Aachener Verfahrenstechnik

RWTH AACHEN UNIVERSITY

Aachener Verfahrenstechnik Series
AVT.CVT – Chemical Process Engineering
Volume 43 (2024)

Kristina Baitalow

Switchable Oxygen Depolarized Cathodes in Flexible Electrolysis Operation

Switchable Oxygen Depolarized Cathodes in Flexible Electrolysis Operation

Schaltbare Sauerstoffverzehrkathoden in Flexiblen Elektrolyseverfahren

Von der Fakultät für Maschinenwesen der
Rheinisch-Westfälischen Technischen Hochschule Aachen zur
Erlangung des akademischen Grades einer Doktorin der
Ingenieurwissenschaften genehmigte Dissertation

vorgelegt von

Kristina Baitalow

Berichter:
Univ.-Prof. Dr.-Ing. Matthias Wessling
Univ.-Prof. Alexander Mitsos, Ph.D.

Tag der mündlichen Prüfung: 02.11.2023

Diese Dissertation ist auf den Internetseiten der Universitätsbibliothek online verfügbar.

Parts of this dissertation have been published. Reproduced with permission from:

Kristina Baitalow, Niklas Köller, Paul Bacmeister, Robert G. Keller, Matthias Wessling,
On the operation of switchable oxygen depolarized cathodes, Chemical Engineering Journal, 2022
DOI: 10.1016/j.cej.2023.143759

Titel: Switchable Oxygen Depolarized Cathodes in Flexible Electrolysis Operation
Schaltbare Sauerstoffverzehrkathoden in Flexiblen Elektrolyseverfahren

Autor: Kristina Baitalow

Reihe: Aachener Verfahrenstechnik Series
AVT.CVT - Chemical Process Engineering
Volume: 43 (2024)

Herausgeber: Aachener Verfahrenstechnik
Forckenbeckstraße 51
52074 Aachen
Tel.: +49 (0)241 8095470
Fax.: +49 (0)241 8092252
E-Mail: secretary.cvt@avt.rwth-aachen.de
http://www.avt.rwth-aachen.de/AVT

Volltext verfügbar: 10.18154/RWTH-2024-09734

Danksagung

Die Vollendung dieser Dissertation schließt für mich ein wundervolles und sehr bedeutendes Kapitel, das nicht facettenreicher hätte sein können. Natürlich wurde ich von der Forschungsumgebung beflügelt, habe gerne Neues erforscht und mich stetig weiterentwickelt – aber noch bedeutsamer waren all die Kontakte, Interaktionen, Diskussionen und Begegnungen, sprich die Menschen, die ich auf diesem Wege kennengelernt und die mich begleitet haben.

Zunächst möchte ich meinem Doktorvater, Prof. Matthias Wessling, für seine Unterstützung und Betreuung meiner Arbeit danken. Du hast an mich geglaubt und mir gleichzeitig die Freiheit gegeben, mich auf meine eigene, vielfältige Weise einzubringen und zu entfalten. Ich war inspiriert durch deine charismatische Art, Forschung zu kommunizieren und Neues, Ungewisses zu wagen. Ich möchte weiterhin meinem Zweitprüfer, Prof. Alexander Mitsos, danken, der weit mehr war als ein Zweitprüfer. Auch du warst ein Mentor für mich, der mich im Forschungsprojekt Synergie und darüber hinaus fachlich gefordert und persönlich gestärkt hat.
Ich möchte Robert Keller für sein stets offenes Ohr und seine außerordentliche fachliche Wegweisung danken, die mir eine Inspiration war. Ich danke Stefanie Kriescher, die meine Arbeiten erheblich verbessert hat und mit ihrem Optimismus und ihrer Unermüdlichkeit ein Vorbild war und ist.

Ein ganz besonderer Dank gilt meinen Kolleginnen und Kollegen am CVT, ohne die ich das Ganze vermutlich nicht durchgezogen hätte. Ihr seid mit mir elektrochemischen Mysterien auf den Grund gegangen; habt mich im Labor, bei Simulationen und Hypothesen unterstützt; aber vor allem habt ihr mir zugehört und mein Leben am und außerhalb des Instituts unglaublich bereichert: Angefangen bei meinen Bürokollegen Florian Roghmans, Elizaveta Evdochenko, meinen Schützlingen - den Electroboys - Jan Vehrenberg, Jonas Bäßler, Matthias Heßelmann, mit denen ich jede elektrochemische Frage diskutieren konnte; meiner MuCo Gruppe und insbesondere Anna Kalde und Ilka Rose für unermüdliche digitale Diss-Stunden; den ”Kaffee-Babos” Anna, Denis Wypysek, Felix Stockmeier, mit denen ich meine CVT-Entwicklung am intensivsten durchgemacht habe; dem Trio Maria Padligur, Niklas Köller, Lucas Stüwe, die selbst den schlimmsten Tag mit Humor oder Radeln bei Aachener Wetter vergessen ließen; Simon Roth, auf dessen Rat ich mich heute noch verlassen kann. Für die hilfreiche Auseinandersetzung mit meiner Forschung und bei der Vollendung meiner Dissertation möchte ich weiterhin Ann-Kathrin Mertens, Stefan Herrmann, Tobias Harhues, Dana Kaubitzsch, Alexander Limper, Mojtaba Mohseni, Christian Linnartz und Sebastian Brosch danken. Als ich selbst noch neu war, habe ich zu euch

aufgeschaut und ihr habt meine Ausbildung mit beeinflusst: Jonas Lölsberg, Hans Breisig, Michael Alders, Korcan Percin, Morten Logemann, Georg Linz, Jan Vennekötter und Axel Böcking.

Ich möchte meinen Projektpartnern, Karen Perrey und Andreas Bulan, besonderen Dank für die sehr fruchtbare und kooperative Zusammenarbeit und natürlich für die Industriezellen, die ich für meine Forschungszwecke bearbeiten durfte, aussprechen.
Ich danke dem Kopernikus-Projekt und insbesondere dem Synergie-Projekt des BMBF, die mir meine Forschung ermöglicht haben; dem Rechencluster der RWTH Aachen University mit Zugang zu exzellenter Rechenleistung; den KollegInnen von der SVT, die ich unter anderem alles zu Modellierung fragen konnte: Moritz Begall, Luisa Brée, Kosan Roh, Jan Schulze und Jannik Lüthje.
Ohne meine 36 Studierenden hätte ich niemals die Ergebnisse der Dissertation geschafft. Ich habe mit euch allen unglaublich gerne zusammengearbeitet und von vielen auch selbst etwas gelernt. Ich danke auch Karen Faensen für ihre kümmernde Unterstützung und die Table-Top und EDX-Bilder; Susi Offermann für den lieben Zuspruch und die Beruhigung in all den Jahren; Jutta Friedrich nicht nur für all die IT-Hilfe, sondern auch für Rückhalt während meiner Zeit in der PR-Gruppe; Roman Ryapushkin und Udo Kosfeld für die Hilfe mit Software und Elektronik; dem Team am DWI Leibniz-Institut für Interaktive Materialien für die Ermöglichung von BET- und XRD-Messungen. Ich danke ZUMOLab GmbH, die mich kurzfristig mit notwendiger Hardware und stets gutem Support unterstützt haben. Und ganz besonders möchte ich der mechanischen Werkstatt des AVT und insbesondere Joachim Schornstein für seine unermüdliche Arbeit an der Industriezelle danken. Tiefer Dank geht auch an das ILR, ganz besonders Sebastian Hille und Dominic Schröder, die mir die Rauchlanze für meine Forschungszwecke zur Verfügung gestellt und diese einmaligen Experimente ermöglicht haben.

Ich möchte auch meinen Freunden in und außerhalb Aachens danken, die mein Leben und meine Persönlichkeit geprägt haben, und mir Halt und Rat gaben, insbesondere Anna Torka, Lea Olbrück, Verena Neisen, die Doppelkopf-Runde und die Kanutruppe. Mit den Dinos und den Rugbeez konnte ich auf dem Spielfeld abschalten und Teamspirit spüren.
Ich danke meinen Eltern und meinem Bruder, dass ihr meine Entscheidungen, egal wie außergewöhnlich, immer unterstützt und für mich da seid. Und schließlich danke ich dir, Max, dass du mein Leben bereicherst und mich mit all meinen Eigenheiten und Ideen begleitest.

People will forget what you said, people will forget what you did,
but people will never forget how you made them feel.

- Maya Angelou

Contents

Abstract

The transition of the energy supply from fossil fuels to renewable energy sources will result in significant fluctuations in the power grid. These fluctuations particularly affect energy-intensive manufacturing processes, requiring short-term adaptation of their production volume. Chlor-alkali electrolysis, as an example for an energy-intensive consumer, can benefit from such demand-side management.

Currently, 86 % of industrial chlorine production is conducted via the membrane-based electrolysis process with chlorine evolution reaction on the anode side and hydrogen evolution reaction on the cathode side. By incorporating a switchable oxygen depolarized cathode, the oxygen reduction reaction substitutes the conventional hydrogen evolution, leading to approximately 25 % savings in energy costs. A thorough flushing of the shared gas compartment between hydrogen and oxygen reactions is necessary to avoid dangerous oxyhydrogen formation. To date, there have been no experimental investigations regarding the switching between the two cathode reactions and their potential effects on long-term operation.

This work aims to comprehend the interaction of both cathode reactions on a single switchable oxygen depolarized cathode and enable a safe switching operation. Investigations of the cell potential and the cathode potential were conducted in an electrochemical lab cell using a three-electrode setup. Additionally, up to 1,600 switching cycles between hydrogen and oxygen reactions were performed to mimic long-term operation. Ex-situ contact angle measurements before and after the switching cycles provided insights into material degradation, while key figures such as the Faraday efficiency indicated the electrochemical performance. The electrochemical experiments revealed a significant correlation between the increase in cell potential and the undesired electrolyte breakthrough to the gas side of the oxygen depolarized cathode. Modifications to the cell design and operational procedures could only partially reduce electrolyte breakthroughs.

Further analysis of the flushing step between hydrogen and oxygen reactions focused on the support structures in the gas compartment. The investigations aimed to enhance mass transfer, eliminate dead zones between the structures, and eventually find the shortest flushing time. CFD simulations and fog experiments visualized the gas distribution. This approach unveiled significant dead zones resulting from a disadvantageous cell geometry. Time-dependent concentration measurements of flushing procedures with different gas combinations confirmed the unexpectedly strong influence of the cell design on flushing efficiency. Finally, an algorithm-supported optimization modifying the gas compartment geometry provided a first approach toward automated cell design improvement for faster flushing.

This thesis highlights the high potential of the switchable oxygen depolarized cathode for flexible electrolysis. The combination of modeling and experimental approaches lays the basis for a holistic evaluation of optimized cell design to ensure a safe and efficient flushing process.

Zusammenfassung

Die fortschreitende Umstellung der Energieversorgung von fossilen Energieträgern auf erneuerbare Energiequellen wird zu erheblichen Schwankungen im Stromnetz führen. Diese Fluktuationen beeinflussen insbesondere energieintensive Fertigungsprozesse und erfordern gegebenenfalls kurzfristige Anpassungen der Produktion. Die Chlor-Alkali-Elektrolyse kann als ein energieintensiver Verbraucher durch schaltbare Sauerstoffverzehrkathoden dieses Lastmanagement gezielt nutzen.

86 % der industriellen Chlorproduktion basiert auf membranbasierter Elektrolyse mit Chlorentwicklung auf der Anodenseite und Wasserstoffentwicklung auf der Kathodenseite. Die Integration einer schaltbaren Sauerstoffverzehrkathode ersetzt die konventionelle Wasserstoffentwicklung durch die Sauerstoffreduktion, was etwa 25 % Energie einspart. Eine gründliche Spülung des gemeinsamen Gasraums zwischen Wasserstoff- und Sauerstoffreaktion ist unerlässlich, um Knallgasbildung auszuschließen. Bislang gibt es keine experimentellen Untersuchungen des Schaltens zwischen den Kathodenreaktionen und möglichen Auswirkungen auf den Langzeitbetrieb.

Ziel dieser Arbeit ist der Betrieb beider Kathodenreaktionen an ein und derselben schaltbaren Sauerstoffverzehrkathode sowie die detaillierte Analyse des Schaltvorgangs. Dafür wurden in einer elektrochemischen Laborzelle das Zell- und Kathodenpotential in einer Drei-Elektroden-Anordnung untersucht. Bis zu 1.600 Schaltzyklen simulierten den Langzeitbetrieb. Mit Ex-situ Kontaktwinkelmessungen vor und nach den Schaltzyklen wird die materielle Abnutzung bewertet, während Kennzahlen wie die Faraday-Effizienz die elektrochemische Leistungsfähigkeit beurteilen. Die Experimente zeigten einen deutlichen Zusammenhang zwischen Zellpotentialanstieg und unerwünschtem Elektrolytdurchbruch zur Gasseite. Modifikationen am Zelldesign und im Betriebsablauf konnten den Elektrolytdurchbruch nur teilweise reduzieren.

Zusätzlich wurde der Spülprozess zwischen Wasserstoff- und Sauerstoffreaktion analysiert, wobei der Fokus auf den Stützstrukturen im Gasraum und deren Einfluss auf die Konzentrationsverteilung lag. Ziel der Untersuchungen waren eine Verbesserung des Stofftransports, die Eliminierung von Totzonen und letztendlich die Ermittlung der minimalen Spülzeit. CFD-Simulationen und Nebelexperimente visualisierten die Gasverteilung und zeigten dabei signifikante Totzonen aufgrund ungünstiger Zellgeometrie auf. Transiente Konzentrationsmessungen der Spülvorgänge mit verschiedenen Gaskombinationen bestätigten den unerwartet starken Einfluss des Zelldesigns auf die Spüleffizienz. Schließlich lieferte eine algorithmengestützte Optimierung, bei der die Geometrie der Stützstrukturen variiert wurde, einen ersten Ansatz zur automatisierten Verbesserung des Zelldesigns für kürzere Spülzeiten.

Diese Arbeit verdeutlicht das beträchtliche Potenzial der schaltbaren Sauerstoffverzehrkathode für flexible Elektrolyseprozesse. Die Kombination aus Modellierung und experimentellen Methoden legt die Grundlage für eine ganzheitliche Bewertung eines optimierten Zelldesigns, um einen sicheren und effizienten Spülprozess zu gewährleisten.

1. Introduction

1

1.1. Motivation

The prospect of global climate change and decreasing fossil-fuel reserves call for a shift towards renewable energies. By increasing electrification from renewable sources, the chemical industry production strives to contribute to reducing greenhouse gas emissions [Erya2022]. However, the shift comes with challenges as it can lead to strong power fluctuations in the electrical grid, where energy demand and supply can mismatch strongly [Saue2019]. Energy-intensive production processes in the chemical industry can mitigate such peaks by adapting production rates to changes in the power supply. Electrolysis processes are particularly predestined to compensate for such fluctuations since they directly consume electrical energy. [Ausf2018]

The chlor-alkali electrolysis (CAE) is an example of such an energy-intensive electrolysis process. Chlorine (Cl_2), the main product, is an important bulk chemical worldwide [Mill2013]. In Europe, 9.2 Mt were mainly produced via the membrane-based process (82.5 %), followed by the diaphragm-based process (11.1 %) and other processes in 2020 [Euro2021]. The membrane-based electrolysis is highly energy-intensive with a specific energy demand of 2.58 MWh per ton chlorine [Klau2017; Euro2021]. Thus, the CAE accounts for 26 % of the electricity demand in the German chemical industry [Ausf2018]. Therefore, the impact of the CAE demand on the electricity market is immense.

Deploying switchable oxygen depolarized cathodes (sODC) in the CAE process allows coping with those power fluctuations [Jöri2011]. The well-established conventional process of CAE involves a hydrogen evolution reaction (HER) on the cathode side. In this case, hydrogen evolves as a side product at industrially typical cell potentials of 3 V [Mous2008]. The sODC allows running the oxygen reduction reaction (ORR) at the same cathode while maintaining constant chlorine production, thereby reducing operational costs [Bula2017]. Therefore, even though oxygen is consumed and hydrogen is avoided as a by-product, savings from a decreased cell potential of 2 V and, thus, energy reduction becomes possible (reported cell potentials at 6 kA m^{-2}, [Mous2008]).

In addition to the flexibility option of variable chlorine production, the sODC creates completely new possibilities in the flexible operation of electrolyzers: In times of expensive energy supply, the ORR is employed (further called O_2 mode), whereas in times of energy surplus at low, or negative, electricity prices, the HER is applied (further called H_2 mode).

On the system level, numerous studies on demand side management and flexible electrolysis support the future potential of sODC in CAE [Brée2019; Roh2022; Klau2017; Saue2019]. On the cell level, research on non-switchable ODC set essential fundamentals in the field of catalyst choice, long-term operation, and modeling, which can also be transferred to the sODC [Mous2008; Furu2000; Sira2008; Röhe2019b]. While these findings have been incorporated into the further development of the sODC, literature has not yet considered the sODC along several switching procedures.

Switching between oxygen and hydrogen requires that the gas compartment of the electrolysis cell is kept without residues to prevent explosive oxygen-hydrogen mixtures. To minimize downtime of the CAE plant, the interim flushing process should be kept as short as possible while ensuring a complete and thorough flushing step. However, gas exchange in electrolytic cells or enclosed spaces still need to be addressed. Systematic flow investigations in combination with cell design optimization of electrolysis cells are not known so far. Gas flow investigations are common in aerodynamics, such as flow investigations in wind tunnels.

1.2. Outline of the Thesis

Figure 1.1 gives an overview of the thesis. After the introduction (Chapter 1), fundamentals and technical background are given in Chapter 2. Then, Chapters 3 and 4 discuss the sODC on a lab scale. Next, Chapters 5 and 6 transfer the investigation to industry size. Finally, Chapter 7 provides an interim prototype cell focusing on cell design optimization.

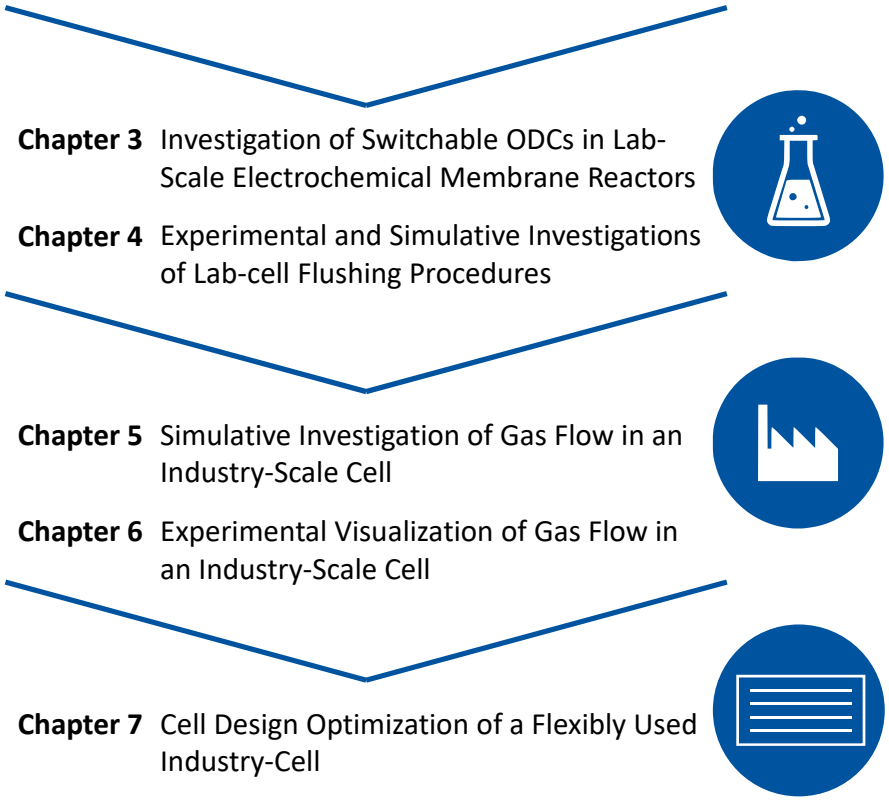

Figure 1.1.: Flexible chlor-alkali electrolysis is evaluated based on lab-scale experiments and CFD simulations using switchable oxygen depolarized cathodes, industry-scale flushing experiments as well as simulations, and an optimized cell design is proposed based on the previous findings.

For the beginning, **Chapter 2** introduces the fundamentals of CAE and (non-) switchable ODC. A short insight into the flexible operation of electrolyzers reveals the applicability of sODC. Furthermore, relevant gas flow and electrochemical investigation methods are presented.

Chapter 3 examines the sODC and its two modes, the H_2 and O_2 modes. Measurements of cathode potentials and overpotentials classify the ORR and HER reactions compared to the literature. Cell potential data provide insights into the energy efficiency of the sODC. In addition, the cell potential is compared as a function of electrolyte and gas volume flows. Finally, over 1,000 switching cycles are conducted, assessing their effects on cell potential, contact angle, and electrolyte retention of the sODC.

Chapter 4 combines numerical simulations with laboratory experiments. The electrochemical cell used in the previous laboratory experiments is simulated to mimic the gas exchange. 3D CFD simulations represent the flushing process. The determined flushing times are verified with laboratory experiments.

The mathematical model is extended towards commercially used industrial cells in **Chapter 5**. The 3D model is reduced to suitable 2D cross-sections. Flow simulation is combined with mass transport to determine the flushing time of the industry cell. Furthermore, density differences of the gases and the resulting effect on gas mixing are incorporated. Finally, the impact of a second outlet on flushing is examined by combining flow simulation, mass transport and density differences.

The objective of **Chapter 6** is to validate the simulation results through experimental flushing tests. The flow distribution in the gas compartment of a commercial electrolysis cell is examined, and the actual flushing time is determined. Concentration measurements at up to three sampling locations for different gas combinations and outlets monitor the flushing process and give a measure for the flushing time. Flow patterns and potential dead zones are visualized using a fog generator. The influence of different gas densities and different outlet positions is highlighted likewise in this chapter.

While Chapter 5 and 6 discuss the importance of a thorough flushing process and reveal problems of the current cell design, **Chapter 7** focuses on cell design optimization. In this chapter, the flushing process is carried out and evaluated under variations of the cell interiors. Cell design optimization is first addressed via CFD simulations of simple geometry adaptions in the default design. Second, a systematic approach using Bayesian Optimization is applied to optimize the geometry based on flow pattern evaluation. A prototype cell is scaled down using the gas compartment of the commercial, industrial cell. Lastly, the selected geometries are implemented into the prototype cell to conduct concentration and visualization experiments.

Finally, **Chapter 8** gives a summary of the presented work and an outlook on the potential of switchable oxygen depolarized cathodes in flexible electrolysis.

Previous Publications in Student Theses

This thesis's content and results emanate from research conducted under the affiliation and position of the author as research fellow and PhD candidate at RWTH Aachen University. The position is associated with the Chair of Chemical Process Engineering. The work comprises data based on the following student theses:

- Vera Ubbenjans, Bachelor's thesis, August 2018, Supervisor: Kristina Baitalow, *Experimental Study of a Bifunctional Oxygen Depolarized Cathode on Laboratory Scale*
- Maria Padligur, Master's thesis, 20.02.2019, Supervisor: Kristina Baitalow, *CFD simulation of gaseous fluid flow through a large-scale industry cell*
- Felix Zuber, Bachelor's thesis, 19.07.2019, Supervisor: Kristina Baitalow, *Investigation of the transition from laminar to turbulent flow in industrial elec-trolysis cells using CFD simulations*
- Martin Ellermann, Master's thesis, 11.08.2020, Supervisor: Kristina Baitalow, *Simulative design optimization of a chlor-alkali industry cell*
- Michel Overlack, Master's thesis, 26.04.2020, Supervisor: Kristina Baitalow, *Analysis and visualization of gaseous flow through the set-up of an industry-sized chlor-alkali electrolysis cell*
- Simon Wennemaring, Master's thesis, 31.03.2021, Supervisors: Kristina Baitalow, Moritz Begall, *Reducing the Flushing Time of the Gas Compartment in Chlor-Alkali-Electrolysis-Cells using Flow Pattern Recognition*
- Niklas Köller, Master's thesis, 30.09.2019, Supervisor: Kristina Baitalow, *Towards a scale-up of switchable oxygen depolarized cathodes in chlor-alkali electrolysis*

- Florian Popkes, Bachelor's thesis, 02.09.2021, Supervisor: Kristina Baitalow, *Rapid Prototyping enables flow analysis of adaptable flow distributors in electrolysis cells*

2. Fundamentals

Parts of this chapter have been published as:
Kristina Baitalow, Niklas Köller, Paul Bacmeister, Robert Keller, Matthias Wessling
On the operation of switchable oxygen depolarized cathodes, Chemical Engineering Journal, 2023
DOI: 10.1016/j.cej.2023.143759

2.1. Electrochemical Industry Processes

2.1.1. The Chlor-Alkali Process

Given the extensive industrial usage of chlorine and the substantial energy demands associated with chlor-alkali electrolysis (CAE), the process is an ideal focus for investigating flexibility options in high-energy industrial operations. The membrane-based chlorine process occurs in an electrochemical cell. A standard electrochemical cell consists of a solid anode and cathode and two liquid electrolytes separated by a membrane. Chlorine gas evolves in the liquid anolyte on the anode side (see Equation 2.1). The majority of chlorine production with membrane processes involves hydrogen evolution reaction (HER) as a counter-reaction on the cathode side (see Equation 2.2). In this thesis, the cathode is a gas diffusion electrode (GDE). GDEs enable a three-phase boundary within a solid porous structure, stabilizing a liquid-gas interface. Therefore, the electrochemical cell can contain an additional gas compartment at the backside of the GDE.

$$4Cl^- \rightarrow 2Cl_2 + 4e^- \qquad \text{(Anode, CAE)} \qquad (2.1)$$

$$4H_2O + 4e^- \rightarrow 2H_2 + 4OH^- \qquad \text{(Cathode, HER, } H_2 \text{ mode)} \qquad (2.2)$$

Figure 2.1a shows the CAE with chlorine evolution on the anode and HER on the cathode side.

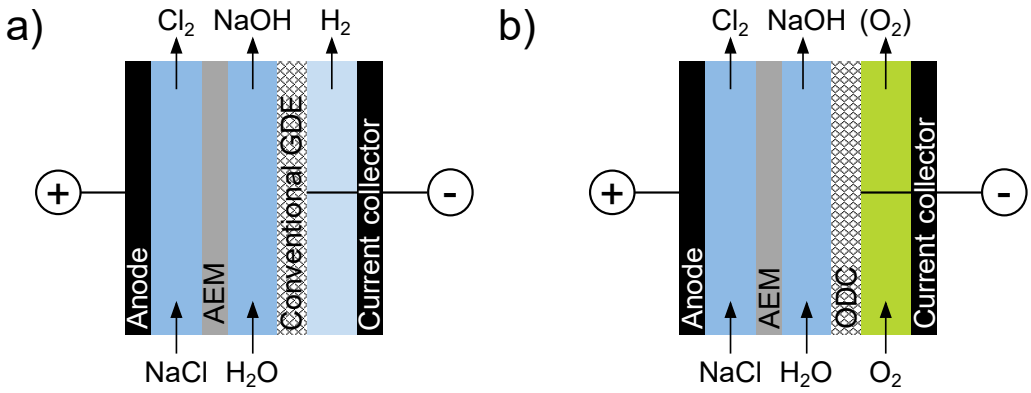

Figure 2.1.: Material flows and cell elements in CAE with a) HER and, b) ORR on the cathode side.

Introducing oxygen depolarized cathodes (ODCs) has unlocked new operational modes in CAE. With ODC, the oxygen reduction reaction (ORR) takes place (see Equation 2.3) instead of the HER on the cathode side.

$$2H_2O + O_2 + 4e^- \rightarrow 4OH^- \qquad \text{(Cathode, ORR, } O_2 \text{ mode)} \qquad (2.3)$$

Figure 2.1b depicts the O_2 mode with ORR on the cathode. Oxygen is supplied to the cell through the gas compartment. ORR occurs again at the three-phase boundary between liquid catholyte, oxygen gas, and solid catalysts in the pores of the ODC. Excess oxygen leaves the gas compartment through the cell outlet.

ODCs are a type of GDEs. Figure 2.2 shows the structure of the ODC containing polytetrafluoroethylene (PTFE) fibers and catalyst particles supported on a metal mesh. This composition facilitates the build-up of the three-phase boundary and provides good mass transport of the reaction substances. The hydrophilic catalyst enables water transport toward the reaction site; the porous structure with its hydrophobic PTFE elements guides the movement of oxygen toward the reaction site in ORR, or the removal of hydrogen in HER, respectively.

ODCs have been known since the 1950s and moved into focus for industrial use in the 1970s. Detailed studies and reviews describe several stages in ODC development up to 2008 [Mous2008; Uchi1997; Chli2004; Moor2000; Fede2001; Kiro2006; Okaj2005]. Progress was reported on laboratory, pilot, and industrial scales, in material and catalyst selection, as well as in process operation (e.g., for adjustment of the sensitive liquid-gas pressure ratio). In the 1990s, a second phase of ODC research in chlor-alkali electrolysis came up in Japan [Mous2008]. It led to the first industrial application in Germany in 1998 by Bayer, Uhde, and DeNora with electrode areas of 2.7 m^2 [Mous2008; Moor2000].

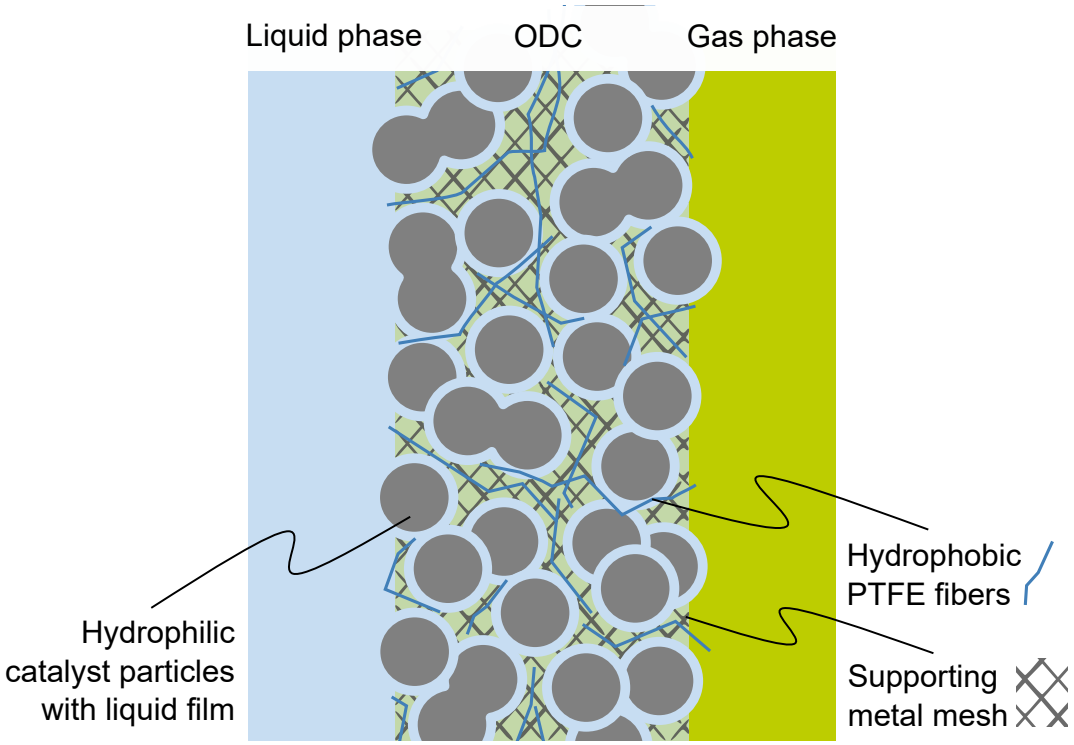

Figure 2.2.: ODC structure (metal mesh carries PTFE fibers and catalyst particles) creates a porous system facilitating a gas-liquid-interphase (adapted from [Jöri2011]).

The combination of chlorine evolution on the anode and hydrogen evolution on the cathode is regarded as the well-established, conventional chlor-alkali electrolysis. CAE with HER is highly energy-intensive with a specific energy demand of 2.58 MWh per ton chlorine [Klau2017; Euro2021]. Although ODCs require oxygen as a feedstock, they reduce the energy demand by up to 25 % [Jöri2011]. The energy demand can be assessed from the standard potentials needed for the reaction and is relevant to compare the O_2 and H_2 modes. Standard potentials represent the minimum voltage required to initiate a chemical reaction at an activity of 1, under standard conditions (25 °C, 1 M concentration, 1 atm pressure) and with no current flowing [Schm2003]. Figure 2.3 shows the standard potentials of the reactions of CAE vs. Standard Hydrogen Electrode (SHE). The SHE is a reference electrode (RE), which means it has a tabulated potential under standard conditions and does not change during the reaction. In the case of SHE, this potential is 0.00 V. The difference between the depicted potentials

in Figure 2.3 indicates the required cell potential and is used to calculate the energy demand of the process. In theory, the potential difference between the standard potentials of chlorine evolution and ORR is 0.96 V, which is much smaller than the theoretical potential difference between the chlorine reaction and HER (2.19 V). In reality, additional overpotentials occur in the process (see Chapter 2.2.6). Overpotentials explain the nonlinear course of the electrode potential with increasing current density, as shown in Figure 2.3.

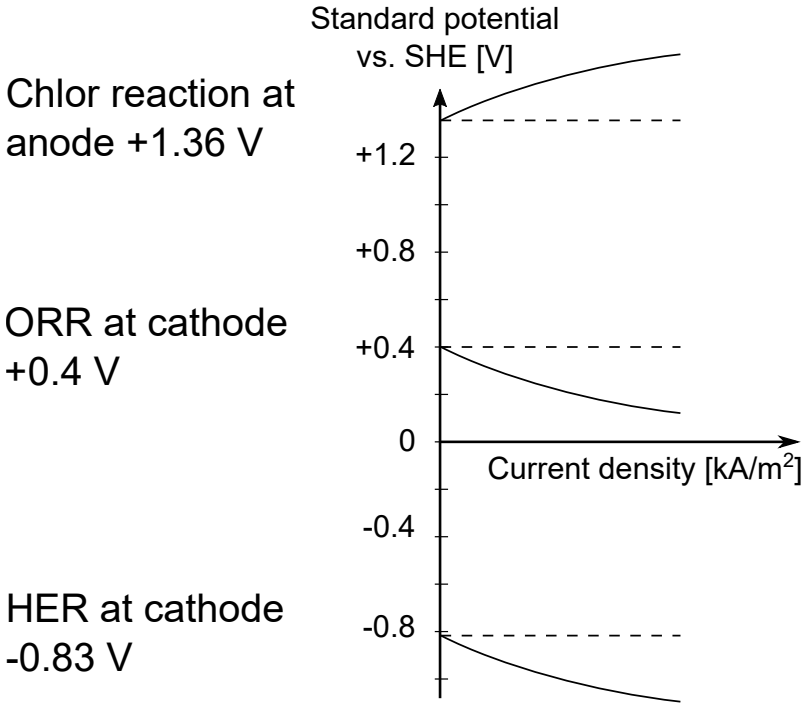

Figure 2.3.: Standard potentials of reactions in CAE vs. Standard Hydrogen Electrode (SHE) as a function of current density.

2.1.2. Flexibility Options of Chlor-Alkali-Electrolysis

A further step towards flexible energy consumption emerged with the invention of the switchable ODC (sODC) [Bula2017]. The sODC enables the oxygen-consuming ORR at a moderate energy demand, subsequently referred to as the O_2 mode. Alternatively, the conventional HER can occur at a high energy demand in the H_2 mode. The energy-intensive H_2 mode can be used in times of energy surplus, generating the by-product hydrogen,

which is usable as an energy source or for chemical synthesis [Jöri2011]. When energy prices rise, the process can be switched to the O_2 mode with lower energy demand [Brée2019]. The switching between those two modes allows for a flexible process operation to compensate for fluctuating energy production that naturally arises in markets with a significant share of renewable energy.

Due to the relatively recent development of sODC, there are only few literature references to this new material. Instead, the available literature on ODCs can be consulted for the operation of sODC. Research has focused on the long-term stability of ODCs under industrial conditions in the O_2 mode, and few compared the ODC with the conventional hydrogen-evolving cathode [Kiro2006]. However, the available studies examine the HER and ORR reactions individually. Work, including the switching process between the two reactions, is not yet available.

2.1.3. Techno-Economical Aspects of Flexible Chlor-Alkali-Electrolysis

The viability of flexible CAE depends not only on the physical suitability of the components but also on the balance of capital (CAPEX) and operating expenses (OPEX) [Brée2019; Roh2019b]. Material costs are incurred due to the need for new sODC catalysts and cells, as well as additional (peripheral) elements [Mous2008; Berg1982]. Regarding consumables, prices are expected to fluctuate and potentially increase more strongly for raw materials, electricity from renewable energies, and profits from by-products in the future [Klau2017; Saue2019; Roh2022]. In that context, demand-side management is becoming increasingly relevant.

The studies mentioned in the following are based on modeling work with a techno-economical focus. Extensive studies deal with the demand-side management of CAE based on raw materials, electricity prices, or material flows [Brée2019; Brée2020; Roh2019b; Roh2019a; Roh2022; Klau2017; Saue2019; Wang2014; Otas2019; Weig2021]. These model-based studies have concluded a high potential of dynamic CAE for load

reduction and power grid stabilization. Further flexibility options exist, such as the integration of electrolyzers in chemical processes to absorb energy peak loads or the combination of batteries for energy storage [Brée2020]. The incorporation of switchable sODC with additional flexibility options due to the two different cathode reactions can extend the flexibility options of CAE [Brée2020; Roh2022]. With an increasing supply from renewable energies, the available power in the grid will fluctuate more strongly and thus significantly increase the profitability of a switchable process between hydrogen and oxygen mode [Brée2019; Roh2022]. However, Moussallem et al. [Mous2008] have concluded that economic viability of sODC is still not fully answered. It is a complex system directly affected by material prices, costs for new cells and plant change-over, and the subsequent utilization of the by-product hydrogen [Mous2008; Brée2020].

However, further experimental investigations on the cell components under flexible operation are necessary for economic applicability in future energy scenarios [Brée2019; Roh2019b]. According to available information, no experimental studies exist on the switchable operation of ODCs.

Other studies on the dynamic operation of electrolyzers mainly address water electrolysis, as it finds wide application in the use of excess energy from renewable energy sources. However, the studies highlight some challenges also relevant to CAE, such as the degradation of cell components, complex adjustments to intensity and frequency of energy fluctuations, and efficiency losses [Haug2017a; Amor2014; Amor2017; Ursu2012; Brau2020; Seib2018].

2.2. Studies on Flexible Lab-Scale Electrolysis Processes

2.2.1. ODC Development

There are numerous studies on manufacturing and composition and their effects on ODC properties, such as how to affect electrolyte flooding and gas percolation through hydrophobicity [Mous2008; Mous2012; Furu2000;

Sira2008; Saka1999; Saka1998]. In general, the material choice is relevant for the start-up and shutdown of the electrolyzer [Sira2008; Staa1985; Schm1982]. Thus, it is especially crucial for a flexibly operated electrolyzer. Most ODC manufacturing processes are based on carbon-containing platinum or silver catalysts within a PTFE framework to ensure hydrophobicity. The hydrophilic silver particles promote electrolyte transport, while the hydrophobic PTFE elements expose the coarser of the GDE pores for gas access [Mous2012; Fran2019]. However, carbon-based electrodes show stronger deactivation than silver-PTFE electrodes, especially in combination with a shutdown of the electrolyzer [Staa1985; Schm1982]. Silver-carbon-based materials are prone to electrode flooding and highly sensitive to uncontrolled shutdowns [Sira2008]. In addition, silver-PTFE electrodes show leakage, which can be explained by degradation due to a loss of hydrophobicity attributed to alteration of the PTFE content in the electrode [Mous2008]. For platinum-carbon-based electrodes, an increasing cell potential and catholyte leakage through the ODC have been reported [Saka1999; Saka1998]. Due to the significant demand for electrolyzers and cell area, there are efforts to find alternative low-cost non-noble metals instead of silver or platinum catalysts, but so far, alternative catalysts show rather sluggish reaction kinetics [Figu2013].

2.2.2. Cell Potential

The evaluation of the cell potential in an electrochemical cell is a good indicator of energy consumption during an electrolysis process and is directly influenced by both electrode reactions. This thesis employs water splitting as a replacement system, with oxygen evolution at the anode. Therefore, comparing cell potentials with the literature is challenging since systems implementing the ODC in CAE typically involve chlorine evolution at the anode. Moreover, variations in electrolyte gap and membrane type further complicate the comparison. Nevertheless, cell potentials discussed in alkaline water electrolysis (AWE) are comparable to the system used in this thesis.

For example, Vincent et al. [Vinc2017] stated that an AWE using anion exchange membranes (AEM) typically operated at cell potentials of 1.9 V for a current density of 400 mA cm^{-2} at 40 °C. In a more detailed follow-up study, Vincent et al. [Vinc2018] elaborated that typical AWE processes operated at a current density of about 400 mA cm^{-2}, at temperatures of 70 °C to 90 °C, with a cell potential in the range of 1.85 V to 2.2 V, and conversion efficiencies in the range of 60 % to 80 %.

While in industrial CAE processes, typical cell potentials range from 3.1 V to 3.3 V at 400 mA cm^{-2} to 600 mA cm^{-2}, the cell potential was significantly reduced when using ODCs [Kiro2006; Mous2008]. Table 2.1 summarizes cell potentials and corresponding current densities similar to this study. In general, values differ based on ODC composition and process parameters. Studies achieved cell potentials between 1.8 V at 200 mA cm^{-2} and 2.17 V at 300 mA cm^{-2} in the O_2 mode using ODCs, which closely resemble AWE values. Moussallem et al. [Mous2012] observed cell potentials of 2.5-2.75 V at 600 mA cm^{-2}, indicating larger overpotentials at higher current densities. Furuya and coworkers measured a 0.14 V increase in cell potential when the electrolyte gap was increased from 0.4 mm to 7 mm [Furu1998; Naka1999]. Kiros et al. [Kiro2006] reported a cell potential reduction of 31-38 % to up to 2.0 V when using the ORR on the cathode side instead of a cathode with HER. Further insights into ODC development between 1973-2006 are compiled by Moussallem et al. [Mous2008].

Table 2.1.: Cell potentials using ODCs in CAE

U_{cell} in V	J in mA cm^{-2}	Other boundary conditions	ODC catalyst	Study
1.85	200		Ag	[Jöri2011]
1.8 2.5-2.75	200 600		Ag	[Mous2012]
2.17	300	85 ℃	Ag	[Staa1985]
2.14 2.0	300	7mm catholyte gap 0.4mm catholyte gap	Ag Ag	[Naka1999] [Furu1998]
2.05	300	90 ℃; zero gap cathode arrangement	Ag	[Ashi1997]
2.0	300	2mm catholyte gap, 90 ℃ carbon-based electrodes	C	[Saik1999]

2.2.3. Cathode Potential

A potential difference can also be measured between an element of the electrochemical cell, e.g., the anode or the cathode, against a RE. The SHE, as a type of RE, is based on the half-cell reaction of the reduction of protons to hydrogen gas under standard conditions and ion activity of 1. The standard electrode potential of the SHE is defined as 0 V in an ideal electrolyte at all temperatures. A practical sub-type of the SHE, the reversible hydrogen electrode (RHE), has the advantage of pH-dependent potential changes and can be directly utilized in the electrolyte. The standard potential of the RHE vs. SHE can be described as [Schm2003]:

$$E_0 \text{ vs. SHE} = 0 - (0.0591\,\text{V} \cdot pH) \tag{2.4}$$

Other reference electrodes with a constant, reproducible equilibrium potential can be used in practice. Reference electrodes with electrolyte fillings similar to the experimental setup should be used to keep measurement falsifications low. [Bard2001]

Since both HER and ORR can occur at the sODC, the two reactions are summarized for common conditions in Table2.2. The few documented values for HER on porous GDEs strongly depend on the material composition,

resulting in significant scattering within the range of −0.4 V to −0.1 V vs. RHE [Bula2017]. Other data for HER mainly focuses on solid planar electrodes. For ORR, cathode potentials vary in the range of 0.59 V to 0.866 V vs RHE depending on cathode composition and boundary conditions.

Table 2.2.: Cathode potentials of HER and ORR

U_{cath} in V vs. RHE	J in mA cm^{-2}	Other boundary conditions	Study
		HER	
-0.4 to -0.1	150	11 M NaOH; 63 °C	[Bula2017]
		ORR	
0.7 to 0.8	400	11 M NaOH; 80 °C	[Bula2017]
0.59 to 0.72	400	11 M NaOH	[Mous2012]
0.48	400	7.5 M NaOH; 50 °C	[Gebh2019]
0.866	300	8 M NaOH; 70 °C	[Kiro2006]
0.75	300	11 M NaOH;	[Furu2000]

Only a few studies directly addressed both cathode reactions in comparison. Kiros et al. [Kiro2004; Kiro2006] compared a Nickel cathode to a self-made ODC in a 10 cm^2 cell (300 mA cm^{-2}, 8 M NaOH, 80 °C [Kiro2006]) regarding the energy demand. In that study, the implementation of the ODC resulted in a reduction in energy demand with a simultaneous temperature increase of approximately 35 °C. The findings indicate that the ORR is more exothermic than the HER and, therefore, requires less heat supply [Kiro2004].

Figueiredo et al. [Figu2013] compared a self-made copper-doped ODC to an H_2-evolving graphite electrode. Linear potential scans revealed a significant current increase when O_2 was supplied compared to an N_2-atmosphere. The current increase was observed, particularly at high cathode potentials. After 60 min of chlorine electrolysis, the ODC had a 1 V lower cell potential at room temperature and a 1.2 V decrease at 70 °C compared to the H_2-evolving graphite electrode. The amount of chlorine produced did not change for the different cathodes.

2.2.4. Gas Bubble Evolution

When implementing industrial boundary conditions, a particular challenge is the gas bubble management at the electrodes, especially at high current densities. Gas evolution can have an impact on the electrolyte resistance and lead to fluctuations in cell potential [Angu2020; Naga2003; Abba2008; Angu2022]. The intensity is influenced by electrolyte concentration, flow velocity, temperature, and current density [Haug2017a; Roy2006; Bula2017; Kiro2006; Bisa1991; Angu2022]. Numerous studies have experimentally and theoretically investigated the effects of gas-evolving electrodes with ambitions to minimize the so-called internal resistance (iR) drop. The iR drop is a potential drop that occurs due to the voltage loss across the internal resistance of an electrochemical cell, resulting from the flow of current through the cell (see [Schm2003] for further information). Gas formation and associated effects also occur at solid, planar electrodes. In CAE, porous GDE cathodes are combined with solid dimensionally stable anodes (DSAs). Besides CAE, literature on gas bubble formation at solid electrodes can be found subjecting water and CO_2 electrolysis. Kiros et al. [Kiro2006] suggested implementing inter-electrode gaps, which prevent entanglement of gas bubbles between anode and membrane, but these gaps have the disadvantage of a higher iR drop. Angulo et al. [Angu2020] intensively studied gas evolution at solid electrodes; and concluded a dynamic behavior of bubble nucleation, growth, and detachment to dynamically influence cell potential and ohmic resistances. Zhao et al. [Zhao2019] investigated the entire path of the gas evolution and equations to model the individual influences. They attributed the ohmic resistance increase to changes in the solution paths through the bubbles moving in the electrolyte. Chen et al. [Chen2012] showed via wavelet transform analysis of potential noise that an increase of the current density from 100 $mA\,cm^{-2}$ to industrially more relevant values of 400 $mA\,cm^{-2}$ results in stronger cell-potential noise. Furthermore, higher currents increased the amplitude and frequency of the noise, which was caused by bubble formation and detachment – and should be avoided to ensure stable electrode performance. At the same time, electrodes that release many small, evenly distributed bubbles were preferred to those favoring the

coalescence of large bubbles at long time intervals. Investigations were performed in stagnant electrolytes with solid, planar electrodes [Chen2012]. Pumping of the electrolyte avoided gas accumulation in the electrolysis cell, which prevented drastic temperature increases due to overpotentials and ohmic losses [Haug2017a]. High electrolyte flow rates can generally reduce the nucleation and bubble growth rate of the undesired dissolved gases [Roy2006] on one side and decrease the disadvantageous electrode bubble coverage on the other side [Balz2003].

Redox reactions with gas as the consumed species, such as in the ORR or the CO_2 reduction, require a sufficient gas supply to proceed unlimitedly. Equation 2.3 also shows the need for water as a reactant. The pores of GDEs are excellent for allowing simultaneous contact between gaseous oxygen, liquid water, and solid catalyst. This emerging three-phase equilibrium thus determines the reaction zone. Porous GDEs, or more precisely, sODCs, therefore, allow for maximization of the reaction area compared to solid planar electrodes. Figure 2.4 shows such a porous GDE. Here, the effect of hydrostatic pressure through the electrolyte on the constant gas pressure in the vertical structure of a GDE is illustrated: gas breakthrough can occur in the upper region of the gas compartment, while the increasing hydrostatic pressure in the lower part of the cell can lead to electrolyte flooding. Both phenomena reduce the active area of GDEs and must be avoided. [Jöri2011]

In industrial applications with a large cell height, the direction of the evolving gas was adjusted via slightly increased pressure on the electrolyte side of the GDE [Bula2017]. However, elevated pressure can also have a negative effect on gas bubble formation due to smaller bubbles and coalescence impediment [Roy2006].

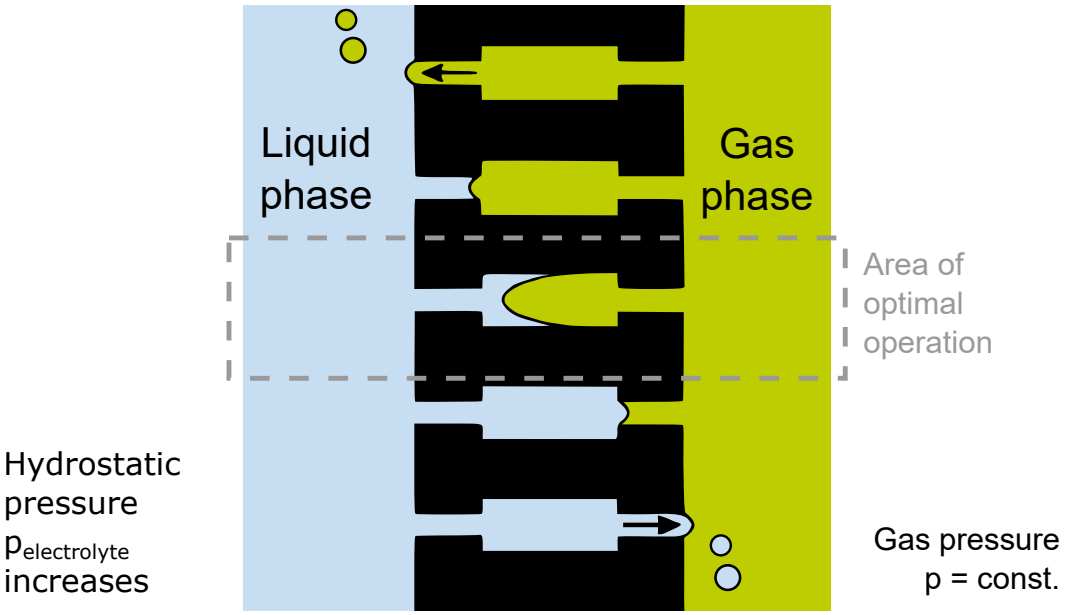

Figure 2.4.: Three-phase boundary in pores of a gas diffusion electrode (adapted from [Jöri2011]).

Phenomena related to gas evolution at porous GDEs have been studied for sODCs in CAE and other electrolysis processes. For CAE, Moussallem et al. [Mous2012] investigated NaOH leakage to the gas side ($1\,g\,d^{-1}$ to $4\,g\,d^{-1}$ per electrode area) as well as oxygen breakthrough to the catholyte side (25 mbar to 185 mbar oxygen overpressure). They recommended silver/PTFE loadings of at least $200\,mg\,cm^{-2}$ to prevent leakage of the electrolyte NaOH to the gas side. These loadings allow oxygen overpressures of more than 100 mbar without a gas breakthrough. In their experiments with varying loadings, they revealed that a decreasing PTFE content and increasing electrode thickness lower electrolyte leakage and, at the same time, need higher pressures for oxygen to break through. For CO_2 reduction, Jeanty et al. [Jean2018] observed bubble agglomeration in CO_2 electrolysis leading to electrical insulation in their $100\,cm^2$ cells.

2.2.5. Electrowetting

Electrowetting is a characteristic phenomenon for gas diffusion electrodes. Besides the above-discussed gas bubble evolution, electrowetting and electrolyte leakage through the (s)ODC can be detrimental. Adverse effects have

been observed in long-term experiments, from which recommendations for the (s)ODC composition could be derived [Mous2012].

Detailed models for the electrolyte distribution exist for GDEs [Pinn2011] and ODCs, in particular, [Chav2015]. These simulative studies indicated that, especially at high current densities, there is insufficient O_2 at the electrocatalyst, and consequently, mass transport limitation prevails over low electrocatalytic activity [Pinn2011; Chav2015].

Paulisch et al. [Paul2019] investigated how electrolyte droplets covered the backside of ODCs via chronoamperometric measurements at different potentials. They observed a faster droplet formation and accumulation at higher overpotentials (equivalent to higher current densities), which they explained by increased electrowetting. Also, the authors measured stronger current density fluctuations at higher overpotentials, which might result from the different sizes of the emerging droplets.

In a following study, Paulisch et al. [Paul2021] investigated electrolyte distribution and filling of GDE pores. Operando synchrotron imaging confirmed the effect of electrowetting: Higher temporal fluctuations in electrolyte distribution with increasing overpotentials. Additionally, the authors found that pore flooding is irreversible.

Bienen et al. [Bien2022] investigated the electrolyte breakthrough in a GDE via a digital microscope. A higher overpotential facilitated the breakthrough of electrolytes to the GDE gas side. Faster droplet formation with higher overpotentials again indicated electrowetting. Surprisingly, an earlier electrolyte breakthrough was observed for GDEs with a higher PTFE content. Higher PTFE content and lower overpotentials resulted in smaller electrolyte droplets and less droplet coverage at the GDE backside. The images showed that once a pore is filled with electrolyte, a droplet forms, and continuous electrolyte flow leads to droplet growth.

Franzen et al. [Fran2019] demonstrated that electrolyte filling in ODC pores is key to efficient electrolysis. They have identified an optimal PTFE fraction that is low enough to enable pore filling and, simultaneously, high enough to avoid pore flooding. Tafel slopes revealed that the catalytic performance was comparable for different PTFE fractions, and thus overpotentials

were attributed to the physical three-phase formation. In addition to a low PTFE content, high overpressure also caused pore flooding, which had a detrimental effect on overpotentials.

Kalde et al. [Kald2022] developed a microfluidic device with a porous, conductive structure, multi-scale porosity, and heterogeneous surface wettability to mimic conventional GDEs. They showed non-reversible wetting of microfluidic porous structures via in-operando visualization using confocal laser scanning microscopy. In addition, they visualized that the potential onset applied to gas-fed electrolyzers might disrupt the previously stable phase boundary.

2.2.6. Overpotentials

Overpotentials refer to the excess voltage applied to an electrochemical cell or electrode to drive an electrochemical reaction at a specific rate. It represents the additional voltage needed to achieve a particular current density or reaction rate beyond the thermodynamic equilibrium potential [Hama2005]. Figure 2.5 shows an exemplary overpotential distribution in an electrochemical cell with two liquid electrodes separated by a membrane. Typical overpotentials arise from the ohmic potential drop at the electrodes ($\eta_{\Omega,s,C}$, $\eta_{\Omega,s,A}$), the overpotential for the reactions ($\eta_{rt,C}$, $\eta_{rt,A}$), the concentration overpotential at the electrode surfaces ($\eta_{c,C}$, $\eta_{c,A}$), the iR drop of the electrolytes ($\eta_{\Omega I,C}$, $\eta_{\Omega I,A}$), and the iR drop of the membrane ($\eta_{\Omega M}$).

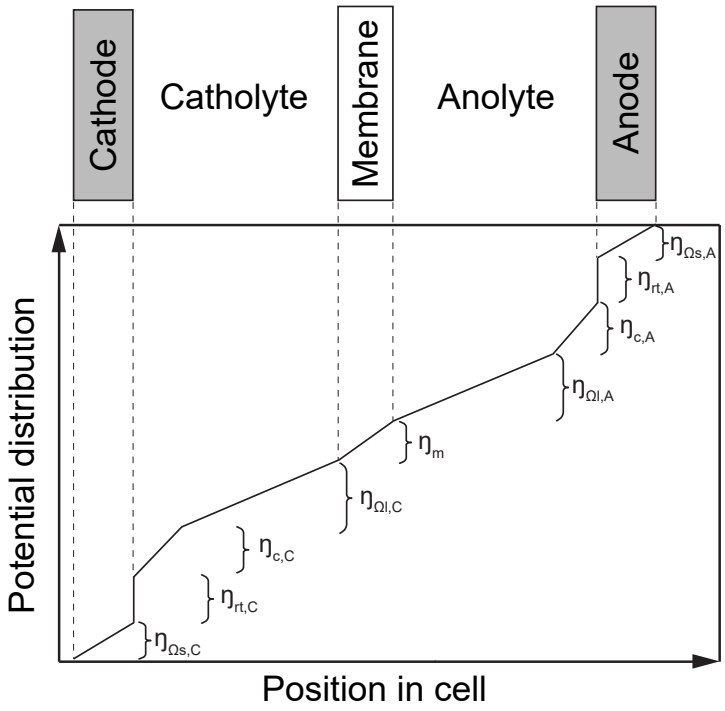

Figure 2.5.: Exemplary potential distribution in an electrochemical cell with two liquid electrolytes (adapted from [Venn2019a]).

Overpotentials can be directly influenced by reaction kinetics (characterized by anode and cathode potentials), cell design (distances between cell elements), and gas bubble evolution. Reducing those overpotentials can lead to remarkable energy savings [Venn2019a]. Thus, some studies dealing with overpotentials in electrochemical cells running HER or ORR are discussed in the following.

Morimoto et al. [Mori2000] measured an overpotential of 0.439 V in ORR at a current density of 200 mA cm^{-2}. For a cathode potential of –0.28 V at 200 mA cm^{-2} (approximately –0.3 V at 300 mA cm^{-2}), the potential difference between O_2 and H_2 mode was 0.85 V.

Moussallem et al. [Mous2012] confirmed higher cell potentials due to more overpotentials at increasing current density using an ODC setup for ORR.

Nickel shows a high initial electrocatalytic activity towards the HER in water electrolysis. However, it experiences extensive deactivation as a cathode during AWE. Deactivation of the cathode is manifested by either

a current loss at a fixed electrode potential or an increase in hydrogen overpotential at a constant current [Zoul2004].

2.3. Large-Scale Analysis of Gas-Flow Reactors

2.3.1. Demands on Flexible Gas Exchange

Flexibility is directly influenced by the switching operation of the sODC between H_2 and O_2 modes. This flexible switching has three constraints: (1) the switching timing depends on the current market prices of electricity and raw materials [Brée2019; Roh2019b]; (2) since the switching process takes place without current applied, the electrolyzer is shut down, and chlorine production is paused, making a short-term chlorine storage indispensable [Brée2019]; (3) it is economical to keep the flushing process as short as possible to ensure the shortest possible downtime in chlorine production and to minimize the flushing gas to be discharged [Brée2019]. Literature is available on the first two constraints [Brée2019; Roh2019b; Roh2022; Klau2020]. However, further investigation of the flushing step is necessary to enable the most realistic implementation on an industrial scale, especially under constant chlorine production [Brée2019; Klau2020].

Switching between the H_2 and O_2 modes includes flushing the gas compartment in the electrolysis cell with an inert gas to prevent the formation of a potentially explosive oxyhydrogen mixture [Bula2017]. The time required for this flushing step is an important parameter that needs to be investigated and optimized for an economically viable industry-scale process.

The studies mentioned in Chapter 2.2 primarily focus on the further development of the (switchable) ODC, the integration of cost-effective non-noble catalysts, the manufacturing of the ODC (with those catalysts) and optimization of the ODC or the process conditions for a stable electrolyte-gas balance (e.g., through the addition of PTFE). However, a rapid gas change is inevitable to introduce flexibility to the CAE process. Cell design, in particular, plays an important role in this context. So far, no studies explicitly address gas management and flow distribution in electrolysis cells.

Safe and efficient gas exchange is characterized by the following:

- Minimization of the flushing time,
- Complete exchange of the gases involved or the total displacement with inert gas to undercut explosion limits, and
- A flow-optimized and easy-to-manufacture cell geometry.

However, studies of gas flow in electrolysis cells focus primarily on models for reaction rates, diffusion layers at electrodes (in most cases, gas diffusion electrodes), and mass transport towards and away from the electrode. Reaction-free flushing of gas compartments has yet to be addressed.

2.3.2. Flow Visualization by CFD Simulations

The laws of conservation of mass, momentum, and energy describe fluid flow. The differential form of the conservation of mass equation is called the continuity equation [Durs2006]:

$$\frac{\partial \rho}{\partial t} + \nabla \cdot (\rho \vec{u}) = 0 \tag{2.5}$$

Here, $\vec{u}$ represents the velocity vector, t denotes time, and ρ stands for the fluid density. If the fluid movement is modeled incompressible, the density remains constant regardless of the flow. Hence, the continuity equation simplifies to [Schr2004b]:

$$\nabla \cdot \vec{u} = 0 \tag{2.6}$$

The Navier-Stokes equation (NSE) reflecting the conservation of momentum can be expressed as [Adam2008]:

$$\frac{\partial}{\partial t}(\rho \vec{u}) + \nabla \cdot (\rho \vec{u} \vec{u}) = -\nabla p + \nabla \underline{\tau} + \rho \vec{f} \tag{2.7}$$

$\underline{\tau}$ is the stress tensor, p matches the pressure, while $\vec{f}$ corresponds to specific volume forces. Regarding energy, the fluid flow is assumed to be

isothermal, entering at a fixed temperature.

Fluid flow can be classified into two main regimes: laminar and turbulent. The dimensionless Reynolds number can be calculated to determine whether the flow is laminar or turbulent. The Reynolds number is the ratio of inertial vs. viscous forces acting on the fluid [Oert2015]:

$$Re = \frac{inertialforces}{viscousforces} = \frac{\rho \cdot L \cdot u}{\eta} \tag{2.8}$$

L is the characteristic length and η is the viscosity of the fluid. The fluid flow can be assumed laminar if the resulting value is below the critical Reynolds number (Re_{crit}). However, The critical Reynolds number depends on the geometry and differs for distinct systems. For tube flow, $Re_{crit,tube}$ is 2300 while for a planar plate $Re_{crit,plate}$ equals $5 \cdot 10^5$ [Oert2015].

To assess whether mass transfer is predominantly governed by diffusion or convection, the dimensionless Péclet number is employed [Bird2002]:

$$Pe = \frac{convection}{diffusion} = \frac{u \cdot L}{D_{ij}} \tag{2.9}$$

Here, L is the characteristic length, and u denotes the velocity. Similar to the Reynolds number, the characteristic length is specific to each geometry, and various geometries exhibit different characteristic lengths. For $Pe >> 1$, convection dominates the mass transport [Zien2000].

Computational Fluid Dynamics (CFD) involves solving the NSE using computer-based methods. Since NSE are partial differential equations, analytical solutions are typically limited to elementary applications. More complex problems require simplifying the case or using empirical equations to reduce their complexity. Therefore, discretization techniques transform the continuous model into a discrete one. The discretization of a model can be achieved using different methods. The common Finite Element Method (FEM), which has the highest flexibility but the lowest accuracy, replaces the differential equations with linear and parabolic equations [Lech2011; Laur2018]. In the following, it is discussed how numerical methods can

approximate the case.

CFD software can model both laminar and turbulent flows. The flow profile is uniform in laminar flow without noticeable small-scale fluctuations [Adam2008]. The fluid moves in parallel layers, and the macroscopic exchange is primarily diffusion-driven and thus negligible. Exchange events are mainly initiated by momentum transports transverse to the flow direction [Durs2006]. Figure 2.6 a) shows the course of laminar flow lines. The individual layers represent different velocities. Frictional forces manifest as shear stresses between the layers. The full NSE are employed for the numerical calculation of laminar flow, meaning that all influences are considered, including frequencies and even minor variations [Lech2011].

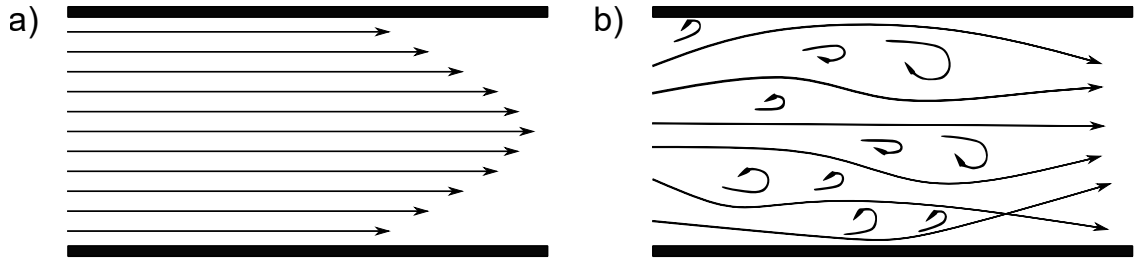

Figure 2.6.: a) Uniform streamlines in a laminar flow profile, b) streamlines dissipate chaotically in a turbulent flow profile.

On the contrary, inertial forces predominate over frictional forces in a turbulent flow. As a result, the flow layers get increasingly non-uniform since velocity fluctuations occur more frequently. The changes in the flow variables lead to additional transverse momentum and energy exchange between the flow lines [Oert2015], which in turn causes further instability mechanisms [Adam2008]. As a result, the uniform layers from laminar flow dissipate and form random, chaotic streamlines, as shown in Figure 2.6 b).

Figure 2.7 shows the averaged velocity for turbulent and laminar flow over time. Comparing the velocity profiles of both flows, the occurring instabilities in the turbulent region affect the resulting velocity. Consequently, the flow velocity changes with time for turbulent flow, while it can be assumed constant for laminar flow. The transition from laminar to turbulent flow occurs smoothly. This additional flow region is called the transition

region [Schr2004b]. Over several intermediate states, the uniform laminar flow increasingly loses its typical characteristics, and the local fluctuations accumulate. Within these states, the instabilities are briefly intensified and damped in alternation [Durs2006].

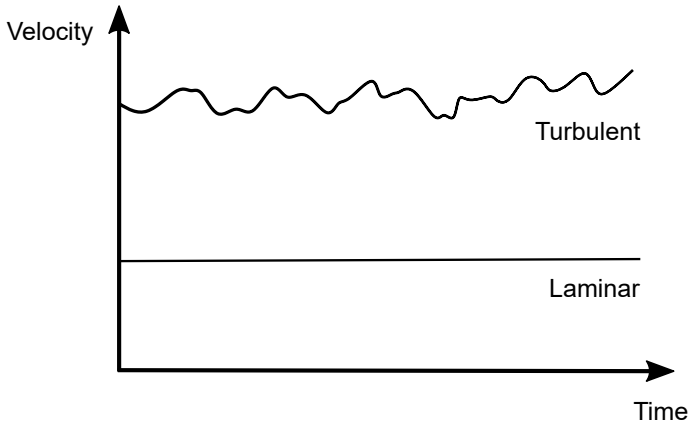

Figure 2.7.: Velocity profile of a laminar and a turbulent flow regime over time.

A very detailed local and temporal resolution is required to compute turbulent flow. For this reason, turbulence models were developed that statistically describe occurring fluctuations to solve the NSE. The computation time can be reduced using Reynolds-averaged Navier-Stokes equations (RANS). The RANS do not solve small turbulences but model them via empirical turbulence models that reproduce the physics adequately [Lech2011]. RANS approximate velocity and pressure by the sum of their mean values and the corresponding statistical variation [Lech2011]. Therefore, the accuracy of the solution depends on the chosen turbulence models. Different turbulence models are available in commercial simulation software, like COMSOL Multiphysics, to approach the velocity and pressure fields.

The κ-ϵ turbulence model is the most widely used and is applied in this thesis. This model uses two equations for approximating the turbulent kinetic energy κ and the turbulent dissipation rate ϵ. The kinetic energy κ can be interpreted as a level of turbulence. κ concentrates mainly in the larger vortices, which decompose into smaller vortices and lead to energy dissipation ϵ. Both values κ and ϵ are calculated independently. Therefore, the κ-ϵ turbulence model is also the turbulence model that needs

the least computation time. The model uses an equation each to calculate the turbulent energy κ and the turbulent dissipation rate ϵ. However, the κ-ϵ turbulence model has its drawbacks with the calculation of wall effects where there is a transition from turbulent to laminar flow [COMS2017; Lech2011; Laur2018; Schw2013].

Like the κ-ϵ model, the κ-ω model is also a two-equation model. Again, the turbulent kinetic energy κ is added. The main difference is that instead of the dissipation rate ϵ, the turbulent or characteristic frequency:

$$\omega = \frac{\epsilon}{\kappa} \tag{2.10}$$

is applied [Schw2013; Lech2011]. Thus, there is a direct connection between the differential equations. Especially in the vicinity of walls, a much better description of the mean turbulence is therefore possible.

Other less common models are the v2-f model (includes two additional wall functions), the Narrow-Channel approximation (a subcategory of the laminar interface, which assumes infinite extension in the z-direction), and the Thin-Film Flow (flow in very small gaps). [COMS2017]

2.3.3. Flow Analysis Using Optimization Methods

Optimization methods are structured techniques to find the best solution to a numerical problem by maximizing or minimizing well-defined functions. In the case of expensive-to-evaluate functions, Machine Learning approaches, such as *Bayesian Optimization*, can be used. Bayesian optimization aims to find the (near) global optimum of an expensive or complex black-box function with a minimum number of steps. The objective is treated as an arbitrary function described by a simple stochastic model. In this case, the Thompson sampling efficient multi-objective optimization (TSEMO) algorithm [Brad2018], incorporating the simple, stochastic Gaussian process distribution, has shown practical applicability in optimization with CFD modeling [Bega2023]. TSEMO can handle multiple objective functions by utilizing Gaussian processes to estimate the course of the objective function. In each iteration step, the prediction is iteratively updated with new data obtained

from expensive-to-evaluate observations taken from CFD simulations of varying cell geometries. [Broc2010; Rasm2006]

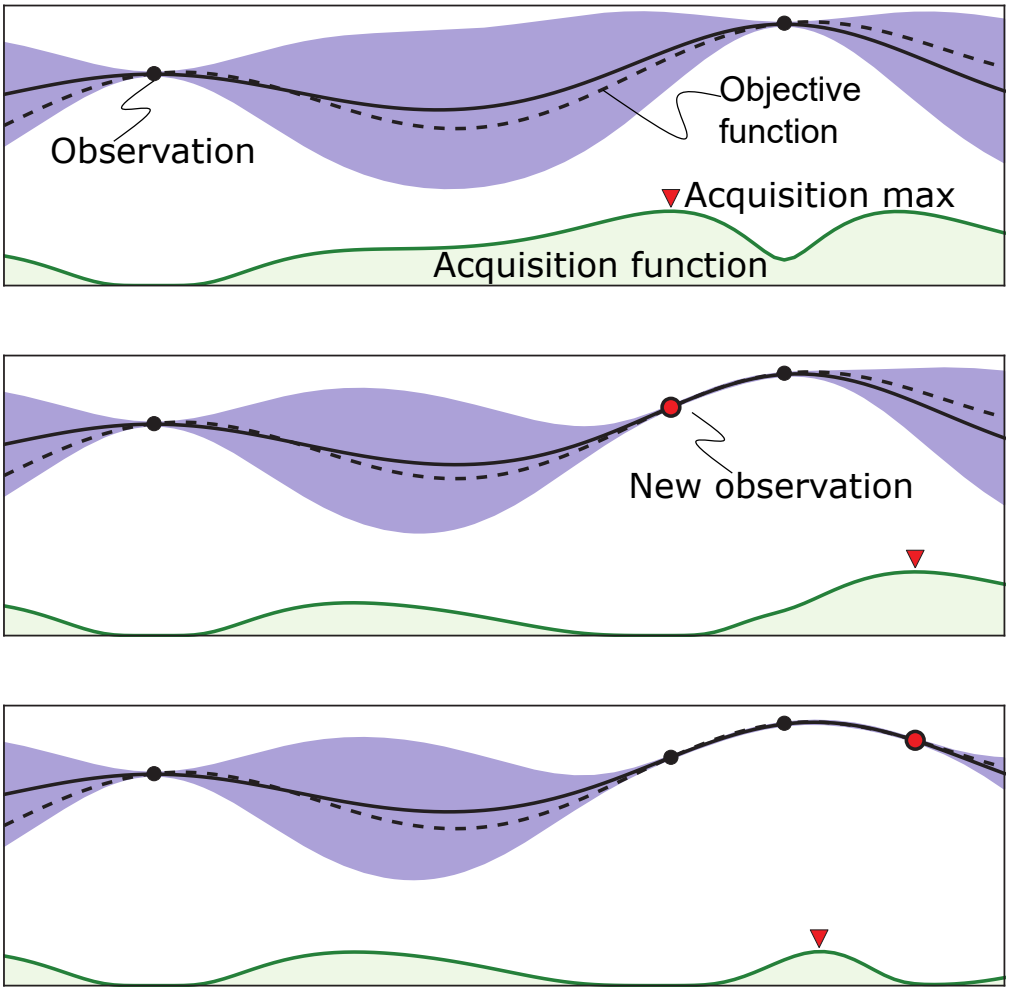

Figure 2.8.: Working principle of the Bayesian Optimization algorithm approximating a 1D problem with four iterations (adapted from [Broc2010]).

Figure 2.8 shows a typical run of Bayesian optimization on a 1D problem. The dashed black line is the objective function that shall be approximated. The solid function is the prediction originating from the optimization model with an uncertainty illustrated as blue shades surrounding the line. An acquisition function (green) helps choose the next evaluation point by elaborating the trade-off between exploration (new areas) and exploitation (based on past evaluations). At each iteration, the acquisition function is maximized to determine the next sampling point of the objective function (represented by

red markers in Figure 2.8). After each new function evaluation, the Gaussian process is updated, and the Bayesian Optimization Algorithm estimates the true objective function with increasing accuracy. The steps are repeated until a desired amount of iterations has been done, in this example, until four iterations.

In literature, the Bayesian Optimization algorithm has been applied to different geometries and CFD simulation to study reactor or flow behavior [Mori2021; Park2018; Tran2020; Tran2019; Bega2023].

2.3.4. Flow Analysis Using Other Visualization Techniques

Experimental flow investigations exist mainly for gaseous systems and natural physical phenomena like natural convection. Directed flow visualization is also known from aerospace or aircraft dynamics [Russ2011] or heat and mass transfer applications [Atki2016].

Wright et al. [Wrig2006] investigated the natural convection of air in a vertical cavity using smoke patterns and interferometry. They discovered some rotating chaotic disturbances and unsteady flow patterns. Their findings can be applied to heat and mass transfer correlations. Ahler et al. [Ahle2009] investigated turbulent Rayleigh-Bénard convection by experiment (evaluation of plume motion), theory, and numerical simulation of thermally driven flows. Qiu et al. [Qiu2001] investigated large-scale velocity structures induced by turbulent thermal convection in water-filled cells using Laser Doppler velocimetry. However, they also detected random unstable modes in a closed system rotating coherently. Bengoa et al. [Beng2000] studied flow patterns in electrochemical cells. They studied the hydrodynamics induced by different spacers in a 64 cm^2 electrolyzer by flow visualization and residence time distribution. Optical flow visualizations were carried out via a tracer point injection. They identified an asymmetric distribution of the tracer as a consequence of a velocity maldistribution due to the inlet geometry. Focke et al. [Fock1986] also investigated spacer geometries via dye injection in an industrial plate heat exchanger model showing dominant guidance of grooves in the module´s walls.

Different groups have investigated the two-phase flow in PEM fuel cells. Banerjee et al. [Bane2014] recorded videos of liquid water coverage in gas-filled cathode channels as a function of current density, temperature, and flow channel geometry. Thus, they used new algorithms developed in MATLAB to analyze the videos, quantify the liquid water, and identify the flow patterns. Dohle et al. [Dohl2003] confirmed that a homogeneous flow distribution and minimal pressure losses favor the most effective utilization of PEM fuel cells´ areas. An optical evaluation of the flow field with different diffusion characteristics revealed the time-dependent distribution of dye. Although a completely different application, Giling et al. [Gili1981] dealt with similar issues concerning the interaction of varying carrier gases (He, H_2, N_2, Ar), and the effects of turbulence, cell design and entrance effects on convective motions. They used interference holography to visualize gas flow patterns and temperature profiles in epitaxial reactor cells. Narayanan et al. [Nara2003] used infrared airflow imaging techniques on free plane two-dimensional impinging jets. The visualization technique can be used for instantaneous planar flow visualization in heat transfer applications. Xi et al. [Xi2004] experimentally examined the onset of the large-scale coherent mean flow in Rayleigh-Bénard turbulent convection via shadowgraph and particle image velocimetry techniques. They unraveled the significance of vortices and evolving plumes causing fluid entrainment, leading to a rotatory motion even in closed compartments.

Studies so far have focused on liquid flow distribution in industry electrolysis cells [Abba2008; Chav2015]. The gas compartment of different types of electrochemical cells has been optimized using serpentines, parallel channels, baffles, inlet distributors, or combinations of these techniques [Lee2013; Nie2010; Rive2015; Togh2018; Wang2020]. Previous work was not found related to optimizing the flow pattern of the gas compartment of the chlor-alkali-electrolysis cells.

3. Investigation of Switchable ODCs in Lab-Scale Electrochemical Reactors

Parts of this chapter have been published as:
Kristina Baitalow, Niklas Köller, Paul Bacmeister, Robert Keller, Matthias Wessling
On the operation of switchable oxygen depolarized cathodes, Chemical Engineering Journal, 2023
DOI: 10.1016/j.cej.2023.143759

3.1. Introduction

As introduced earlier, the integration of the switchable ODC can, in addition to enabling flexible load variations, significantly reduce energy consumption in the chlor-alkali process. Before considering scale-up and industrial application, it is essential to demonstrate that the switching between hydrogen and oxygen modes of the sODC works smoothly on a small scale. Electrochemical lab cells with active areas of a few centimeters are suitable for such tests.

This chapter explores the stability of the switchable CAE modes using a commercial, patented sODC from Covestro [Bula2017]. First, the two sODC modes, the H_2 and the O_2 mode, are intensively studied and evaluated for switchable CAE. For this purpose, the cathode and cell potential are recorded as a function of current density. Furthermore, the two modes are investigated at different electrolyte volume flows, and the O_2 mode at variable oxygen volume flows. In addition, the initial reduction process of sODC is observed in more detail to determine any detrimental consequences for the continuous operation. Finally, for the first time, a large number of 1,000 switching cycles is performed to evaluate the long-term stability of the sODC. The condition of the sODC is evaluated by means of contact angle measurements before and after the long-term experiments.

3.2. Experimentals

Oxygen evolution reaction (OER) was chosen as a substitute system to eliminate safety hazards from the chlorine evolution reaction on the anode side, see Equation 3.1. On the cathode side, ORR and HER were implemented. As this study focuses on the stability and durability of the cathode, substituting the anode reaction is justified because the cathode reactions 2.2 and 2.3 at the sODC are not affected as the used membrane facilitates OH^- transport but blocks gas exchange.

$$4OH^- \rightarrow O_2 + 2H_2O + 4e^- \qquad \text{(Anode, OER, this study)} \qquad (3.1)$$

A schematic of the process is shown in Figure 3.1. Switching between H_2 and O_2 mode is interrupted by nitrogen (N_2) flushing of the gas compartment between the sODC and the cathodic current collector. Figure 3.1 a) shows the H_2 mode with hydrogen evolution in times of energy surplus and low or even negative electricity prices. Figure 3.1 c) indicates the O_2 mode with oxygen consumption at the cathode at times of high electricity prices. To prevent an explosive atmosphere, a nitrogen flush is applied between both modes every time before switching, indicated by Figure 3.1 b).

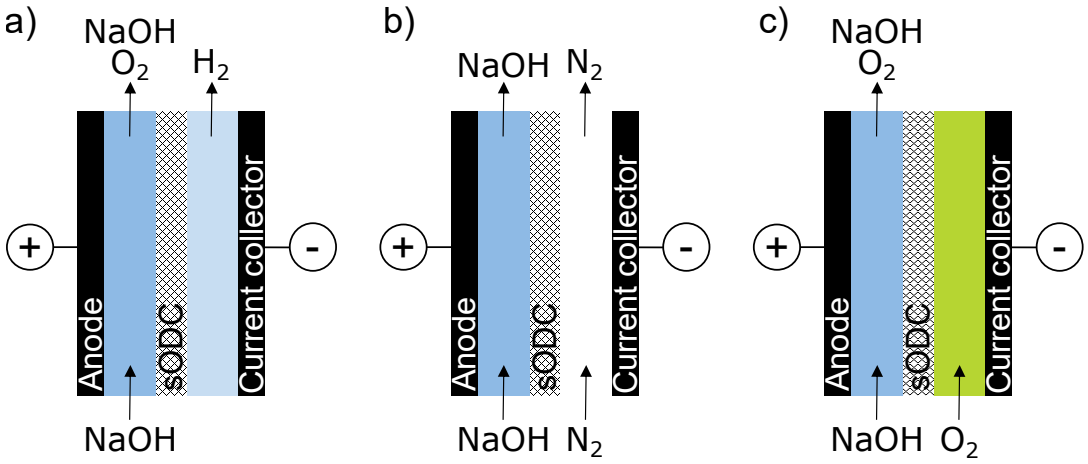

Figure 3.1.: Cell setup with a liquid and a gas compartment with a) HER, b) nitrogen flush, and c) ORR in the gas compartment.

3.2.1. Cell Design

In the first step, a 1st generation cell was implemented as a divided cell with an ion exchange membrane as a separator and tested in electrochemical experiments. Subsequently, experiments at high current densities, concentrations, and temperatures led to a 2nd generation cell without a membrane but a shared electrolyte space to enhance gas bubble removal. A membrane was not essential to separate the electrolytes since the same electrolyte at the anode and the cathode were used. Nagai et al. [Naga2003] reported an electrode-gap optimum and efficiency benefit without a separator by avoiding gas trapping of evolving gas bubbles. Experiments were performed in both cell designs and are discussed comparatively.

In both cells, the geometric area of the cathode was 30 mm x 40 mm. An sODC (Covestro AG, Leverkusen GER) separated the catholyte from the gas compartment on the cathode side. The sODC consisted of polytetrafluoroethylene (PTFE), silver and ruthenium catalyst on an electrically conductive nickel mesh [Bula2017]. Gas evolution (HER) occurred on the back of the sODC in a separate gas compartment of 4 mm depth (see Figure 3.1). The cell was operated in crossflow mode, with the electrolytes flowing from bottom to top and the gas flowing from top to bottom. A 1.5 mm thick PTFE spacer, called catholyte spacer, was used as a stabilizer of the catholyte flow channel holding the sODC in place.

1st Generation Cell

In the 1st generation cell, experiments were conducted with a reinforced anion exchange membrane (AEM, FUMASEP FAB-PK-130, Fumatech, Bietigheim-Bissingen GER) to separate the electrolytes as in the industrial application and to distinguish between oxygen evolution at the anode and possible gas crossover through the sODC at the cathode.

Meander-shaped inserts made of stainless steel were inserted into both half cells as flow channels and current collectors. On the anode side, the anolyte flowed through the meander insert, which was covered by a nickel mesh (Ni-2733 by Recemat BV, Dodevard NL; average porosity 95.2 %) as anode; on the cathode side, the meander insert represented the gas compartment. The sODC was placed directly on the meander insert and sealed with gaskets towards the catholyte. A Haber-Luggin capillary was used to connect a reference electrode to the cell. Therefore, a 1 mm Nafion® tube was placed in a borehole leading from the back of the anode compartment to an opening in the direct vicinity of the membrane (adapted from [Venn2019b]). The Nafion® tube was then led to a vessel where a reference electrode was placed (see Section 3.2.2 for reference electrode details). The Nafion® tube was filled with the same electrolyte as the reference electrode. The 1st generation cell design was used to assess the potential difference between O_2 and H_2 modes and to verify the

suitability of the setup for the long-term switching experiments.

2nd Generation Cell

The increase in gas evolution due to high current densities is extensively discussed in literature [Haug2017b; Haug2017a; Roy2006; Balz2003]. In order to overcome challenges associated with gas removal at high current density, the membrane was omitted in the 2nd generation cell. Hydrogen cross-over to the anode from the cathode side was prevented, as hydrogen was released on the back side of the sODC. Electrolyte mixing of anolyte and catholyte due to the missing membrane was not detrimental since the same electrolyte was used for the anolyte and catholyte. Figure 3.2 shows the elements of the electrochemical cell with rigid metallic end plates, anode and cathode half cells made of PTFE, the anode, the catholyte spacer, the sODC with the current collector and a polymethyl methacrylate (PMMA) window at the back of the gas compartment (sealings were left out in the overview). The meander-like inserts were replaced by a frame-like current collector made of nickel alloy 201 (Nickel 201, Alloy Shop, London UK) to provide electrical contact with the sODC via a lateral bar. This helped to reduce the total cell thickness and to improve stability. A plate made of nickel alloy 201 was used as anode. The electrode distance amounted to 4 mm. A T-junction made of PTFE was placed directly in front of the catholyte inlet containing the reference electrode and flushed with the catholyte entering the cell (see Section 3.2.2 for reference electrode and electrolytes).

3.2.2. Experimental Setup

All cell elements in contact with the electrolyte were cleaned with deionized water before and after usage. Solutions of sodium hydroxide (CAS-No. 1310-73-2, NaOH beads $\geq$99 %, Carl Roth, Karlsruhe GER) were freshly prepared with deionized water. 1 M NaOH was used as electrolyte. The electrolyte was mixed in the reservoir vessel to compensate for concentration differences and to balance the trend of different electrolyte levels over time according to [Haug2017a]. The used gases were oxygen 3.5 (ISO 14175-0-0,

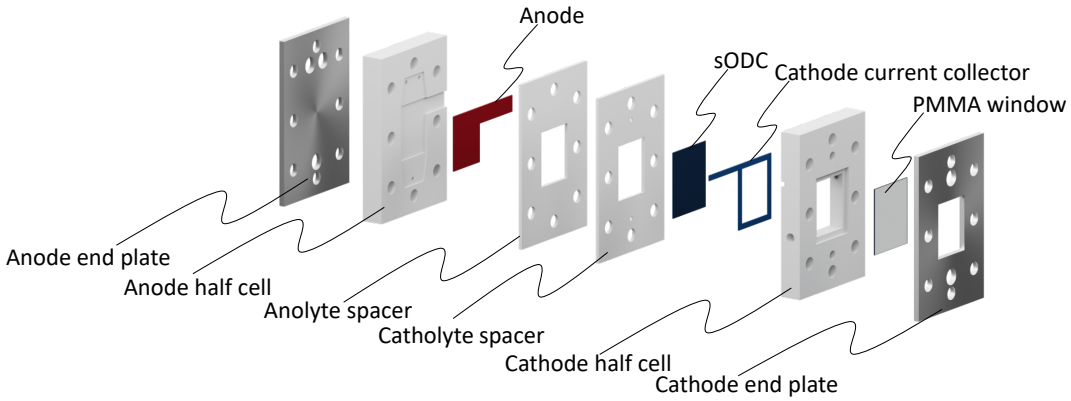

Figure 3.2.: Elements of the 2nd generation electrochemical cell with metal end plates, PTFE half cells, electrolyte spacers holding the anode and sODC in place, a cathode current collector for electrical connection and a PMMA window at the backside of the sODC.

Westfalen AG, Münster GER) for the O_2 mode of the sODC and nitrogen 5.0 (ISO 14175-N1-N, Westfalen AG, Münster GER) for flushing. The used reference electrode was a Hg/HgO electrode (Meinsberg HgO11-S with 1M NaOH electrolyte filling, Xylem Analytics, Weilheim GER).

Figure 3.3 shows the flow diagram of the cell implemented in the setup. A peristaltic pump (MCP-Process IP65, ISMATEC® Cole Parmer GmbH, Wertheim GER) provided the electrochemical cell with a constant electrolyte flow rate of 5 L h^{-1}. Several tubes (TYGON® A-60-F, ProLiquid, Überlingen GER) connected the peristaltic pump with the electrolyte reservoirs. A mass flow controller (Type 8711, Bürkert Fluid Control Systems, Ingelfingen GER) controlled the gas flow. The entering gas was humidified via a gas-washing bottle filled with deionized water. Back pressure could be adjusted at the outlet of the gas compartment via a water column filled with up to 50 cm of water. Temperature sensors (FieldPoint FP-TC-120, National Instruments Corp., Austin TX USA) and pressure sensors (S10, A-10, and IS-10, WIKA Alexander Wiegand SE & Co. KG, Klingenberg GER) were used to monitor process conditions. The pressure sensors were used for interim pressure tests to check the pressure drop in the liquid channel across the laboratory cell. No irregularities were detected; hence, the pressure sensors were not

installed for the subsequent measurements. A manual bubble flow meter (Supelco 10CC EA, Merck KgaA, Darmstadt GER) was used to measure the gas volume flow at the cell outlet. A DC power source (MCS-3202, Manson Engineering Industrial Ltd, Hongkong HK) provided a constant current. Voltages were measured via a multimeter (Voltcraft VC 850, Conrad Electronic SE, Hirschau GER). The cell temperature was controlled via the electrolyte cycle heated in the reservoir vessel. A heating plate with temperature control set the electrolyte temperature to a constant 30 °C. A LabVIEW application automatically controlled the experimental devices.

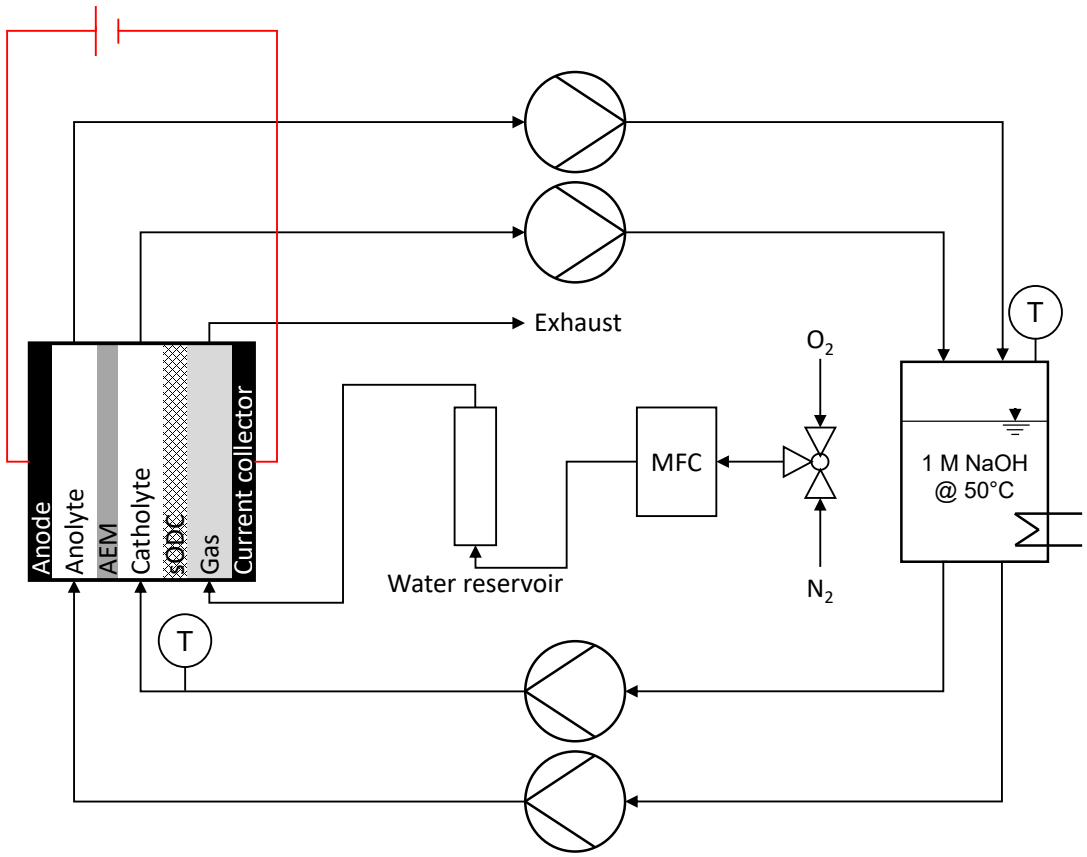

Figure 3.3.: Flow diagram of the experimental setup showing two electrolyte cycles, a gas cycle, the gas supply, a two-channel liquid pump, a mass flow controller, storage tanks and several sensors.

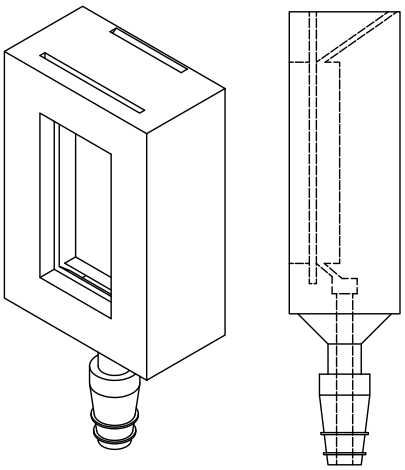

Figure 3.4.: 3D-printed beaker cell used in the beaker experiments.

3.2.3. Electrochemical Measurements

sODC Reduction Process Experiments with gradually increasing current density were conducted in a beaker to record the cell potential over time and evaluated to understand the sODC reduction process better. Additionally, the color change of the sODC during the initial start-up (reduction process) of a pristine sODC was observed visually. Both H_2 and O_2 modes were investigated in the beaker experiments. For the H_2 mode, an sODC (20 mm x 10 mm) was submerged in 1M NaOH and a nickel mesh served as an anode. Figure 3.4) shows the self-made and 3D-printed beaker cell to run the O_2 mode with an oxygen supply. The geometry had a slit for mounting the sODC and a gas compartment for the constant oxygen supply. The whole geometry was submerged in caustic soda. The experiments for both reaction modes were conducted at different current densities up to 400 mA cm^{-2}. The current was turned on immediately. The subsequent color change from black (pristine) to white (reduced) was observed via a Nikon D750 camera.

Galvanostatic Methods and Electrochemical Impedance Measurements The setup allows for measuring the cell potential at different current densities, the cathode potentials, and Faraday efficiencies. Investigations of the H_2 and the O_2 modes of the sODC were based on chronopotentiometry

(CP) measurements using the 1st generation cell. The overall cell potential was measured at current densities of 50 mA cm^{-2} to 250 mA cm^{-2} via the multimeter in the 2nd generation cell. The cathode potentials (potential between cathode and reference electrode) were measured at current densities 50 mA cm^{-2} to 525 mA cm^{-2} with a potentiostat (VSP, Biologic, Göttingen GER) vs. Hg/HgO reference electrode in the 2nd generation cell. The potential measurements of the least 30 s of each stage were averaged to evaluate the cathode potential. The values were corrected to the RHE scale and iR-drop compensated. The measured cathode potential vs. Hg/HgO reference electrode was corrected to obtain potentials vs. RHE as follows:

$$\begin{aligned} \text{U vs. RHE} &= \text{U vs. SHE} + (0.0591\,\text{V} \cdot pH14) \\ &= 0\,\text{V} + 0.8274\,\text{V} \\ \text{U vs. SHE} &= \text{U vs. Hg/HgO} + 0.14\,\text{V} \end{aligned}$$

$$\begin{aligned} \text{U vs. RHE} &= \text{U vs. Hg/HgO} + 0.14\,\text{V} + 0.8274\,\text{V} \\ &= \text{U vs. Hg/HgO} + 0.967\,\text{V} \end{aligned}$$

iR-drop was obtained via Galvanostatic Electrochemical Impedance Spectroscopy (GEIS) measurements. GEIS measurements were measured at 0 mA bias current, 10 mA amplitude and frequency ranging from 1 kHz to 100 kHz. The intercept of the real axis determined the ohmic resistance of the electrolyte.

The Faraday efficiency (FE) was evaluated in galvanostatic operation by measuring the volumetric gas flow rate at the cell outlet with a manual bubble flow meter. Thus, pure gas streams were assumed at the anode and cathode outlets. Switching experiments were paused to measure FE in between and continued afterward. The theoretical gas consumption was calculated using the entering gas flow rate, Faraday's and ideal gas law for the analysis of the FE. The mean temperature at the gas outlet was used as a reference. For the H_2 mode, the flow rate of the hydrogen produced in the reaction was measured. For the O_2 mode, the consumption of the oxygen gas flow was evaluated.

Varying Process Parameters Before examining the switchability of the modes, the dependence of the cell potential on flow parameters was investigated. The cell potential was measured in H_2 and O_2 modes at varying electrolyte flow rates and only for the O_2 mode at different oxygen flow rates. First, the catholyte volume flow rate was investigated in a range relevant to the application. For this purpose, typical electrolyte flow rates from different studies and empirical values from industry were used. The electrolyte flow rates varied between $2\,\mathrm{L\,h^{-1}}$ to $5\,\mathrm{L\,h^{-1}}$. Second, oxygen flow rates were run at various over-stoichiometric multiples. The flow rates varied between $12\,\mathrm{mL\,min^{-1}}$ to $50\,\mathrm{mL\,min^{-1}}$ at $250\,\mathrm{mA\,cm^{-2}}$. For this purpose, the stoichiometrically required oxygen flow rate was calculated. Using Faraday's law and replacing the charge Q by the product of (constant) current and time, dividing by time, and using the Ideal Gas Law (1 atm, 25 °C), the stoichiometrically required oxygen volume flow can be calculated:

$$
\begin{aligned}
Q &= n \cdot z \cdot F \\
n &= \frac{Q}{z \cdot F} = \frac{I \cdot t}{z \cdot F} \quad 3\,\mathrm{A} \text{ at } 12\,\mathrm{cm^2} \text{ geometrical area} \\
\frac{n}{t} &= \frac{I}{z \cdot F} = \frac{3\,\mathrm{A}}{4 \cdot F} = 7.77 \times 10^{-6}\,\mathrm{mol\,s^{-1}} \\
&\text{With the Ideal Gas Law: } \dot{V} = \frac{\dot{n} \cdot R \cdot T}{p} \\
&= \frac{7.77 \times 10^{-6}\,\mathrm{mol\,s^{-1}} \cdot 8.3145\,\mathrm{N\,m\,mol^{-1}\,K^{-1}} \cdot 300\,\mathrm{K}}{101\,325\,\mathrm{N\,m^{-2}}} \\
\dot{V} &= 1.9 \times 10^{-7}\,\mathrm{m^3\,s^{-1}} = 11.5\,\mathrm{mL\,min^{-1}}
\end{aligned}
$$

3.2.4. Switching Cycle Automatization

The following considerations mimic industrial operation: 12,000 hours are assumed as a reference runtime (= 500 days, comparable to [Kiro2006; Kiro2008; Furu2000; Sira2008]). One mode should be in operation for at least six hours with an additional 30 min for flushing and setup time, and a switching cycle consists of the two modes running after each other, so 13 h in total. This results in a total of 923 cycles. Studies show that, in reality, switching is expected less often than every six hours [Brée2019].

However, as a first long-term evaluation, the cell potential was evaluated over 1,000 switching cycles between H_2 and O_2 mode, exceeding the suggested 500 days. This cycle number can be adapted for further detailed investigations. The parameters for the switching procedure were selected based on industrially relevant conditions.
After each cycle, flushing with nitrogen was carried out to accomplish a safe operation without the formation of explosive gas mixtures. Figure 3.5 shows a sketch of the switching procedure with an example of the applied current density (blue) and the corresponding cell potential (black) over time. The ramp-up of the current density was carried out in three steps. The current density was set to zero during flushing and O_2 filling. After an initial flush with nitrogen for 30 s, the cell was run in H_2 mode at 670 mA cm^{-2} for 90 s. Subsequently, the cell was flushed with nitrogen for 45 s, and the cell was filled with oxygen for 60 s. Then, the second mode, the O_2 mode, was run at 670 mA cm^{-2} for 90 s. Finally, the switching cycle was terminated with a final nitrogen flush for 45 s. The procedure was repeated, starting from the H_2 mode and running repetitively.

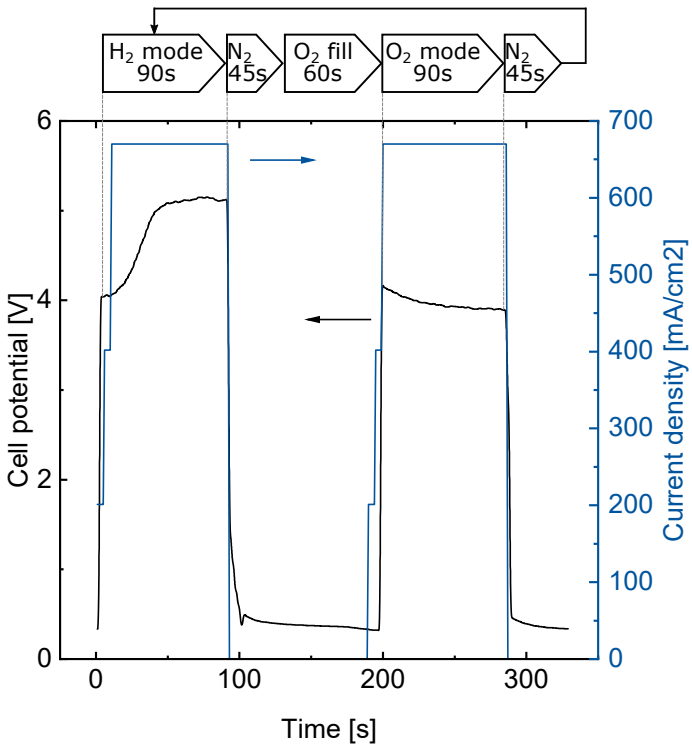

Figure 3.5.: Schematic procedure of a switching cycle and an example of the current density applied (blue) and the corresponding cell potential of H_2 mode, N_2 flushing, O_2 filling and O_2 mode black (current density is ramped up in three steps).

The current density was set to 670 mA cm^{-2}, resembling industrial values. The electrolyte volume flow rate of 5 L h^{-1} was selected to ensure sufficient overflow and good removal of gas bubbles. The resulting electrolyte velocity of approximately 18 mm s^{-1} is comparable with literature values (1.4 mm s^{-1} to 3.6 mm s^{-1} [Haug2017a], 22 mm s^{-1} to 84 mm s^{-1} [Jala2009]). The stoichiometric oxygen flow rate required for a current density of 670 mA cm^{-2} was calculated to be 30.6 mL min^{-1}. It was exceeded by a factor of 2.6 to 80 mL min^{-1} to ensure an over-stoichiometric supply. The same value was chosen for nitrogen volume flow. The temperature was set to 30 °C for the switching cycles. For stability reasons, 1 M NaOH was chosen. The experimental parameters are summarized in Table 3.1.

Contact angle measurements were conducted on a Krüss DSA10-Mk2 tensiometer before and after the switching cycle sequence. Liquid drops were applied onto the sODC with a PTFE cannula (0.5 mm diameter) and filmed with an integrated camera. At least five drops of DI water were

Table 3.1.: Experimental conditions of the long-term switching experiments.

Parameter	Value
Current density [mA cm^{-2}]	670
Electrolyte volume flow [L h^{-1}]	5
Gas volume flow [mL min^{-1}]	80
Temperature [°C]	30
Electrolyte	1 M NaOH

analyzed with the *Tangent-1* method supplied by the device's software and averaged afterward. Contact angle measurements were also run with 1 M NaOH but showed no remarkable deviations and are therefore not shown here. The sODCs were dried for four hours before the measurements for a uniform initial reference. The tests were conducted on the electrolyte-facing side of the sODCs. The results were compared to those of a fresh sODC to characterize possible degradation phenomena.

3.3. Results and Discussion

3.3.1. sODC Reduction Process

The sODC reduction process is investigated at different current densities up to 400 mA cm^{-2}. Color change of the sODC is observed during the initial operation. This color change is attributed to the reduction of silver oxide to silver according to Equation 3.2 and occurs during HER and ORR.

$$2\,Ag_2O \longrightarrow 4\,Ag + O_2 \tag{3.2}$$

Figure 3.6 shows an exemplary series of pictures taken during a beaker experiment at a current density of 50 mA cm^{-2}. The upper row shows the sODC in H_2 mode (no oxygen supplied) after 10, 60, and 80 min during the experiment. The lower row shows the same time steps of the sODC in O_2 mode with oxygen fed to the backside of the sODC via the beaker cell. In

both cases, the color changes at a few small spots first and then spreads irregularly until the entire sODC is colored white. In H_2 mode, hydrogen bubbles start forming at the sites which have already turned white. The color changes faster at higher current densities: At 200 mA cm^{-2}, it takes 18 min to complete the change in H_2 mode, at 300 mA cm^{-2} 10 min and at 400 mA cm^{-2} 5 min.

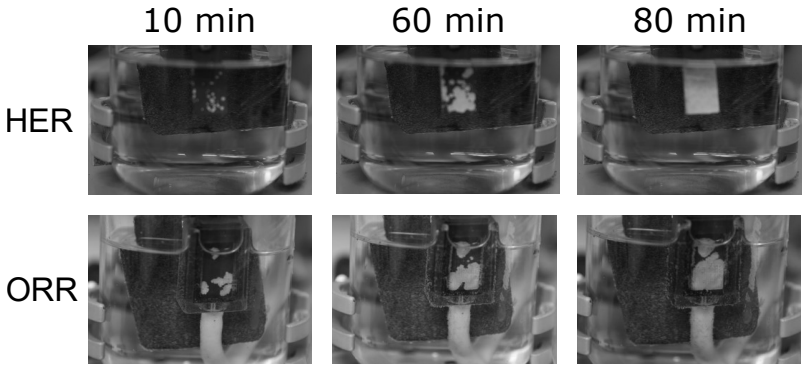

Figure 3.6.: Images taken during beaker experiments after 10, 60 and 80 min (from left to right) at HER (upper row) and ORR (lower row). Applied current density: 50 mA cm^{-2}.

The accompanying cell potential measurement underlines the presumed initial reduction process (see Figure 3.7). The corresponding patent for the sODC used here states that a considerable amount of silver oxide could be contained [Bula2017]. For non-disclosure reasons, more detailed investigations of the composition cannot be carried out. Nevertheless, the results show that the initial reduction process of a pristine sODC is inevitable and that the structure or the characteristics of the sODC change visibly under the influence of the current.

3.3.2. Electrochemical Potentials of ODCs

The cell potentials of the two reactions in the H_2 and O_2 modes of the sODC were examined for their potential difference and, thus, suitability for energy saving. Furthermore, the O_2 mode of the conventional was compared with the switchable ODC. Finally, cathode potentials of both modes of the sODC were used to estimate the overpotentials as a function of increasing current

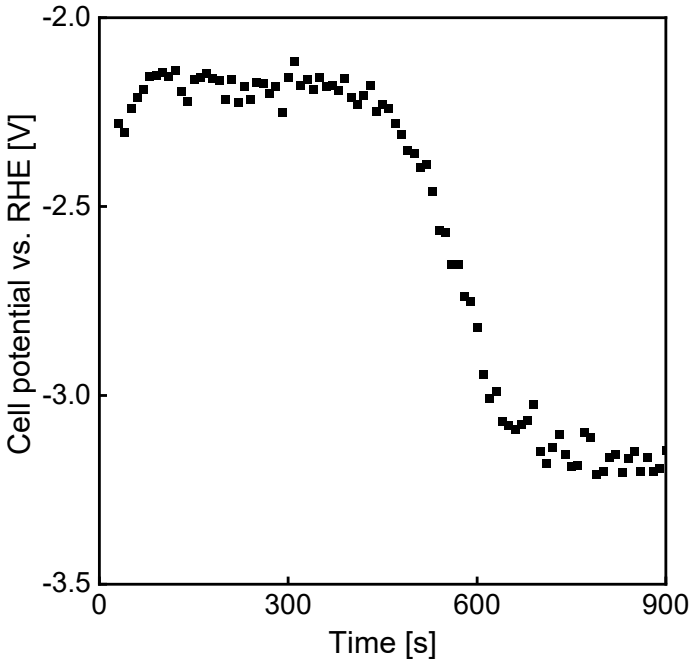

Figure 3.7.: *Chronopotentiometry of initial reduction process of sODC operation revealing a change in cathode potential (applied current density: 250 mA/cm^2.)*

density.

Cell Potential

Figure 3.8 shows measured cell potentials for the sODC (empty circles) and the conventional ODC (crossed circles) for current densities 50 mA cm^{-2} to 250 mA cm^{-2} using the 1st generation cell and CP methods. Both the conventional ODC and the sODC achieved similar cell potentials in the O_2 mode with a maximum difference of 0.07 V. This difference confirms the good performance of the sODC and its prospect of substituting the conventional ODC. Cell potentials cannot be compared with the literature at this point since values relevant to ODC are found with chlorine evolution on the anode side and not with oxygen evolution, as in the case at hand. Additionally, the electrolyte gap and membrane type vary.

Figure 3.8 shows an average increase in cell potential of +1.26 V from O_2 to H_2 mode, which corresponds well to the theoretically expected potential difference of +1.23 V between ORR and HER [Step2005]. Regarding energy savings, the cell potential drop equals 45 % when switching from H_2

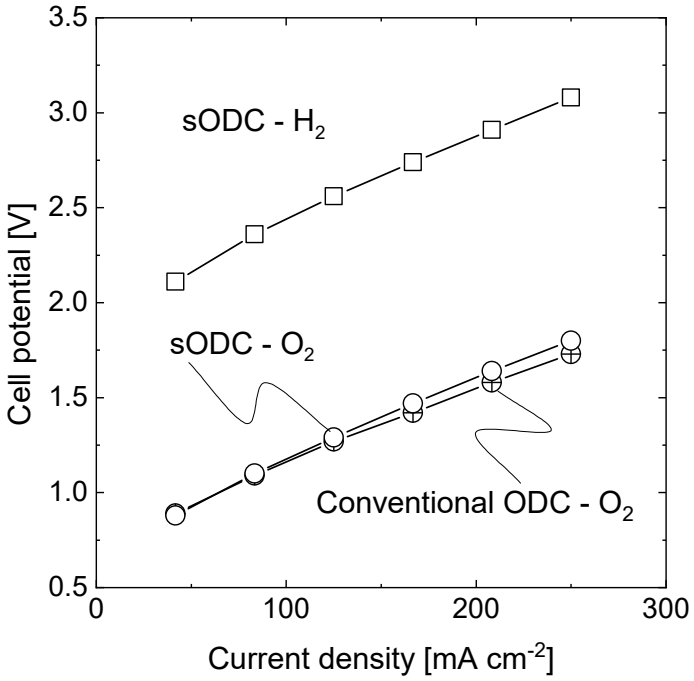

Figure 3.8.: Cell potentials of the O_2 and H_2 mode of the sODC and the O_2 mode of the conventional ODC.

to O_2 mode at 310 mA cm^{-2} in the replacement system water electrolysis. The here calculated percent savings in the replacement system are based on a cell potential in water electrolysis of around 2 V, while comparisons in CAE obtain lower percent savings due to the higher total cell potential of approximately 3 V. CAE-related studies compared the oxygen-consuming mode with the conventional hydrogen-evolving cathode in the chlorine evolution process. They observed similar potential savings (30 % to 38 % at 300 mA cm^{-2} [Kiro2006], 30 % to 35 % at 300 mA cm^{-2} [Kiro2008], around 30 % at industrial current densities [Jöri2011; Kint2017], a 42 % reduced energy demand between a graphite (hydrogen-evolving) cathode and a copper-doped ODC [Figu2013]). The cell potential decrease explains the lower energy consumption of the O_2 mode. Still, a more detailed investigation of investment and operational costs is necessary to clarify the economic efficiency and can be found elsewhere (see [Kint2017; Jöri2011; Brée2019; Brée2020] for further investigations).

Cathode Potential

Figure 3.9 displays the cathode potential vs. reversible hydrogen electrode (RHE) of the sODC as a function of current density varying between 50 mA cm^{-2} to 525 mA cm^{-2} using the 2nd generation cell. Measurements are averaged over the last 30 s of each CP step and iR-corrected using GEIS results. Deviations were determined as the minimum and maximum values. Subsequently, the calculated cathode potentials were used for a more detailed decomposition of the individual overpotentials and to calculate the current-dependent iR drop.

Figure 3.10 shows the summation resulting in the total cell potentials for the O_2 and the H_2 mode. The overpotential estimations were obtained from the Chronopotentiometry (CP) measurements with a potentiostat (VSP, Biologic, Göttingen GER). The Hg/HgO reference electrode was placed directly before the anolyte or the catholyte inlet. Both electrode overpotentials and the remaining overpotential could be obtained by alternating between the two positions. For this evaluation, the theoretical equilibrium potential, overpotentials at the electrodes, and resistances from electrolytes and membrane were estimated based on the electrochemical measurements. Due to the higher equilibrium-potential difference and higher overpotentials of the hydrogen-evolving cathode in the H_2 mode, the total cell potential is higher than in the O_2 mode.

Electrode overpotentials were corrected by the iR drop between the reference electrode and the corresponding working electrode using the electrochemical impedance measurements. Overpotentials at the electrodes increase from low current densities to higher current densities of 525 mA cm^{-2} (ORR: 0.51 V at the cathode, HER: 0.72 V at the cathode, 0.55 V at the anode in both reactions). Jörissen et al. [Jöri2011] reported a similar ORR cathode overpotential of approximately 0.65 V at 550 mA cm^{-2}. They assumed a higher cathode overpotential for ORR than HER. However, the measurements reported here showed a higher overpotential for HER, possibly because the Ag-Ru-containing sODC is not optimal for HER. Another critical difference is the active provision of oxygen in the ORR compared to the hydrogen produced in the HER. The evolving hydrogen must

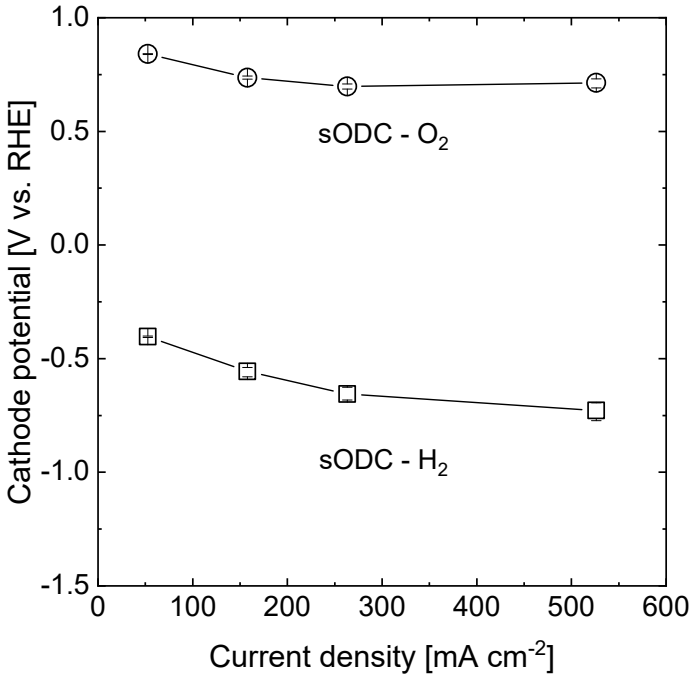

Figure 3.9.: sODC shows a potential difference between H_2 and O_2 mode (1st generation cell design with Fumasep FAB-PK-130 anion exchange membrane).

first escape from the pores of the sODC. Bubble entrapment could result in higher overpotentials.

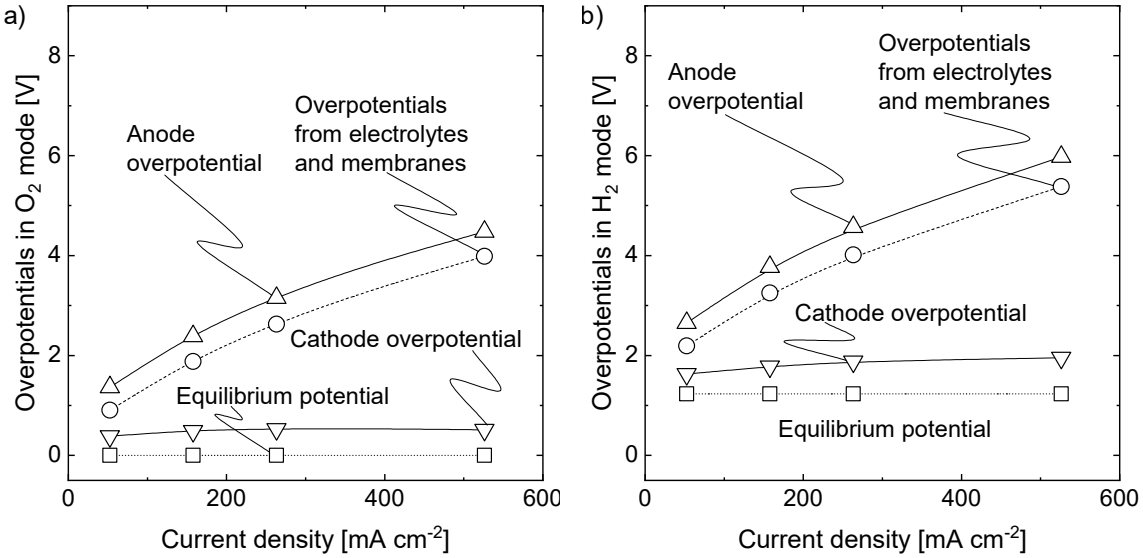

Figure 3.10.: Overpotential compositions of the two modes consist of the anode overpotential △, iR drop of electrolytes and membrane ◯, and the cathode overpotential ▽, added to the equilibrium potential □ in a) O_2 mode, and in b) H_2 mode.

A direct comparison of cathode potentials of the same electrodes from

literature is challenging, as ODC investigations often focus on different material combinations, and thus ODC composition varies significantly. In this thesis, the sODC composition is fixed and most comparable to a patent of Covestro [Bula2017]. Cathode potentials reported in Figure 3.8 differ by an additional 0.279 V [Bula2017] for HER and by an additional 0 V to 0.17 V [Bula2017; Mous2012; Gebh2019; Furu2000] for ORR compared to this thesis' values (see chapter 2.2.3 for further details). In both cathode reactions, the presented results show higher overpotentials, which may originate from the catalyst, lower electrolyte concentration, or lower reaction temperature. Future research could focus on the correlation between the specific composition and the resulting overpotentials.

However, few studies directly address both cathode reactions, and none measure cathode potentials at the same bi-functional cathode. Instead, cathode potentials of ORR or HER are measured at cathodes optimized for each reaction. These studies have confirmed that cathode potentials are significantly lower for the O_2 mode than for the H_2 mode, and values are comparable to the study at hand [Kiro2006; Kiro2008; Figu2013; Mori2000]. In this thesis, one electrode has to catalyze both reactions. This leads to performance limitations, further discussed in the following subchapters.

Influence of Process Parameters

Figure 3.11 a) shows that the catholyte volume flow rate does not influence the cell potential in the range 2 L h^{-1} to 5 L h^{-1}: both H_2 and O_2 modes show a linear and uniform increase in cell potential for increasing current densities between 50 mA cm^{-2} and 250 mA cm^{-2}.

Figure 3.11 b) shows that the O_2 mode shows no further dependence on the oxygen volume flow rate above a minimum stoichiometric oxygen supply of 12 mL min^{-1}.

Above a specific minimum requirement, the catholyte and oxygen volume flow variations show no significant influence on the cell or the cathode potential. This output was considered when choosing the process parameters for the switching cycles experiments (see Chapter 3.2.4).

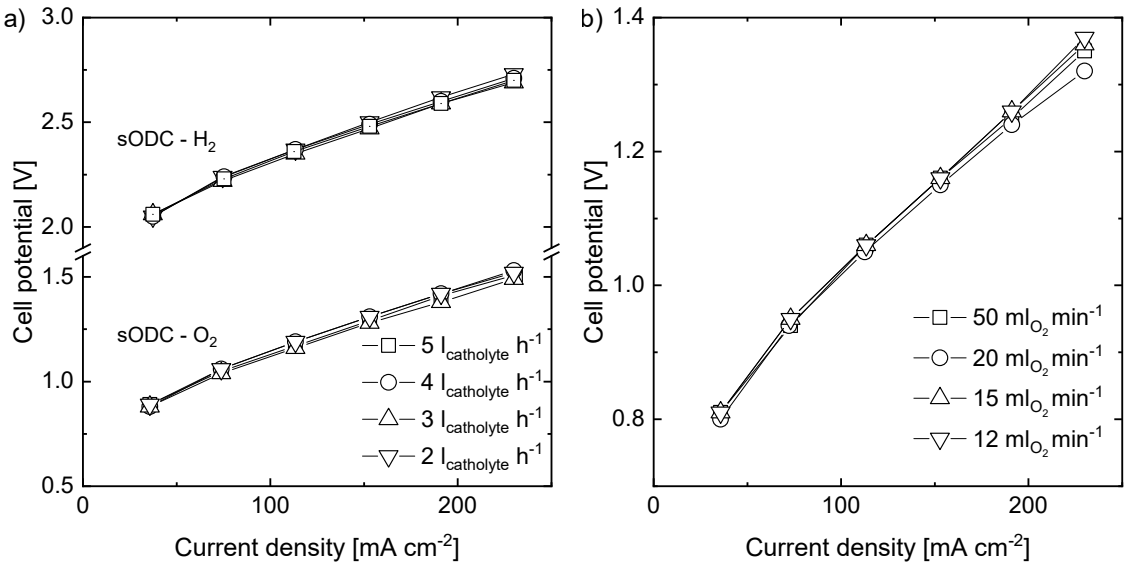

Figure 3.11.: Cell potential as function of a) catholyte flow rate and b) oxygen flow rate.

3.3.3. Long-Term Stability after 1,000 Switching Cycles

The electrochemical analysis described so far addresses a single switching operation comparing O_2 and H_2 modes. However, to assess the industrial relevance of sODC, numerous switching cycles without significant loss in performance must be demonstrated.

Long-term experiments of up to seven days aimed to verify the stable performance of the sODC. A LabVIEW software ran 1,000 automated switching cycles between H_2 and O_2 mode according to the procedure shown in Figure 3.5. For closer evaluation, the switching cycle number was extended to 1,600. The cell potential was recorded over time for a fixed current density of 670 mA cm^{-2} and 1 M NaOH as electrolyte. The mean average of the last 30 s of each switching interval was calculated to evaluate the course of the cell potential. Figure 3.15 shows the mean average of cell potentials for every 100 cycles and each reaction separately.

1st Generation Cell

After separately investigating the O_2 and the H_2 mode, the 1st generation cell was used for the long-term experiments. However, fluctuations and a

strong overall increase in cell potential for both reactions were observed over time during the first experiments. Figure 3.12 a) shows that the cell potential increased by 18.2 % for the H_2 mode (black) and by 22.3 % for the O_2 mode (blue) over 1,600 switching cycles. At the same time, a large amount of leaked electrolyte was detected on the gas side of the sODC, which was returned to the vessel during operation. However, the amount of leaked electrolyte remained approximately the same. Besides, intense gas evolution was observed and associated with higher current densities.

Faraday Efficiency (FE) was measured initially, after 500 and after 1000 switching cycles. Despite the leaking electrolyte, the FE values remained consistently high (see Figure 3.12 b). The FE of the H_2 mode (black) and the O_2 mode (blue) over 1,600 switching cycles remains high. Therefore, most likely, the leakage has no permanent detrimental effect on the sODC performance but leads to a temporary shielding of the active area during the experiment and thus to the cell potential increase.

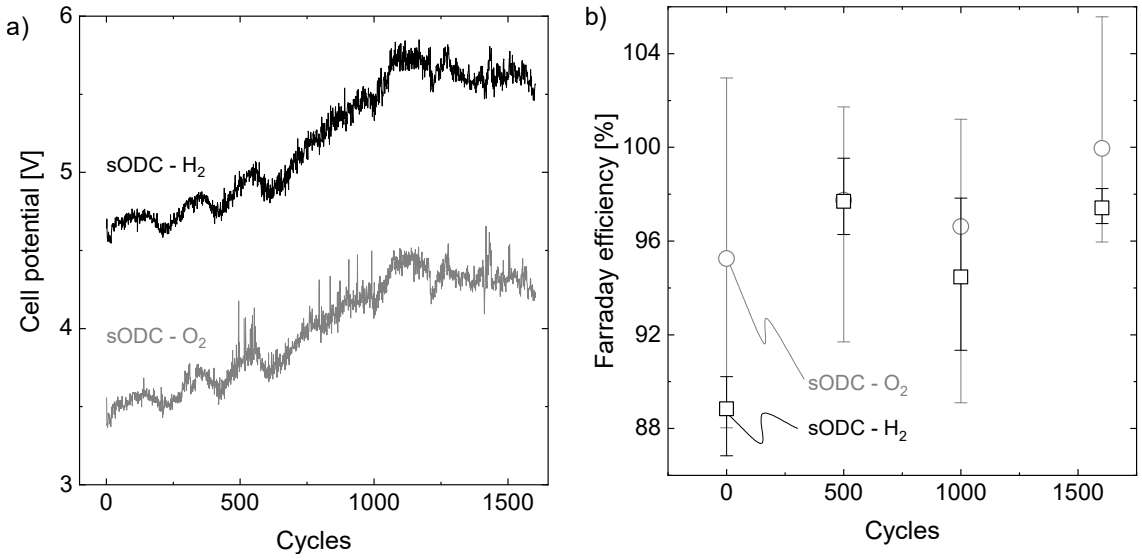

Figure 3.12.: Using the 1st generation cell, a) Cell potential of the H_2 mode (black) and the O_2 mode (blue) over 1,600 switching cycles; b) FE increases only slightly over first cycles and stabilizes between 500 and 1,600 cycles.

In the following, an explanatory approach based on observations of a pristine sODC compared to an sODC after switching cycles is presented.

Maintaining a stable three-phase boundary in the catalytically active zone of the gas diffusion electrode is crucial for the best performance of the

CAE process [Mous2008; Jöri2011; Kint2017; Röhe2019a]. Both the breakthrough of gas to the liquid side and the leakage of catholyte to the gas side have a detrimental effect on the sODC and must be avoided [Mous2008; Jöri2011]. Especially in the described long-term testing, the perpetuation of this sensitive equilibrium is indispensable. On one side, neither the produced hydrogen nor the supplied oxygen must enter the gap between the sODC and the membrane, as this would increase the resistance and block catalytically active surface area. On the other side, electrolyte penetrating the gas compartment could lead to salt precipitation from the electrolyte and, thus, pore blockage, corrosion, and shielding of the active catalytic surface. In both cases, the consequences can lead to an increase in cell potential and diminish the overall efficiency and hence should be avoided. [Bula2017; Furu2000]

During the 1,600 switching cycles, a significant breakthrough of catholyte to the gas side of the sODC of several 100 mL was observed, which was recycled back to the reservoir. pH measurements of the leaking catholyte revealed a roughly 20 % higher concentration of NaOH than the reservoir solution. This observation was also observed by Furuya et al. [Furu2000]. In several experiments of this study, leakage was observed to depend on flow conditions (e.g., use of spacers, electrolyte gap, insufficient catholyte level in the electrolyte gap) or cell assembly (e.g., repositioning sealings). Electrolyte leakage was observed to cause sharp increases in cell potential by up to 1 V to 3 V. The rise was attributed to a disturbance of the three-phase equilibrium and, thus, an increase of the diffusion path of oxygen to the active sites and increased resistance for the removal of hydrogen bubbles. Therefore, prevention of electrolyte breakthrough is paramount for the process. In industrial cells, electrolyte breakthrough is prevented by installing a falling film [Kint2017; Jöri2011]. Contact angle measured ex-situ (see Figure 3.13) declined with increasing switching cycles, with the lowest value after 1,000 cycles. The observed decreasing contact angles can be attributed to a decreasing PTFE content and, thus, decreasing hydrophobicity [Kuwe2016; Wagn2004]. Decreasing hydrophobicity can favor pores to be flooded by the electrolyte. This explains why the cell

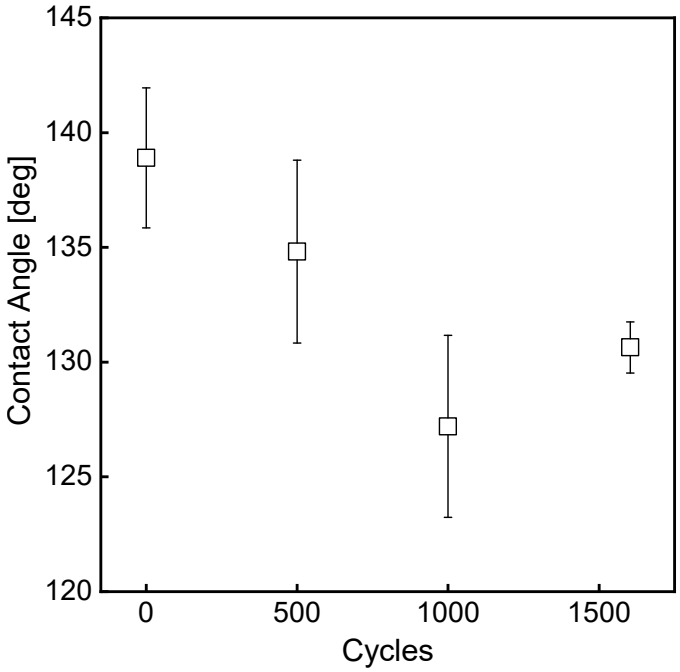

Figure 3.13.: Contact angles of DI water on sODCs (1st generation cell); the pristine sODC after reduction is marked as 0. Contact angles decrease slightly during switching cycle experiments.

potential increases more strongly for the O_2 mode, which needs oxygen access and has also been reported elsewhere [Jöri2011].

In the wide-ranging preliminary tests with the 1st generation cell, the sODCs were always inspected during the disassembly of the electrochemical cell. Figure 3.14 a) shows a pristine sODC just after the initial reduction. Therefore, sharp black edges are still visible. After a few switching cycles or particularly heavy stress, defects (Figure 3.14 b and d) or discoloration of elements of the electrochemical cell (Figure 3.14 c) could be observed. Examples of extreme stresses are thermal peaks, switching cycles with 11 M NaOH, or short-term dry-out.

Long-term consequences in the form of corrosion could magnify with electrolyte breakthrough, especially since stainless steel meandering flow fields were employed. At the same time, the gas breakthrough was rarely observed in the experiments as the presence of gas bubbles in the catholyte outlet hose. Gas breakthrough to the liquid side temporarily shielded the active surface of the sODC and led to short-term, reversible voltage increases.

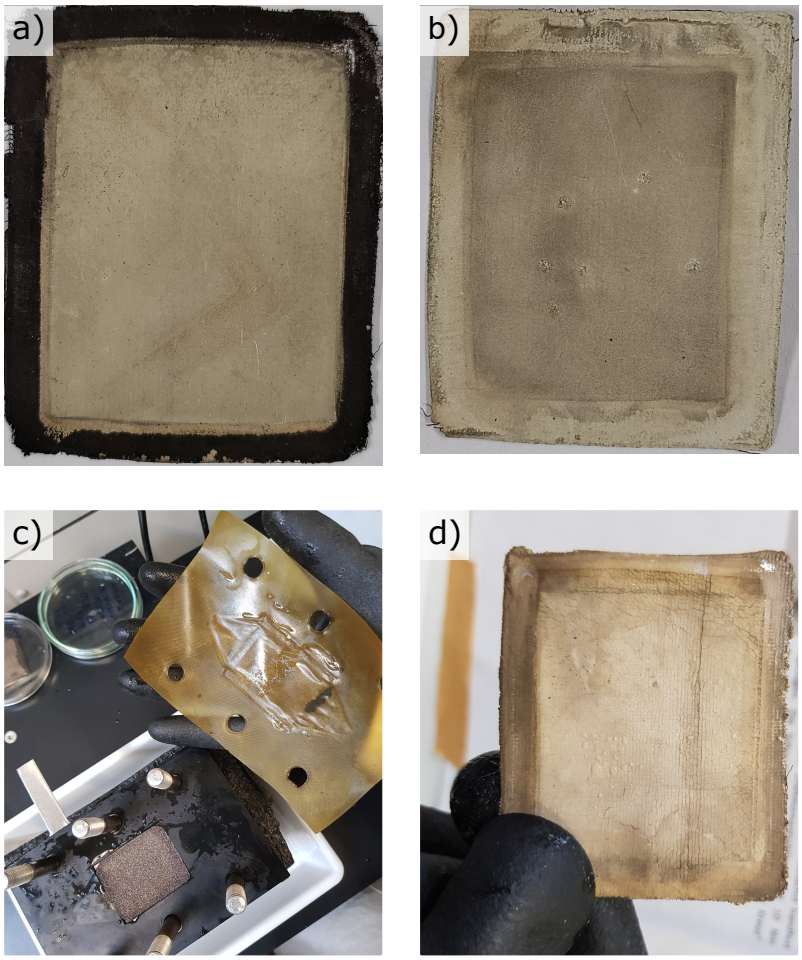

Figure 3.14.: Photographs of a) a pristine sODC after reduction, b) an sODC after 1,000 switching cycles, c) the electrochemical cell including a membrane after switching cycles with 11 M NaOH, and d) an sODC with visible cracks and defects (1st generation cell used).

However, no long-term increase in cell voltage could be attributed to a gas breakthrough.

Nevertheless, it could not be conclusively clarified whether the observed potential increase was related to electrolyte flooding, the degradation of the sODC, or other cell elements. Therefore, to exclude as many potential sources as possible, the 2nd generation cell without membrane, with chemically stable sealings, PTFE spacers, and flow fields, was designed.

2nd Generation Cell

Figure 3.15 shows the mean average of cell potentials for every 100 cycles and each reaction separately. Since two different cell designs were used (1st and 2nd generation cell), the cell potentials V were normalized to an initial value. The initial value V_0 was the average cell potential for the first ten switching cycles. The last ten of the 1,000 switching cycles were averaged for the overall trend and compared to the first ten averaged switching cycles, respectively. From the first run with the 1st generation cell, the first 1,000 out of 1,600 switching cycles were used for the comparison. The cell potential of the 1st generation cell strongly increased by 19.6 % between the initial and the final cell potential after 1,000 switching cycles in the H_2 mode and by 23 % in the O_2 mode (see crossed symbols in Figure 3.15). Running the 1,000 switching cycles with the 2nd generation cell showed a cell potential increases of 7.8 % and 5.1 % for the O_2 and H_2 mode, respectively (see empty symbols in Figure 3.15). While the cell potential fluctuated evenly around the initial value V_0 for the first 750 cycles, there was an apparent increase from the 750th cycle onward, again more pronounced in the O_2 mode than in the H_2 mode.

Figure 3.16.: NaOH droplet formation at the back of the sODC facing towards the gas side.

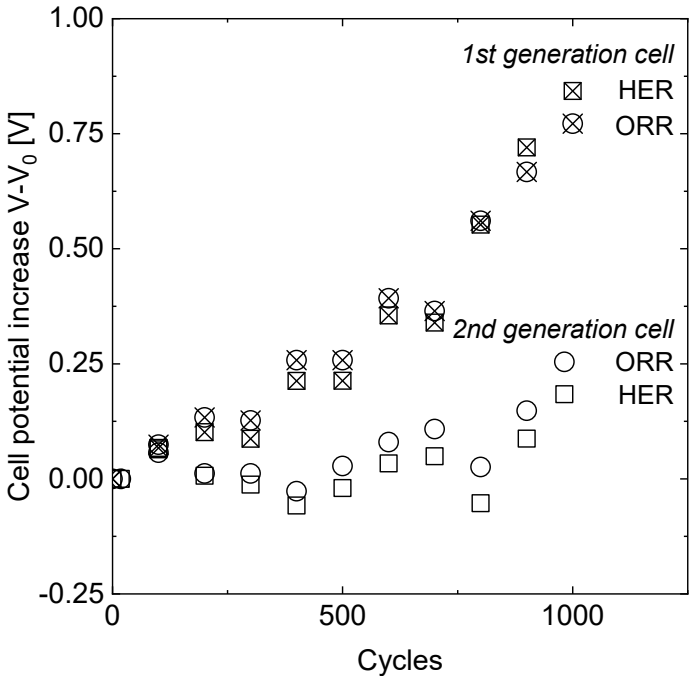

Figure 3.15.: Development of the cell potential with observation of leakage (crossed symbols) and without visible leakage (empty symbols) for 1,000 switching cycles at 670 mA cm^{-2}.

Even with numerous process-related and geometric adjustments, NaOH droplets still formed on the back of the sODC over time (see Figure 3.16), suspected of causing the potential increase. This assumption is discussed with observations from the literature in the following.

Kiros et al. [Kiro2006] observed stable cathode potentials for 300 h, despite shutdowns and start-ups during weekends, but reported an increase in cell temperature over time. However, after 302 h, NaOH droplets were detected in the emerging gas. A substantial cell potential increase was observed, probably caused by blockage of the gas pores due to precipitation in the electrolyte. Additionally, salt blockage from the NaCl electrolyte at the anode and pumping failure lead to small blisters on the ion exchange membrane. The present work confirms visible changes on the membrane in unexpected process irregularities, e.g., insufficient heat dissipation or pumping failure, using the 1st generation cell.

In a following study, Kiros et al. [Kiro2008] discovered a beneficial effect on long term-stability by increasing the PTFE amount and consequently decreasing the wettability of the ODC. They observed an increase in cathode overpotential with an increasing amount of PTFE (up to 20 wt % PTFE) attributed to increasing insulation of the current collector, especially at high current densities. A long-term experiment with and without 10 wt % PTFE over 1600 h showed that adding PTFE unraveled a 4-times lower decay rate of the cell potential for the PTFE-containing ODC compared to the standard ODC. This positive effect was attributed to the porous system's stable hydrophobic properties, avoiding electrode flooding and intrusion of the electrolyte to the gas side. In a 600 h experiment at 300 mA cm^{-2}, two 10 wt % PTFE-containing ODCs showed stable cell potentials varying between 1.98 V to 2.1 V, except for the second ODC drastically increasing cell potential after 300 h. This potential increase was explained by the formation of blisters at the ion exchange membrane (caused possibly due to the start-ups and shutdowns), uneven temperature and current distribution, and shielding effects of gas bubbles in the narrow anolyte gap. Their findings match the here reported observations after unexpected shutdowns and gas bubble entrapment in narrow electrolyte channels. However, although the PTFE content of a 2nd generation sODC had been increased, a positive effect could not be confirmed in the here reported results. Therefore, systematic adjustment of PTFE content while monitoring cell potential and flooding properties of sODC should be the focus of future studies.

Furuya et al. [Furu2000] conducted long-term experiments running over 1200 d with differently loaded ODCs. While the electrolysis started at relatively low cell potentials, the value for one of them increased by 350 mV after an unexpected interruption of the electrolysis on the 68th day. It was terminated on the 150th day. The cell potential value of a second ODC remained stable for 310 d. After an accidental interruption of oxygen supply, the cell potential increased by 850 mV and did not return to the initial value. This consequent switch to HER led to a high cell potential, which is why the process of the second ODC was terminated on the 394th day. A third ODC stayed at 2 V during the first 600 d but showed a subsequent total cell potential increase of 400 mV over more than 1200 d. They reported an increase in cell potential after switching the ODC into HER, which could have similar consequences for the here presented switching results. Their findings imply that an intermittent operation is especially detrimental to a stable three-phase boundary.

Despite stable cell potentials for 120 h (up to 550 h), Siracusano et al. [Sira2008] have shown that metal loss at the ODC surface, a decrease in hydrophobicity, and an increase in the precipitation of compounds from electrolytes may decrease ODC performance by occluding reaction pores. An increase in cell potential versus time is primarily attributed to the ORR (representing the rate-determining step of the overall process).

Wagner et al. [Wagn2004] observed a decrease in PTFE content and a similar long-term deterioration in the form of a cell potential increase of 100 mV over a total runtime of 5000 h (this study: 184 mV voltage loss in the H_2 mode, 254 mV voltage loss in the O_2 mode, 13 000 h runtime).

Vincent et al. [Vinc2017] observed a periodic variation of the cell potential due to the accumulation of bubbles attributed to low electrolyte flow rates (runtime 200 h)indicating the detrimental effect of .

In summary, cell potential increases were observed mainly after unexpected interruptions and electrolyte breakthroughs. The phenomenon of electrowetting has been frequently discussed in the GDE literature as a cause of electrolyte breakthrough [Paul2019; Paul2021; Kald2022; Bien2022]

(see chapter 2.2 for more information). Our observations of the gas side of the GDE showing droplet formation, coagulation, and droplet detachment agree with the findings by Paulisch et al. [Paul2019; Paul2021]. The authors investigated how electrolyte droplets covered the backside of ODCs, affecting the overall potential. They observed a faster droplet formation and accumulation at higher overpotentials (equivalent to higher current densities), which they explained by increased electrowetting. Also, the authors conducted stronger current density fluctuations at higher overpotentials, which might result from the different sizes of the emerging droplets.

In a following study, Paulisch et al. [Paul2021] investigated electrolyte distribution and filling of GDE pores. Operando synchrotron imaging confirmed the effect of electrowetting: Higher temporal fluctuations in electrolyte distribution with increasing overpotentials. Additionally, the authors found that pore flooding is irreversible.

Bienen et al. [Bien2022] investigated the electrolyte breakthrough in a GDE via a digital microscope. A higher overpotential facilitated the breakthrough of electrolytes to the GDE gas side. Faster droplet formation with higher overpotentials again indicated electrowetting. Surprisingly, a faster electrolyte breakthrough was observed for GDEs with a higher PTFE content. Both a higher PTFE content and lower overpotentials resulted in smaller electrolyte droplets and less droplet coverage at the GDE backside. The images showed that once a pore is filled with electrolyte, a droplet forms, and continuous electrolyte flow leads to droplet growth.

Franzen et al. [Fran2019] demonstrated that electrolyte filling in ODC pores is a key factor for efficient electrolysis. They have identified an optimal PTFE fraction that is low enough to enable pore filling and, at the same time, high enough to avoid pore flooding. Tafel slopes revealed that the catalytic performance was comparable for different PTFE fractions, and thus overpotentials were attributed to the physical three-phase formation. In addition to a low PTFE content, high overpressure also caused pore flooding, which had a detrimental effect on overpotentials.

Kalde, Grosseheide et al. [Kald2022] developed a microfluidic device with a porous, conductive structure, multi-scale porosity and heterogeneous

surface wettability to mimic conventional GDEs. They showed non-reversible wetting of microfluidic porous structures via in-operando visualization using confocal laser scanning microscopy. In addition, they visualized that the potential onset in gas-fed electrolyzers might disrupt the previously stable phase boundary.

While liquid management is well solved in the CAE cell, in less developed processes and new cell systems, fluid management may still be a problem. Other electrolysis studies, e.g., CO_2 electrolysis, have also reported a direct correlation between electrolyte breakthrough and cell potential increase or FE decrease [Jean2018]. Comparing the findings from the literature with the results of the present work confirms that there is a need for GDEs with low wettability to improve the long-term performance of gas-evolving electrolysis processes [Kiro2006]. Therefore, improvements in gas-electrolyte balances at GDEs and ODCs benefit various electrolysis processes and should be further explored.

3.4. Conclusion

Experiments have confirmed that conventional ODCs, which produce hydrogen as a side product at the cost of a high cell voltage, can be substituted by sODCs, consuming oxygen at a low cell voltage without affecting the anodic reaction. While switching from the H_2 to the O_2 mode reduces energy consumption by up to 25 % in CAE [Jöri2011], the results discussed here showed a decline of 45 % for the replacement system water electrolysis. Experiments showed a cell potential decrease of 1.24 V to 1.5 V for current densities between 50 mA cm^{-2} to 525 mA cm^{-2}.

In established operation of CAE industrial cells, the process runs stable over long periods of time. Therefore, mainly the interruptions due to switching cycles are attributed to cause the cell potential increase in the reported observations. This study presents for the first time that the sODC has been tested for a large number of switching cycles. Long-term evaluation of 1,000 switching cycles entailed a cell potential increase of up to 7.8 % and 5.1 % for the O_2 and H_2 modes, respectively. While the increase in the cathode

potentials with increasing current density was more pronounced in the H_2 mode than in the O_2 mode, this observation was reversed throughout 1,000 switching cycles. The 1,000 switching cycles with abrupt start-up and shut-down of the current had a detrimental effect on the three-phase boundary in the sODC pores, leading to electrolyte breakthrough and an increase in cell potential. Disruption of the three-phase boundary is particularly disadvantageous for the O_2 mode, where the formation of the three-phase equilibrium in the sODC pores is more significant.

This chapter shows the potential of sODCs for flexible electrolysis as a combination of demand-side management and mode switching. Further development of the sODC towards reduced electrode flooding is a prerequisite for a stable operation. However, studies have shown that the complex correlation between PTFE content, pore formation in GDE, and subsequent wetting in actual operation is not trivial to find [Fran2019]. Additionally, further work on the catalyst is needed to decrease cathode overpotentials. Another challenge, the flushing process between the two modes, is subject to the following Chapters 4 to 6.

4. Experimental and Simulative Investigations of Lab-cell Flushing Procedures

Parts of this chapter have been published as:
Kristina Baitalow, Niklas Köller, Paul Bacmeister, Robert Keller, Matthias Wessling
On the operation of switchable oxygen depolarized cathodes, Chemical Engineering Journal, 2023
DOI: 10.1016/j.cej.2023.143759

4.1. Introduction

The flexible CAE process with sODC involves the challenge that a fast and safe gas exchange is essential to enable a high level of flexibility. To address rapid flushing with inert gas between the two modes, this chapter maps the flow and concentration distribution of the flushing process in a lab cell via 3D-CFD simulations and shows a verification with experimental flushing times. Successful validation of the boundary conditions and assumptions of the CFD simulations provide a basis for following cell design optimization.

This chapter investigates the flushing process in a laboratory cell and maps the process in a 3D-CFD simulation. The measured flushing times are compared to the simulated ones for an oxygen-nitrogen system. CFD simulations are further adapted to meet the experimental observations. Successful verification of the boundary conditions and assumptions regarding the CFD simulations provide a basis for further cell design optimization. Finally, a procedure is proposed that saves experimental resources and enables optimization in a short time without geometric limitations regarding cell design.

4.2. Experimental

Cell design and setup were implemented according to Chapter 3.2. The 1st generation cell with 4 cm x 5 cm active electrode area was used. The cell contained a stainless steel meander compartment for the gas flow. The same cell elements were used (cathode: sODC provided by Covestro AG, Germany; anode: pure Nickel mesh Ni-2733 by Recemat BV, Dodevard NL; Anion exchange membrane: FUMASEP FAB-PK-130, Fumatech, Bietigheim-Bissingen, Germany). The sODC separated the catholyte from the gaseous reactants, which passed at the backside of the sODC through the metal meander. Either hydrogen evolved according to HER, oxygen (oxygen 3.5, ISO 14175-0-0, Westfalen AG, Münster GER) was supplied according to ORR, or nitrogen (nitrogen 5.0, ISO 14175-N1-N, Westfalen AG, Münster GER) was provided for the interim flushing step. The intermediate

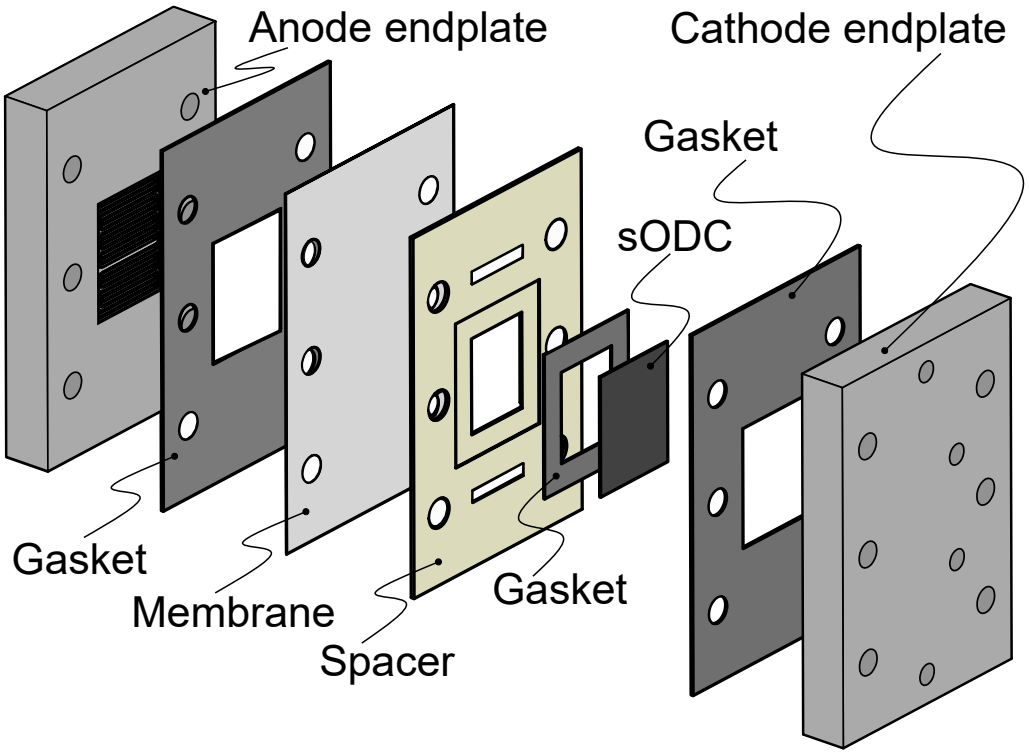

Figure 4.1.: Elements of the 1st generation electrochemical cell with meander-like compartments in cathode and anode endplates.

step with inert gas flushing was mandatory to prevent mixing into oxyhydrogen and is the focus of the following investigations. As the electrolyte, 1 mol NaOH was prepared with deionized water and sodium hydroxide platelets (CAS-No. 1310-73-2). The gases entered the cell through the cathode endplate directly into the meander inlay. The meander inlay was a serpentine flow channel with eleven turns. The width and depth of the serpentine channels were 2 mm. Figure 4.1 shows the elements of the electrochemical cell with anode and cathode endplates made of PTFE, gaskets for anolyte and catholyte streams, the membrane separating the electrolytes, a PTFE spacer to hold the sODC in place, and the two electrodes. Sealings made of ethylene propylene diene monomer (EPDM) rubber were left out in the sketch. The experimental setup and the equipment used are described in chapter 3.2. The same experimental parameters as in Table 3.1 are applied.

For the flushing experiments, oxygen sensors (FireStingO2 with OXB50-HS sensors, PyroScience GmbH, Aachen GER) were placed in tubes and

T-connectors directly before and after the cell. However, a total additional tubing length of 91 mm between the sensors and the flow channel in the cell could not be avoided. The oxygen sensors were bare fiber-optic sensors with a response time of less than 0.3 s for measurements in gases and liquids. Using two sensors allowed for measuring the exact residence time in the cell. All sensors were calibrated in the experimental setting prior to measurements. The gas supply was switched automatically from oxygen to nitrogen and back to oxygen at different volumetric flow rates via a direct-acting three-way pivoted armature valve (Type DS0330, Bürkert Fluid Control Systems, Ingelfingen GER). The measurements were performed without cell voltage applied to mimic the downtime during switching, but electrolytes were pumped at experimental flow rates and temperature. The oxygen content in the gas flow was recorded online. For evaluation, five measurements taken at the same conditions were mean-averaged.

Flushing times were obtained by measuring the oxygen content at the cell inlet and outlet from the point when the automatic three-way valve was switched to nitrogen (cell initially filled with oxygen) or oxygen (cell initially filled with nitrogen). There was 1100 mm tubing (inner diameter 4 mm) between the three-way valve and the cell. The transition from oxygen to nitrogen was not a sharp step function but a smooth transition due to the diffusive mixing in the tubing. Therefore, we recorded the flushing process starting with switching the three-way valve. This was included in the simulations using a fitting function.

4.3. Simulation

The simulation incorporated the gas compartment of the electrochemical lab cell and 7 cm of inlet and outlet tubing to ensure uniform gas inflow and outflow. 3D-CFD simulations were set up and solved in COMSOL Multiphysics 5.4. The 3D-CFD models verified experimental results, yielded a flushing time for safe operation and allowed for dead zone identification, especially when aiming to substitute meandering flow fields. The meander-like gas compartment of the 1st generation lab cell was implemented in

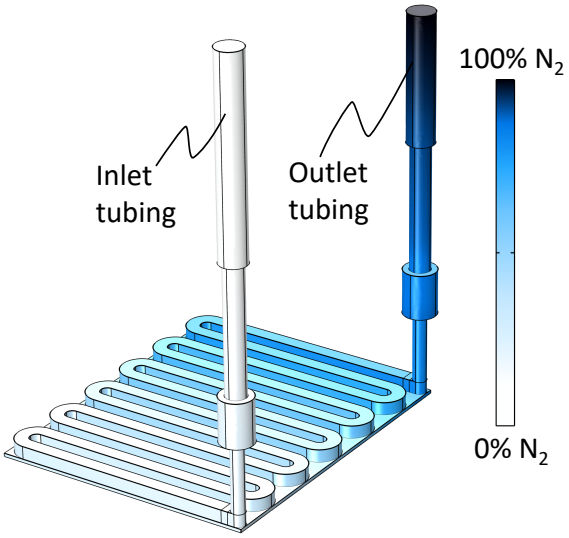

Figure 4.2.: Domain of the gas compartment, including tubing between the oxygen sensors and the cell, and the sODC modeled as porous material. Dark blue indicates nitrogen; white indicates oxygen.

the simulation model. The sODC and the 91 mm distance of the externally placed oxygen sensors were both included in the model (see Figure 4.2). The flushing time was determined based on the location where oxygen was last detected when purging with nitrogen and vice versa with oxygen operation. Figure 4.2 shows the displacement of a nitrogen-filled (dark blue) compartment with oxygen purging (white). The sODC was modeled as a cuboid of porous material with a thickness of 0.5 mm. Inside the porous sODC, mass transfer is governed by diffusion rather than convection. Variation of porosity ϵ and permeability κ of the porous material showed only minor influence on the flushing time. Therefore, ϵ and κ were kept constant.

Where possible, the mesh was implemented as swept mesh. The remaining domain was complemented with triangular elements, resulting in 1.73 million elements in total. Due to the low Reynolds number (Re = 3.86), the *Laminar Flow* physics module by COMSOL was used. The measured data of the inlet (see Figure 4.3) were fitted as a piece-wise function in Matlab R2017a and used as input for the CFD simulations in COMSOL. After the initial time delay of the incoming gas due to tubing, the piecewise function is applied at the cell inlet, describing the oxygen mass fraction. The *steady first deviation* option is used to smooth the transition between the two intervals.

The oxygen mass fraction of the entering gas streams is set to 0 in the case of nitrogen flushing or 1 in the case of oxygen filling, respectively. Other boundary conditions were assigned according to Table 4.1. The mixing of the species was realized with the *Transport of Concentrated Species* interface by COMSOL. It features the convective species transport as well as the diffusive transport. The two physics interfaces were coupled with the *Flow Coupling* connection and solved simultaneously in all simulations. The tubing between the cell and the three-way valve was mimicked via a continuous function at the inlet of the cell. The continuous function was fitted to the experimental data of the oxygen sensor at the inlet of the cell.

Table 4.1.: Simulation parameters for the lab-cell CFD studies.

Simulation	**Value**
Inlet velocity	$0.0663\,\mathrm{m\,s^{-1}}$
Outlet pressure	1 atm
Temperature	35 °C
Porosity [-]	0.4
Permeability [m^2]	10^{-12}

4.4. Results and Discussion

4.4.1. Experimental Results

Figure 4.3 shows measurement data of the inlet (black) and the outlet (gray) oxygen mass fraction at a nitrogen volume flow rate of $50\,\mathrm{mL\,min^{-1}}$. Nitrogen flushing means a decreasing oxygen content in an initially oxygen-filled cell (squares in Figure 4.3). Oxygen filling occurs after the hydrogen reaction and a flushing step (circles in Figure 4.3). Flushing and filling times were acquired between the three-way valve and the cell outlet. According to explosion limits of oxyhydrogen [Schr2002], the flushing time was reached when the oxygen mass fraction was $< 5.4\,\mathrm{w\%}$ and the filling time when the

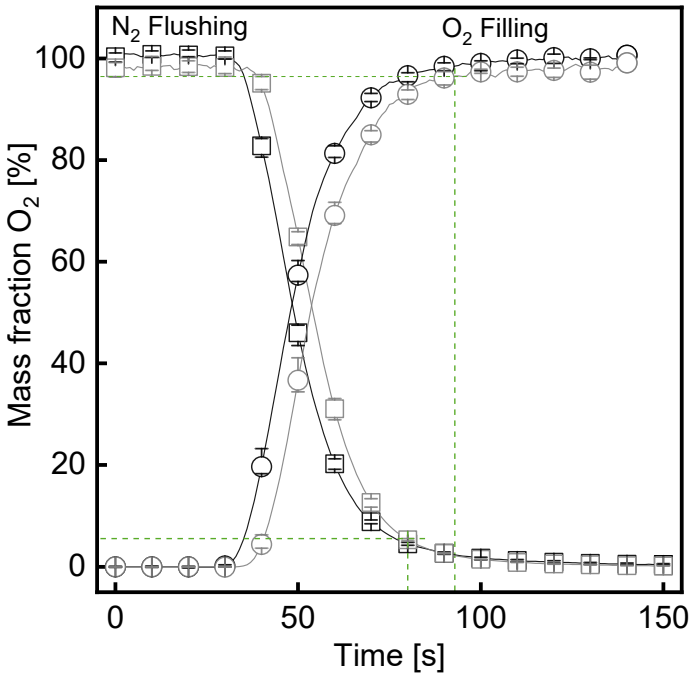

Figure 4.3.: Simulations (lines) and experiments (N_2 flushing - squares, O_2 filling - circles) show similar results, both for the inlet (black) and outlet (gray) domains, at a volume flow rate of 50 mL min^{-1}. Dashed green lines mark the flushing and filling time.

oxygen mass fraction was $>$ 96.5 w%. All reported results are the mean average of five measurements.

For the nitrogen flushing, it takes 32 s (40 % of the entire flushing time) until the mass fraction at the inlet begins to change. It takes another 6 s until the mass fraction at the outlet starts to decrease. The total time of the nitrogen flushing step can be determined to be 80 s (see marked green lines in Figure 4.3). After exceeding an oxygen mass fraction of 96.5 % at the cell outlet, the filling time is determined to be 93 s. The longer flushing time of nitrogen demonstrates the influence of different densities: the heavier oxygen (1.31 kg m^{-3}) takes longer to displace the lighter nitrogen (1.15 kg m^{-3}) (density values at room temperature and ambient pressure [Vere2013]).

The measurements show the influence of the peripheral tubing on the flushing time. The tubing between the three-way valve and cell favors the initial delay of gas entering the cell and leads to a wide transitional concentration area. The tubing (13.823 mm^3) exceeds the meander volume

(1.834 mm^3) by a factor of 7.5. Laminar flow with only minor radial exchange develops due to the long tubular geometry. Therefore, placing the gas supply close to the electrolysis cell is highly important.

4.4.2. Simulative Results

The measured data of the inlet (see Figure 4.3) is fitted as a piece-wise function and used as input for the CFD simulations. After the initial time delay of the incoming gas due to tubing, the piece-wise function is applied at the cell inlet, describing the oxygen mass fraction. The *steady first deviation* option is used to smooth the transition between the two intervals. The entering gas streams is set either to $w_{N2,in}$ in the case of nitrogen flushing or to $w_{O2,in}$ in the case of oxygen filling, respectively.

Determining the flushing time for the laboratory experiments poses a trade-off between the shortest possible flushing time (less waste gas, time savings for the switching cycles) and safe flushing (no residues). However, a closer examination of the simulations showed that no dead zones form in the gas compartment, and gas exchange takes place reliably. Therefore, a sufficiently safe flushing time of 45s was chosen as a compromise, which could be used for comparability in both cell designs.

Figure 4.3 shows the simulated oxygen mass fractions plotted as lines for the inlet (black) and the outlet (gray) over time. Here, the inlet line is the input for the simulation, and the outlet line is the result of the simulated exiting gas. The respective times for the nitrogen flushing reaching the 5.4 % limit were determined to compare simulations and experiments. Figure 4.4 shows the comparison of measured (squares) and simulated (circles) flushing times for different flow rates (50, 75, and 100 mL min^{-1}). The flushing time in the reported experiments was 45 s, whereas the simulations suggest 57 s. Thus, residual oxygen and hydrogen remained in the gas compartment. This effect can be seen in Figure 3.5, where the cell potential in the hydrogen mode originates at the value of the ORR cell potential and increases when all oxygen is consumed and vice versa. In future studies in large equipment, safe flushing times must be established in order to provide non-explosive

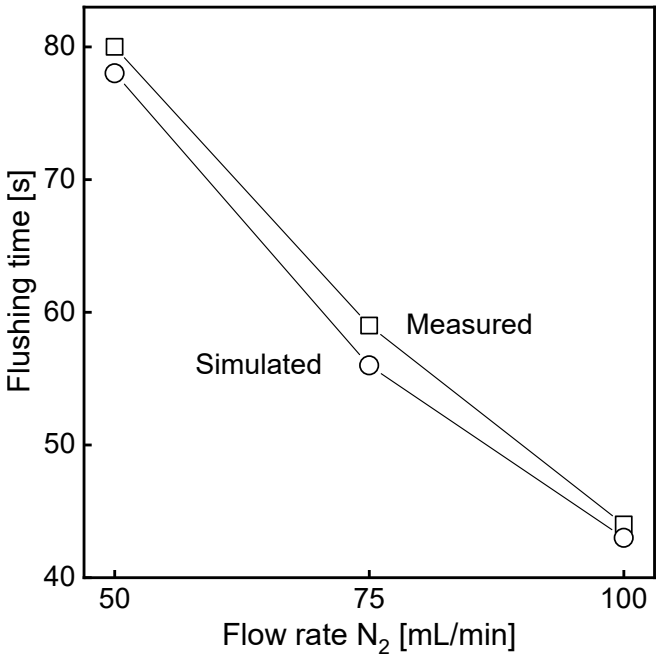

Figure 4.4.: Flushing times obtained from experiments (squares) and simulations (circles) for different flow rates.

atmospheres.

4.5. Conclusion

After the reproducibility of switching between the two modes was demonstrated experimentally in Chapter 3, the flushing process between the modes has been further analyzed in experiments and simulations in this chapter. The flushing time is crucial to the viability and potential profitability of the process because it means downtime in chlorine production and requires a chlorine reservoir.

Here, the two processes were investigated experimentally with measurements via oxygen sensors at the laboratory cell inlet and outlet. The nitrogen flushing step after and the oxygen filling before the oxygen mode was demonstrated. A significant influence of the peripheral tubing on the flushing time was shown, which can be deduced similarly at the industry size. While the gas supply from the valve to the cell is about 40 % of the total flushing

time in the lab-scale experiments, direct placement of the gas supply just before the cell could reduce the flushing time. For switching from oxygen to nitrogen, the flushing time was reduced from 80 s to 6 s at 550 mL min^{-1} when considering only the concentration change between the inlet and outlet. Furthermore, a model for CFD simulations of the laboratory cell was developed. The flushing process was fully computationally described. Flushing times calculated with the simulation model agreed well with measured flushing times at 2-5% deviations. The lab-scale experiments have verified the simulations' physical models and boundary conditions. They can now be used for further applications, such as optimizing large-scale electrolysis cells. While the laboratory cell has a well-flushable, meander-like cell design, the current ordinary design of electrolysis cells is down-target due to numerous and highly deflecting internals impeding rapid gas exchange and, thus, a low-cost flushing process.

The model of the laboratory cell can be used to investigate the influence of other operational parameters (volume flow rate, temperature, overpressure at the outlet, sODC porosity and permeability). The verified simulation approach can thus be used to upscale and optimize the cell design in the next step.

5. Simulative Investigation of Gas Flow in an Industry Cell

5.1. Introduction

Industrial electrolysis processes typically run a fixed reaction or even in a single operating point or range. Therefore, introducing additional flexibilities in electrolysis processes with changing gases is new territory for cell manufacturers and electrolyzer operators. The following chapter addresses the flow behavior during the flushing step and its consequences on the switching between H2 and O2 modes. The intuitive choice is nitrogen as the inert purge gas for a safe change from H_2 to O_2 mode (and vice versa) in the flexible CAE discussed here. Chapter 4 showed that the periphery around the electrochemical cell has an impact on the flushing process. The modeling of the lab-scale cell in a 3D CFD model to simulate the flushing between the two modes and experimental verification of the simulated concentration profiles is the basis for the following section.

In this chapter, the CFD model is extended to a commercial industry-scale cell. The model is then used for simulative investigations of the flow profile and concentration distribution of an oxygen-filled gas compartment which is flushed with nitrogen. The gas compartment contains internals. These grant structural stability for the entire cell, in general, and the porous switchable oxygen depolarized cathode (sODC), in particular. The internals influence the flow inside the cell and, thereby, the gaseous concentration distribution. The following chapters investigate to what extent the cell internals influence the flushing time. CFD simulations investigate critical dead zones in the current design of the internals. 2D models visualize the convective flow through the gas compartment and the diffusive gas exchange with the sODC. Finally, the flushing time for the gas exchange from oxygen to nitrogen is estimated.

5.2. CFD Simulations

In flexible CAE, switching occurs between the energy-saving O_2 mode (oxygen reduction reaction, ORR) and the energy-intensive H_2 mode (hydrogen evolution reaction, HER). Figure 5.1 shows the switching procedure of the

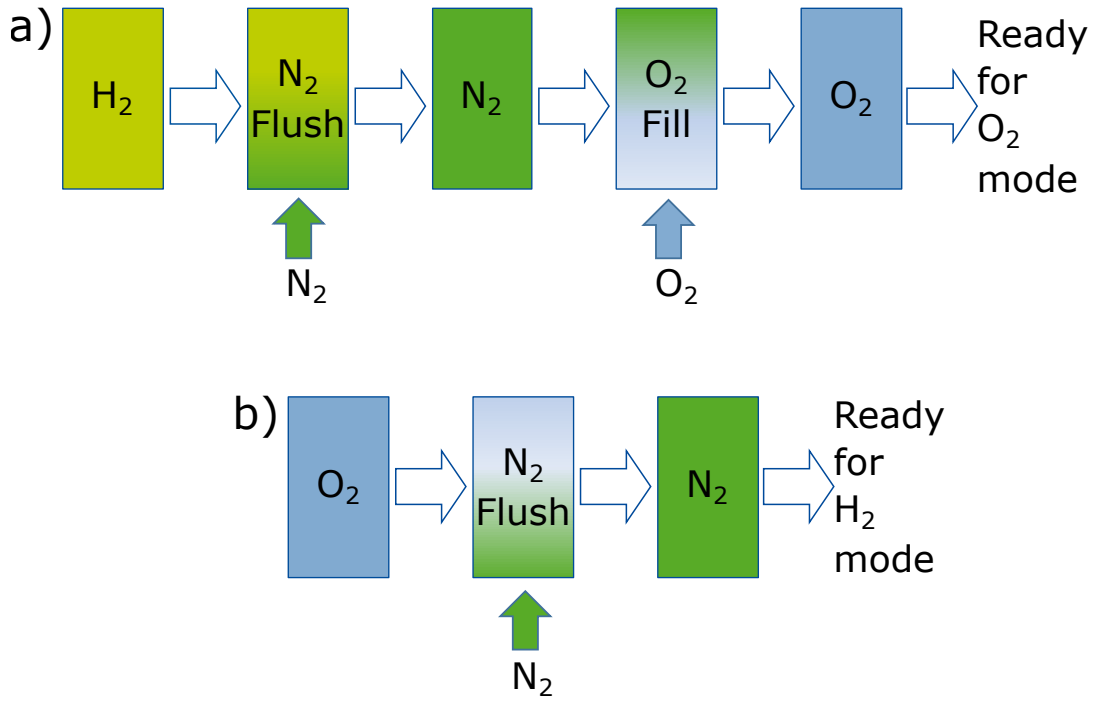

Figure 5.1.: Concept of mode switching in the gas compartment of a CAE cell a) from H_2 mode to O_2 mode with nitrogen flushing and oxygen filling, and b) from O_2 mode to H_2 mode with nitrogen flushing only.

flexible CAE. During the switching process, electrical current is turned off, and thus, no chlorine production takes place. If the cell is in H_2 mode, the hydrogen-filled gas compartment is first flushed with nitrogen and then filled with oxygen to prevent any initiation of the competing hydrogen evolution reaction (HER, see Figure 5.1 b). On the other hand, if the cell operates in O_2 mode, the oxygen-filled gas compartment is flushed entirely with nitrogen before the hydrogen mode starts (see Figure 5.1 b). Both experiments and simulations use 4 % and 96 % oxygen content as lower and upper explosion limits, respectively [Schr2004a]. For the switching, it should be noted for operation-relevant costs that the shutdown and start-up of the electrolysis must be gradual and therefore require a certain amount of time. However, the electrolysis start-up and shutdown are not considered here.

5.2.1. Simulation Domain

The simulation domain is computationally challenging due to the physical dimensions of commercial industry-scale cells. Since large-scale electrolysis processes use planar cells, which are stacked in series, the cells usually exhibit a cell thickness (H) of only a few millimeters [Mous2008; Moor2000]. In contrast, the width (W) and length (L) of the cells usually measure several meters to generate a large usable electrode area. Here, a commercial CAE cell with an exemplary area of $WxL = 2.7\,\mathrm{m}^2$ is examined [Mous2008].

Due to the large geometry relative to the velocity and concentration gradients, 3D simulations of the entire cell may not be feasible in all cases. To be able to simulate the flow phenomena in the cell anyway, simplified simulations in 2D are performed. This allows to make meaningful statements about the flushing process, while, at the same time, maintaining a reasonable computational effort. Figure 5.2 shows the top view of a simple rectangular planar cell (*1st section view*). The right part of Figure 5.2 shows the projection with inlet, outlet and internals. Internals are required to stabilize the porous sODC and are usually simple shapes to reduce manufacturing effort. The internals are bars arranged equidistantly over the whole area, forming vertical flow channels. The bars reach from bottom to top with small cutouts at their ends to enable flow along the outer walls of the gas compartment. Flow simulation in this domain enables the evaluation of the gas flow inside the gas compartment.

The inlet pipe is located at the lower right, and the outlet pipe is on the upper left. The inlet pipe requires special attention: it is very thin and demands higher mesh resolution than the rest of the compartment. Additionally, the combination of small pipe diameter, high velocity and sudden expansion inside the gas compartment causes diffuser-like effects and can initiate turbulence at the inlet opening. In the original cell, the inlet is a small pipe inside a wider channel. Therefore, gas flow around the inlet pipe is possible. In the *1st section view*, this is modeled by placing the inlet pipe 5 cm away from the lower cell wall and 2 cm away from the right cell wall.

The *2nd section view* is parallel to the channel length and perpendicular to the sODC ($L = 0$, see Figure 5.3). In this view, the sODC was modeled

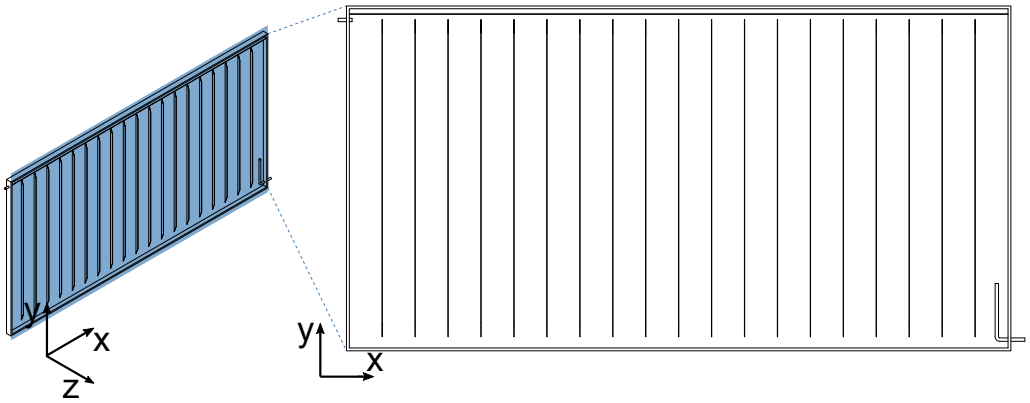

Figure 5.2.: 2D simulation domain of a section view parallel to the sODC.

as a porous domain (see Chapter 5.2.2 for further details) to examine its influence on the flow through the channels.

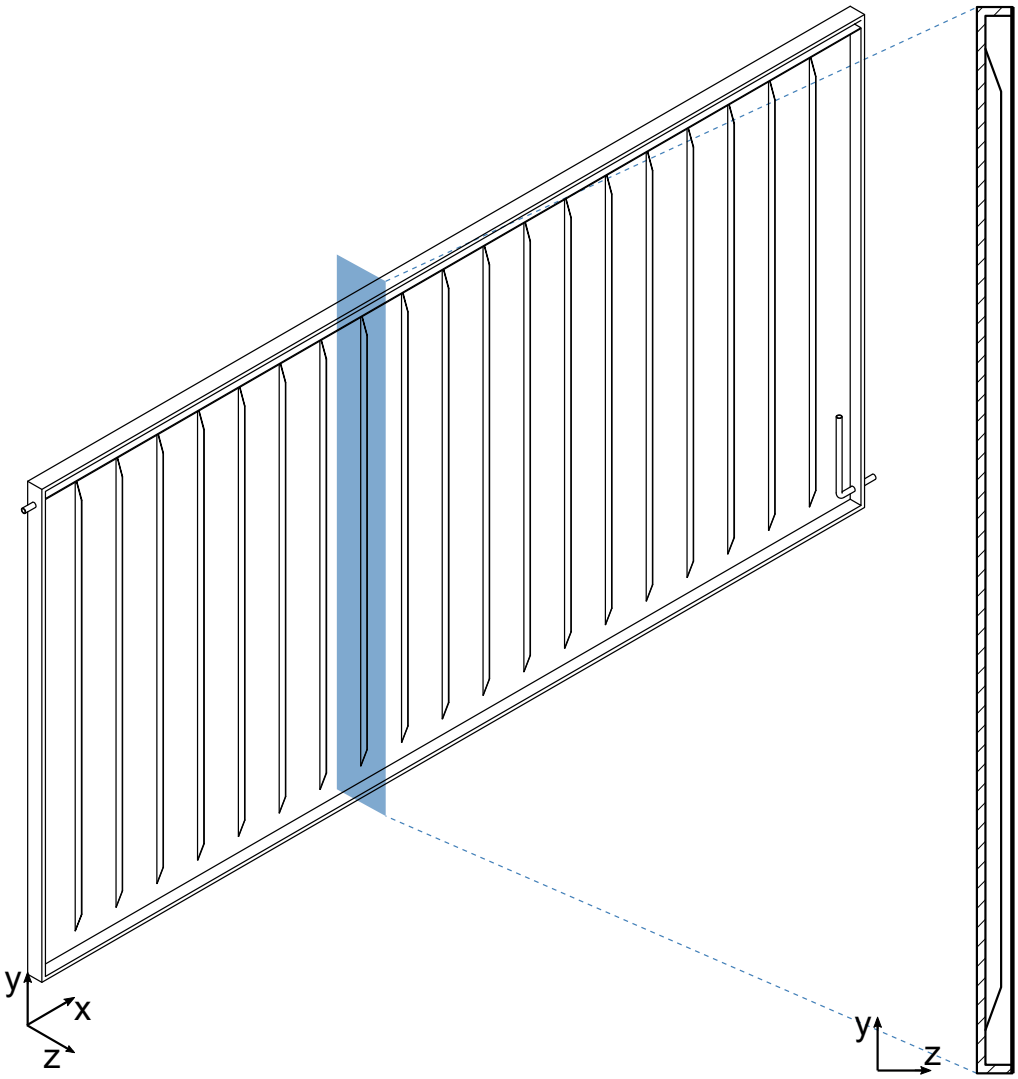

Figure 5.3.: 2D simulation domain of a section view perpendicular to the sODC.

5.2.2. Boundary Conditions and Assumptions

The appropriate physical model selection depends on the prevailing flow regime, i.e., laminar or turbulent flow. As discussed in Chapter 2.3.2, various flow models are available. Implementation of laminar physics requires the solution of the complete Navier-Stokes equations and thus results in high computational cost. The computational effort can be reduced by using turbulence models to smooth velocity fluctuations resulting from turbulence. The κ-ϵ turbulence model solves the Reynolds-averaged Navier-Stokes equations (RANS) using empirical equations for the turbulent kinetic energy and the turbulent dissipation rate (see Chapter 2.3.2). In the discussed

domain, the volume flow enters at a high velocity through the inlet and distributes rapidly in the large interior of the gas compartment. For an inlet velocity of $u_{in} = 5.24\,\mathrm{m\,s^{-1}}$ and a hydraulic diameter of $d_{hyd} = (0.01\,m \cdot 0.03\,m)/2 \cdot (0.01\,m + 0.03\,m) = 0.015\,m$, the Reynolds number can be calculated to $Re = 5180$ ($\eta_{N2} = 1.76 \times 10^{-5}\,\mathrm{Pa\,s}$ and $\rho_{N2} = 1.16\,\mathrm{kg\,m^{-3}}$ at room temperature and 1.2 bar). However, since limits for Reynolds numbers are tabulated only for simple geometries, the transition from laminar to turbulent flow cannot be estimated from the Reynolds number in the complex domain. Therefore, both the laminar and turbulent interfaces are tested in the flow domain here.

To calculate the velocity field in the 2nd section view, the *Laminar Flow* interface is chosen (plane perpendicular to the sODC, see Figure 5.3).

The CFD model is implemented in COMSOL Multiphysics 5.4. The flow physics *Laminar Flow* was tested and *Turbulent Flow,* $\kappa - \epsilon$ (**spf**) was chosen for the main part of the simulations. The flow is considered stationary in the **spf** interface. To model mass transfer, the flow interface is coupled with *Transport of concentrated species* (**tcs**) via *Flow Coupling* (**rf**). Determining the gas exchange and, thus, the flushing time is a time-varying process. Therefore, the **tcs** interface is considered time-varying. Diffusion is modeled according to Fick´s law in the **tcs** interface. The calculation of **spf** and **tcs** can be split into successive steps: First, a stationary velocity field is calculated within the **spf** interface. Afterward, the **rf** interface transfers the pressure and velocity field calculated in the **spf** interface to the **tcs** interface. Finally, the **tcs** interface calculates the time-variant concentration distribution using the stationary velocity field for convective transport. The successive simulation approach is depicted in Figure 5.4.

In the **spf** interface, the fluid flow is governed by the laws of mass, momentum and energy conservation (see Chapter 2). In addition, the flow is modeled as incompressible. The Mach number is calculated with the maximum velocity detected in the gas compartment ($u_{max} = 8\,\mathrm{m\,s^{-1}}$) and the speed of sound in oxygen ($c = 326\,\mathrm{m\,s^{-1}}$). Under these conditions, the Mach number results in 0.0246. Therefore, compressibility is set to *Compressible Flow (Ma¡0.3)*. The inlet velocity is chosen according to volume flows comparable to industrial values. Calculation of the inlet velocity differs

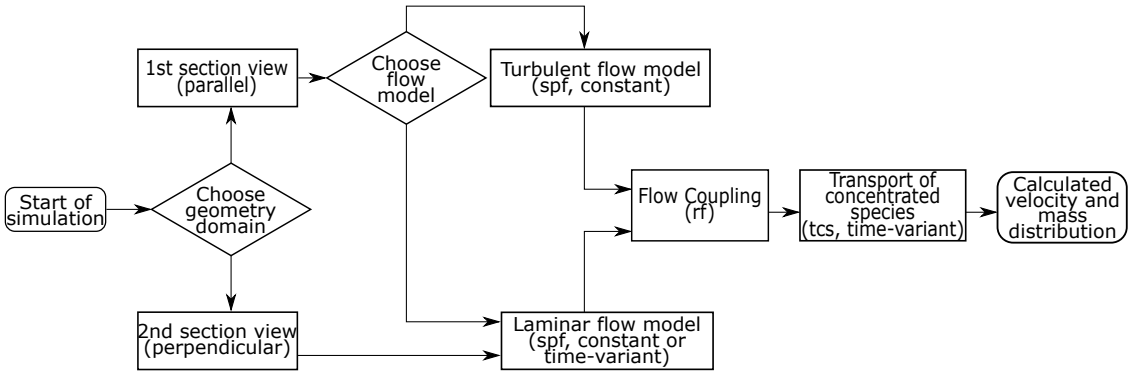

Figure 5.4.: Successive simulation method.

between 2D and 3D geometries. Depending on the geometry, the effective inlet area varies. For the 3D simulation, the effective area is equivalent to a circle. However, a 2D simulation considers the simplification of identical simulation domains in the z-axis (equal flow field above and below the simulation layer). Thus, the inflow is modeled via a virtual line, and the inlet velocity is calculated for a rectangular inlet in 2D. The initial condition of the velocity in the domain is set to 0. However, the sharp increase in the entering inflow can impede convergence. Thus, the inlet velocity is ramped up gradually to facilitate convergence. Therefore, the variable of the inlet velocity is multiplied by a two-times differentiable step function. The step function ramps the inlet velocity from 0 to the defined velocity value within the first 0.1 s. In the **tcs** interface, the initial condition for the nitrogen mass fraction throughout the cell is set to 0; the inlet mass fraction is set to 1. Again, to facilitate convergence, the incoming concentration of the inflow is multiplied by the step function, increasing the inflow concentration from 0 to the defined inflow value.

The outlet condition is set to an overpressure of 220 mbar. The *no slip condition* is applied at the walls. For the porous sODC domain, a porosity of 40 % [Bula2017], and a hydraulic permeability for gas of $1\times10^{-12}\,m^2$, comparable to fuel cells [Grou2019], are assumed. Boundary conditions of the CFD simulations are summarized in Table 5.1.

The gas density is kept the same for all gases in this section and the geometry optimization in Chapter 7. Therefore, the N_2-O_2 material system

is implemented with the material properties for nitrogen.

For the stationary velocity-field calculation, the algebraic multigrid solver GMRES is applied, while the calculation of time-dependent physics is accomplished with the direct solver PARDISO.

Table 5.1.: Simulation conditions for CFD simulations (density values at room temperature and ambient pressure [Vere2013]).

Parameter	**Value**
Inlet velocity	$0.44\,\mathrm{m\,s^{-1}}$
Pressure	220 mbarg
Temperature	70 °C
Diffusion coefficient	$7.81\times10^{-5}\,\mathrm{m^2\,s^{-1}}$
$\mathrm{Porosity_{sODC}}$	0.4
$\mathrm{Permeability_{sODC,\,gas}}$	$1\times10^{-12}\,\mathrm{m^2}$

5.2.3. Implementation of Different Density Properties

In addition, it was investigated to which extent different gas densities affect the concentration distribution. For this purpose, individual material properties for nitrogen and oxygen have been added. The properties molar mass and diffusion coefficient were defined species-specific in the tcs interface. spf receives the resulting mixture density and dynamic viscosity from tcs and the material node, respectively. The mixture density is determined by employing the ideal gas law.

Furthermore, gravity was integrated as an additional external force in the spf interface. In addition, the concentration development affects the flow due to the varying densities in the gas mixture. Therefore, the Flow Coupling interface rf solves spf and tcs simultaneously.

5.2.4. Meshing

A suitable mesh is essential for the simulation to replicate reality as accurately as possible. In general, a higher number of elements (NoE) in a mesh leads to higher accuracy of the model but can encourage the undesired prolonging of simulation time. Therefore, an appropriate mesh can reproduce reality with as little discrepancy as possible in an acceptable computing time. There are structured and unstructured meshes. Structured meshes consist of consistent, quadrilateral elements. Their advantages are a proper numerical transition and little memory usage. Unstructured Meshes consist of triangular or quadrilateral elements in 2D. They can be adapted to complex geometries more easily. [Ande2012]

COMSOL provides an automatically generated mesh that depends on the physics used ('physics-controlled'). The resolution of the physics-controlled meshes varies between 'extremely coarse' to 'extremely fine'. A refinement at the walls, the 'boundary layers', add refinement for edges and walls. In this thesis, physics-controlled meshes are used initially, which are further adapted in specific regions if necessary.

Low mesh quality can be caused by an insufficient NoE or inappropriately chosen mesh element geometries. Complex geometry may have areas that are difficult to mesh, such as tapered elements, thin regions or edges, a high degree of detail or a large aspect ratio. To ensure that the simulation result does not depend on the mesh, a mesh independence study is performed. Thereby, a parameter, e.g., the domain-averaged velocity or pressure, is observed while the NoE is slowly increased. If the observed parameter does not fluctuate by a certain anymore, mesh independence is achieved. Due to the complex geometry, accurate meshing is challenging in the case of the CAE cell. Therefore, meshing is discussed in detail in the results section 5.3.

5.2.5. Analysis

Velocity and concentration distribution were analyzed in the whole domain. In addition, user-defined probes were selected in the inlet and outlet. Data

was recorded at 1 s intervals and exported for analysis with Matlab. For evaluation of the concentration course, the minimal nitrogen mass fraction was plotted over time. In addition, concentrations were averaged over the whole domain or for the user-defined probes.

The simulations aim to calculate the required time to reduce the oxygen concentration in the domain below explosion limits of oxyhydrogen (see Chapter 4.4.1). When the nitrogen mass fraction exceeds 95 %, the gas compartment can be considered completely flushed. The time required to reach this limit at every point in the cell is called 'flushing time'. To calculate the flushing time, the minimal nitrogen mass fraction was evaluated.

5.3. Results and Discussion

This section first evaluates the physics selection and influence of mesh accuracy. A detailed mesh independence study focuses on different degrees of fineness and their effect on the velocity distribution. Finally, it is discussed to what extent different gas densities and a second outlet influence the gas exchange.

5.3.1. Effects of Mesh and Physics Choice on Simulation Results

The simulation domain has large aspect ratios (small depth vs. large area), which makes accurate meshing challenging. Moreover, the inner walls of the numerous internals need a high degree of refinement. The complex geometry of the gas compartment and different orders of magnitude demand locally refined regions, particularly the inlet, the outlet and the sODC domain. Therefore, a mesh independence study based on the domain-averaged velocity as a function of the NoE was performed to decide on a suitable mesh. In addition, the refinement *Boundary Layers* was applied at the walls.

First, the *Laminar Flow* interface was implemented for different NoE to analyze the evolution of the flow with increasing mesh refinement. Therefore, several levels of the physics-defined mesh were implemented, ranging

between 'extremely coarse' and 'extremely fine'. This step aimed to reveal any peculiar irregularities.

Figure 5.5 shows the flow evolution of the first 5 s using *Laminar Flow* with a 'finer' mesh. Figures 5.5 a)-e) show the velocity distribution in a color map ranging from low velocities (black), medium values (blue) to velocities up to $v = 7\,\mathrm{m\,s^{-1}}$ (white). The left side contains red arrows to visualize local velocity directions. On the right side of Figure 5.5, white arrows indicate a main flow along the cell frame and a vertical sub-flow through the channels. After 1 s, a significant gas volume flow moves downwards in the fourth and fifth channels from the right, indicated by higher velocity in that region (lighter color). At the bottom of the cell, the flow splits into a right and a left part. This flow-splitting point moves to the left during the simulation: After 2 s, the flow splits at the bottom of channels ten and eleven. After 5 s, the splitting zone cannot be identified anymore, and most of the gas moves to the right. Figure 5.5 a)-e) can be characterized as the stabilization of the flow field.

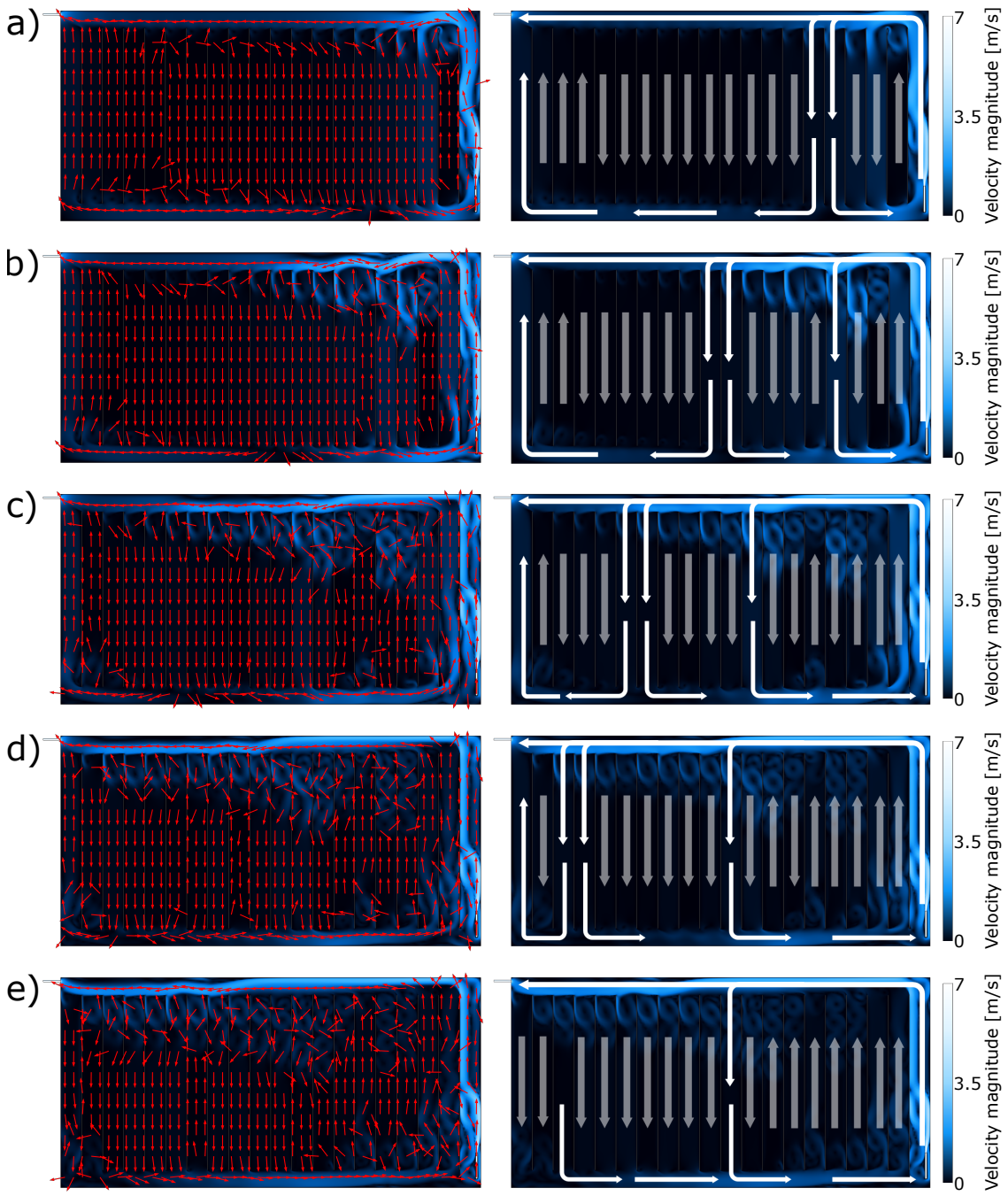

Figure 5.5.: Velocity distribution after a) 1 s to e) 5 s of a laminar, time-variant flow simulation with a 'finer' mesh and constant gas density. Arrows indicate the local flow direction (red, on the left) and the main flow direction (white, on the right).

In the following, the averaged velocity was evaluated for increasing NoE ('coarse' to 'extra fine') within the initial 60 s using a time-variant *Laminar Flow* interface (see Figure 5.6). The average velocity increases within the first seconds to values of about 0.2 m s^{-1} to 0.3 m s^{-1}. The initial increase is due to the ramping of the inlet velocity and the gradual distribution of the flow field through the gas compartment. For NoE smaller than 100,000, the averaged velocities stabilize after the first 20 s (see 'coarse' to 'finer' meshes in Figure 5.6). However, for very fine meshes with NoE of more than 100,000, the averaged velocity fluctuates within ± 15 % and does not stabilize within the first 60 s (see exemplary 'extra fine' mesh in Figure 5.6). In these very fine meshes, the smaller mesh elements resolve the flow phenomena in more detail and can lead to oscillations in the velocity calculation using *Laminar Flow*.

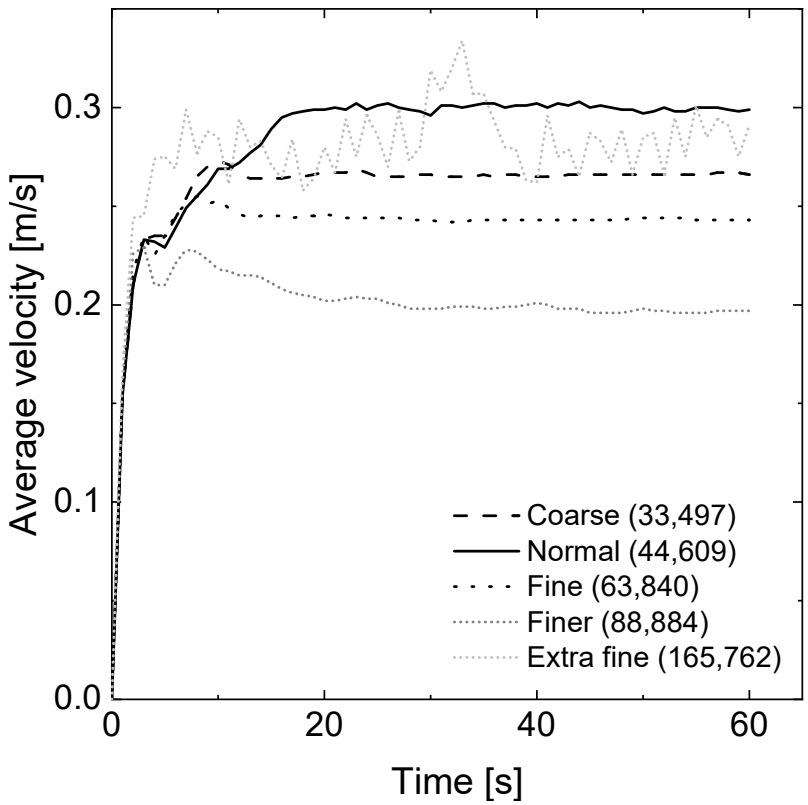

Figure 5.6.: Average velocity in 2D geometry parallel to sODC (1st section view) with NoE given in brackets.

The high degree of detail can be seen in Figure 5.7, showing a very

coarse (22,155 NoE, Figure 5.7 a) and a very fine mesh (182,930 NoE, Figure 5.7 b). The coarse mesh has a homogeneous flow field and a main flow running circularly along the outer walls. The velocity between the bars in the center of the cell is almost zero. In the fine mesh, the flow field shows a similar main frame flow, but several circular instabilities and small vortices appear. Vortices can also be found between the bars in the center of the cell and appear at different places throughout the simulation. The numerous vortices show a volatile velocity field over time in Figure 5.7 b). The solver of the *Laminar Flow* interface attempts to fully solve the Navier-Stokes equations and the flow effects very accurately. Finer mesh and, hence, a larger NoE resolves the instabilities of the flow in more detail. Vortices form due to the orthogonal arrangement of the bars. In addition, the high inlet velocity can induce flow instabilities. The vortices are not stationary but change their shape and location during the simulation. It cannot be eliminated whether the instabilities in the flow field originate from poorly conditioned mesh elements or if they occur in reality.

Based on the results of the *Laminar Flow* interface, a mesh independence study was performed with the κ-ϵ model. Figure 5.8 shows the domain-averaged velocity as a function of NoE. A trend line indicates an asymptotic course of the average velocity, approaching a mean value of about 0.0574 m s^{-1} starting from an NoE of $4.35x10^{10}$. Considering the fluctuations of the data points, the mesh settings were selected, matching the NoE of $5.81x10^{5}$.

The mesh should also be suitable for mass transfer simulations. Hence, the influence of the NoE on mass distribution was investigated. Figure 5.9 exhibits the average mass fraction of nitrogen after a flushing time of 10 s. Again, a trend line indicates an asymptotic course of the mass fraction over NoE. As for the velocity field, the mesh with $5.81x10^{5}$ NoE elements were selected as sufficient refinement.

Based on these preliminary simulations, the *Turbulent* κ-ϵ model was chosen to perform further simulations as a compromise for stable convergence within acceptable simulation time. However, it still needs to be clarified whether the vortices demonstrated in the *Laminar Flow* simulations exist in

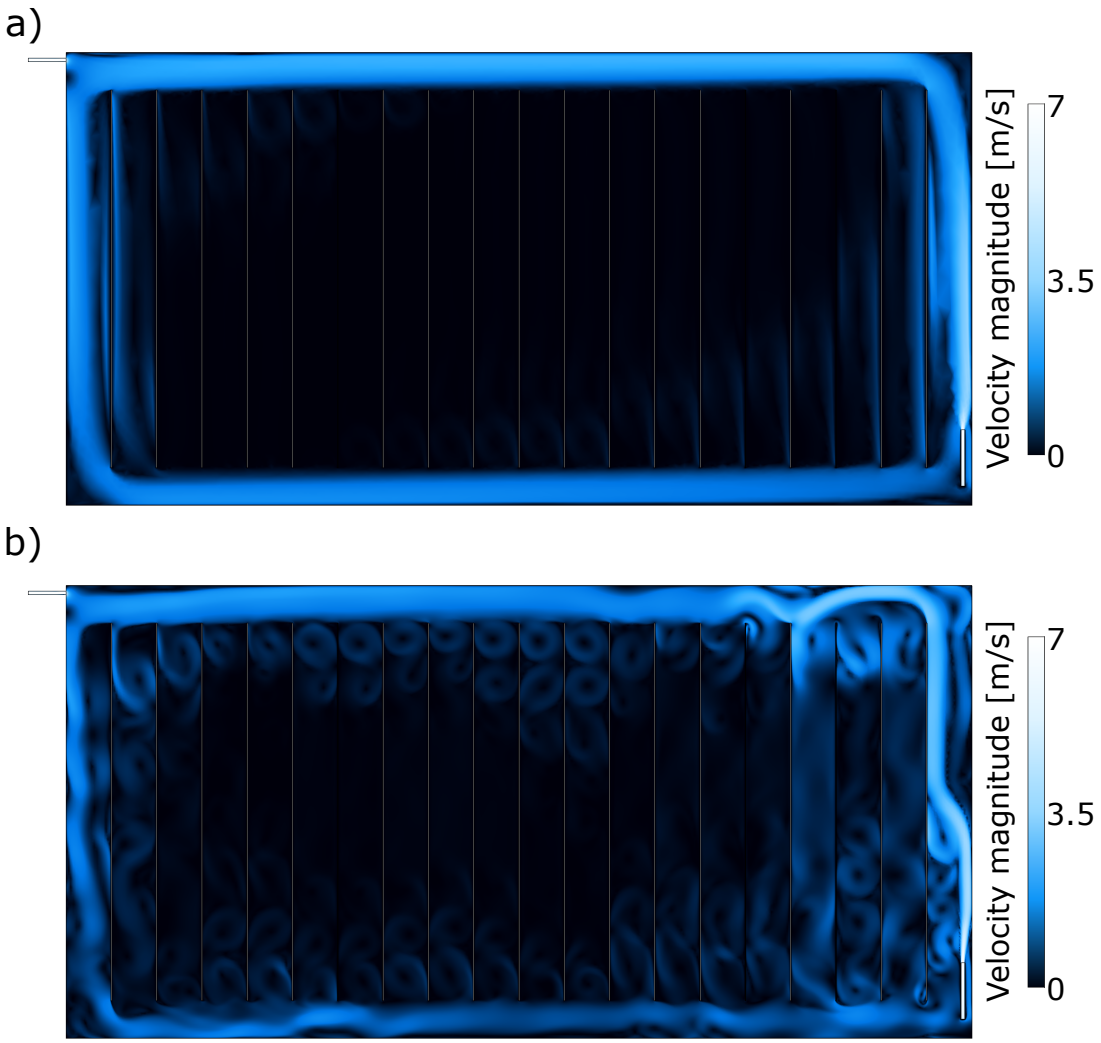

Figure 5.7.: Flow field after $t = 60\,\mathrm{s}$ in 2D geometry parallel to sODC with small inlet ($u_{in} = 5.24\,\mathrm{m\,s^{-1}}$) for a) a 'coarser' (NoE = 22,155), and b) an 'extremely fine' (NoE = 182,930) mesh.

reality. Experimental verification is addressed in Chapter 6.

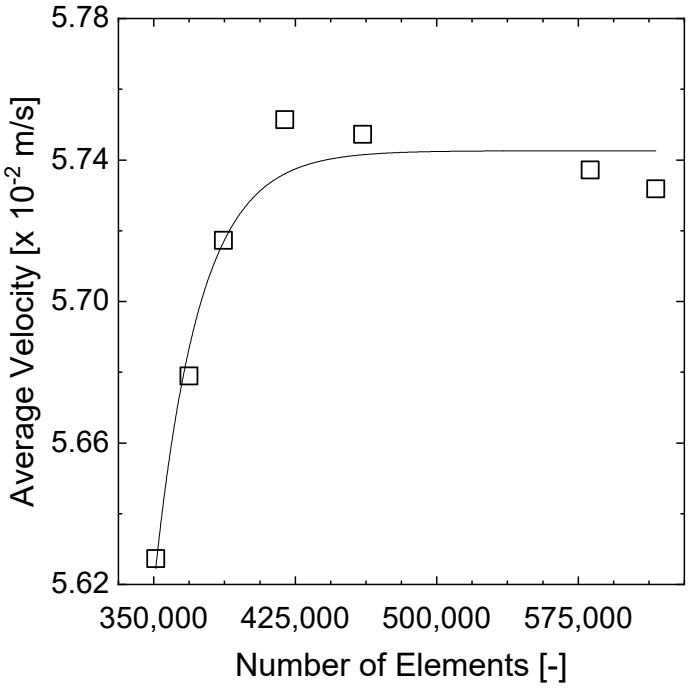

Figure 5.8.: Mesh independence study using a *Turbulent Flow* with the domain-averaged velocity over NoE (constant density, stationary flow field, boundary layers applied at walls).

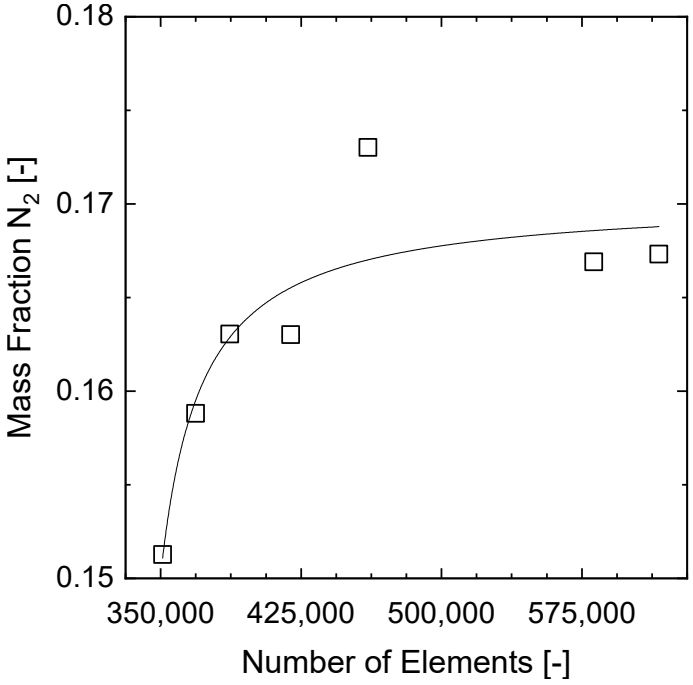

Figure 5.9.: Mesh independence study using a *Turbulent Flow* with the domain-averaged nitrogen mass fraction over NoE (constant density, stationary flow field, boundary layers applied at walls).

5.3.2. CFD Results of the Original Geometry

First, the original design with the assumed 19 vertical bars and the default top outlet was investigated. Figure 5.10 a) shows the stationary velocity field with streamlines of a turbulent κ-ϵ simulation and constant gas densities. Again, a counterclockwise flow along the outer walls can be identified by the streamlines. This frame flow exhibits higher velocities (indicated by white) than in the cell's center (indicated by black). In addition, the streamlines form circular vortices in the top parts of the channels, and one vortex appears in the bottom part of the second-last channel.

In contrast to the flow at the outer walls, velocities are almost zero in the center of the cell. In this area, mass transport is dominated by diffusion, which is magnitudes slower than convection. Regions of low flow velocities are disadvantageous for a fast mass transfer. Therefore, the mass fraction distribution is taken into account in the following. Figure 5.10 b) shows the corresponding mass fraction distribution of the same simulation after 500 s. Here, an oxygen-filled cell was flushed with nitrogen (inflow concentration of $w_{N2,in} = 1$). The main frame flow at the outer walls carries mainly nitrogen. The mass transfer is dominated by convection in these areas of high flow velocities. After 500 s, the gas compartment is almost filled with nitrogen (in white) except for two locations with oxygen accumulation in red and black. One remaining oxygen accumulation is in the second-last left channel (in red). The accumulation matches the observation of a vortex in the velocity distribution. In addition, an accumulation is found in channels two to four from the right (in yellow). Regions of low flow velocities seem to correlate with poor mass transfer (low nitrogen mass fraction). The flow distribution in Figure 5.10 b) is supposed to have a retarding effect on the flushing time because it will take longer until the entire oxygen is removed from the cell by nitrogen. The supporting bars inside the cell are critical elements for the flushing process as they block the free flow and extend the flow path inside the cell. The areas of low nitrogen mass fraction in the right quarter and at the bottom of the second-last channel can be identified as potential dead zones. Finally, the flushing time using a *Turbulent* κ-ϵ model and constant gas densities in the original cell geometry was calculated to 2200 s.

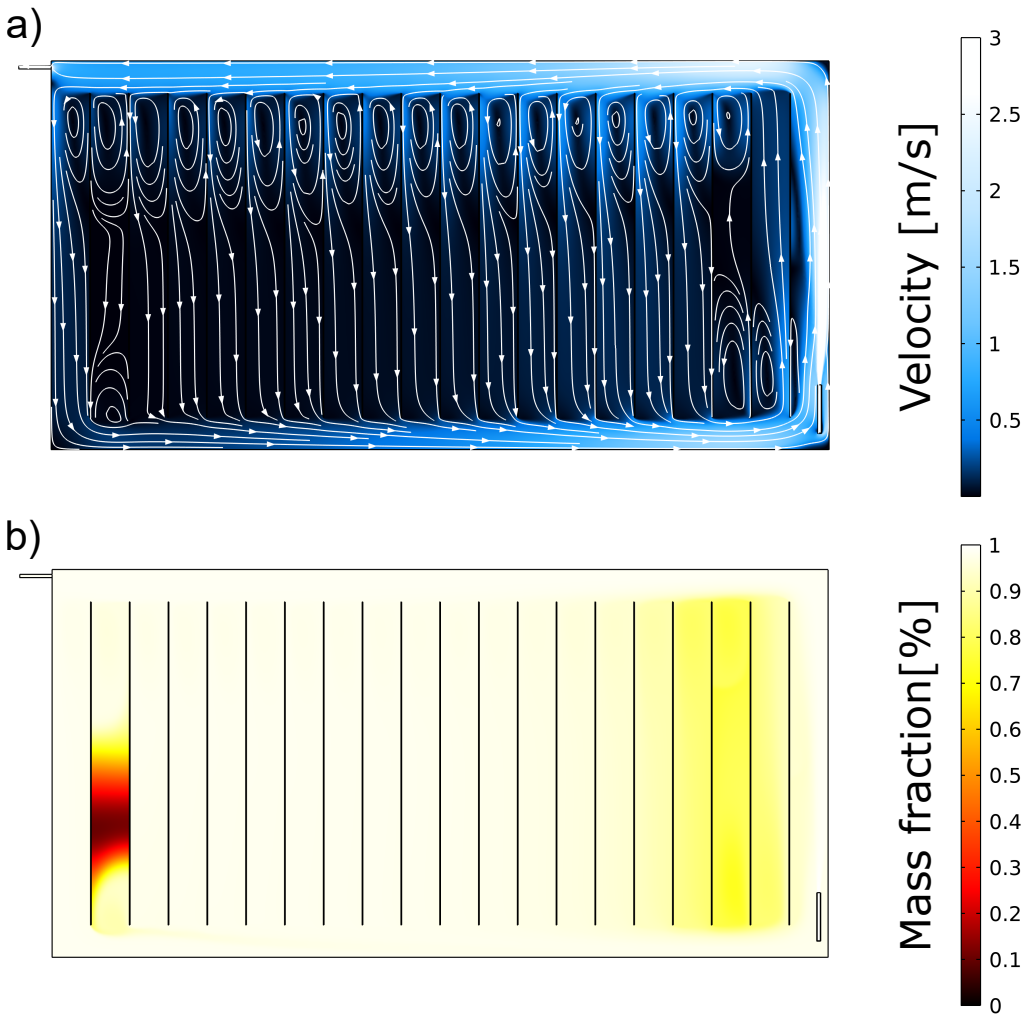

Figure 5.10.: a) Velocity field (turbulent κ-ϵ model), and b) concentration distribution (average nitrogen concentration) after t = 500 s of the original cell geometry.

The second section view (see Figure 5.3) is evaluated to estimate any flushing delay due to mass transfer in the porous sODC. Figures 5.11)a) and b) show the channel inflow after 0.5 s and 1 s, respectively. nitrogen enters from the right and distributes over the whole channel. The uniform nitrogen front is similar to plug flow. Over time, the entering nitrogen increasingly mixes with the remaining oxygen. The mixing leads to a transient concentration profile at the outlet after 7 s (Figure 5.11)c) or 8 s (Figure 5.11)d). The velocity is almost constant in the whole channel. However, the velocity is nearly zero inside the sODC, and mass transport is prevalently diffusive. A perforated plate holds the sODC in place and serves as structural support.

It takes 6 s for complete gas exchange in the empty channel beneath the plate. On the other hand, the gas exchange takes 8 s for the sODC. The gas exchange in the sODC prolongs the flushing time by additional 33 %. In the first approach, this safety margin can also be applied to the flushing times of other geometries. Applying this safety margin, the flushing time for constant gas densities and the original cell geometry can be corrected to 2938 s.

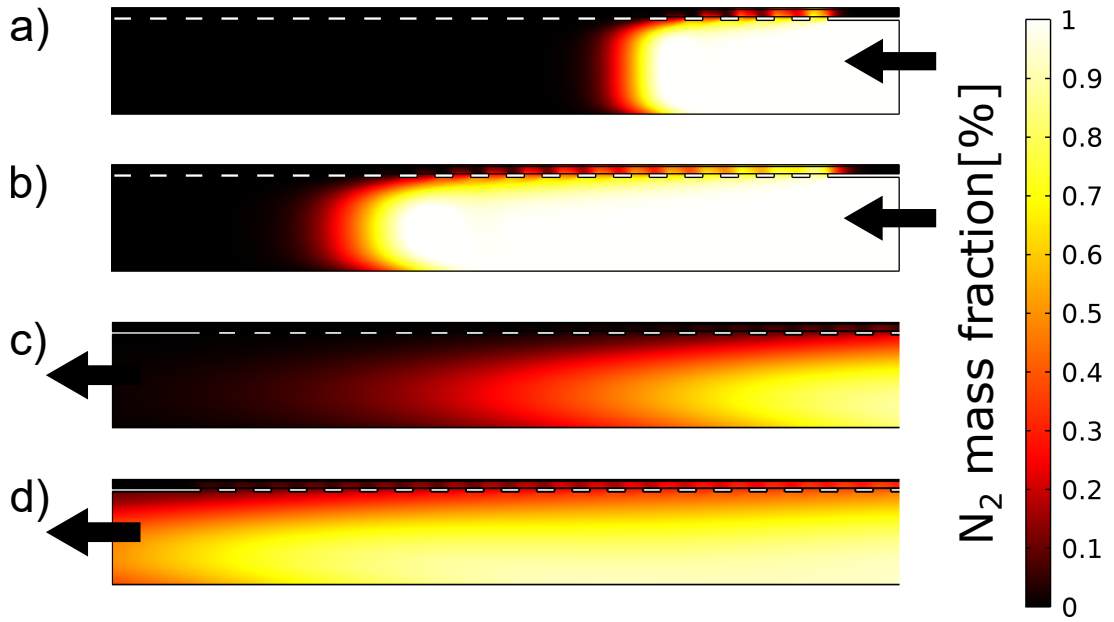

Figure 5.11.: Close-up of the perpendicular view of a channel showing the nitrogen mass fraction at the inlet after a) 0.5 s and b) 1 s; in the outlet at c) 7 s and d) 8 s (*Laminar Flow*, '2nd section view', inflow from the right, outflow to the left).

5.3.3. CFD Density Simulations

The previous simulations assumed constant density for all gases involved. However, the gas densities of oxygen, hydrogen and nitrogen vary between 0.0899 kg m^{-3} to 1.429 kg m^{-3} [Vere2013], creating different mixtures inside the gas compartment during the flushing procedure. Thus, different gas densities and their intermixing are considered in the following simulations. The simulations aim to evaluate the effect of gravity on the flushing procedure. Figure 5.12 shows concentration distributions using the default top outlet (Figures 5.12 a) and 5.12 b), or a new bottom outlet (Figures 5.12 c) and d)

after 50 s. oxygen is indicated by black, while nitrogen is colored in white.

In Figure 5.12 a), the heavier oxygen (black) enters at the bottom right and displaces the lighter nitrogen (white) towards the top left. The first three channels on the right quickly fill with oxygen. oxygen accumulates in the lower part of the gas compartment. The upper left quarter still contains a large amount of nitrogen after 50 s (yellow area equals approx. 20-30% oxygen). In Figure 5.12 b), the lighter nitrogen enters an oxygen-filled volume. nitrogen accumulation can be observed in the top transverse channel. From the upper channel, the nitrogen flows from top to bottom into the individual channels. After 50 s, there is still a high amount of oxygen in the left part of the cell.

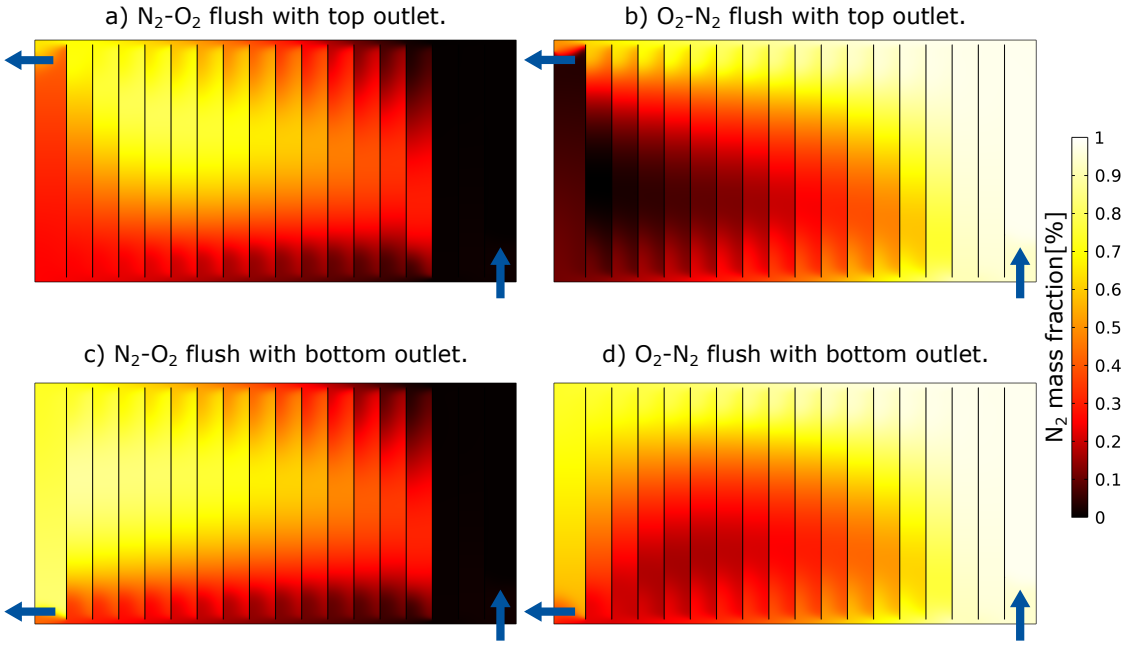

Figure 5.12.: CFD simulations after 50 s under consideration of different gas densities and two different outlet positions (*Turbulent Flow* interface, time-dependent).

Based on these results, a second outlet was implemented at the bottom of the left cell wall. It was investigated whether the second outlet affects the flow distribution in the gas space. In Figure 5.12 c), the heavier oxygen enters through the bottom right inlet while now the lower left outlet is used. The three channels on the right quickly fill with oxygen. Again an oxygen layer

forms in the lower horizontal channel, but this time it is less pronounced: The oxygen accumulation in the lower horizontal channel is almost absent, in contrast to 5.12 a). This time, a more concise residual is visible in the upper left quarter (yellow area indicating a higher nitrogen concentration than in the remaining compartment). In Figure 5.12 d), the entering lighter nitrogen flows directly upward and forms a continuous layer in the upper horizontal channel. From the top, nitrogen moves down into the individual channels. The far left channel is filled more quickly via the frame flow than those to its right. A residual amount of oxygen remains here in the lower left quarter (red indicates low nitrogen concentration).

Figure 5.13 shows the temporal course of the minimal oxygen mass fraction within the first 180 s of the density simulations. In the filling process with heavier gas, oxygen was purged in a nitrogen-filled gas compartment. In that case, the concentration increases. The heavier oxygen fills the compartment from bottom up. Thus, the fastest concentration increase can be observed with the top outlet. Using the bottom or both outlets causes a slight time delay. There is only a small advantage to using the bottom outlet rather than both.

In the process of filling with lighter gas, nitrogen is induced at the bottom-right inlet. During this step, the concentration decreases in Figure 5.13. According to Figure 5.12, nitrogen distributes quickly in the top horizontal channel and from there displaces the heavier oxygen. Thus, the top outlet takes the longest to detect any oxygen residues in this case. On the other side, the bottom outlet represents the fastest decrease in concentration. The concentration course of both outlets runs in between and is surpassed by the top outlet at the end.

Simultaneous solution of velocity and concentration distribution at variable and mixed gas densities with flow coupling is computationally intensive and, therefore, could only be performed for the first 50s. Thus, determining precise flushing times is not possible at this point. In summary, it can be concluded that the bottom outlet should be used when displacing with lighter gas ($w_{in,N2} = 1$) and the top outlet when replacing with heavier gas

($w_{in,O2} = 1$) to achieve thorough replacement.

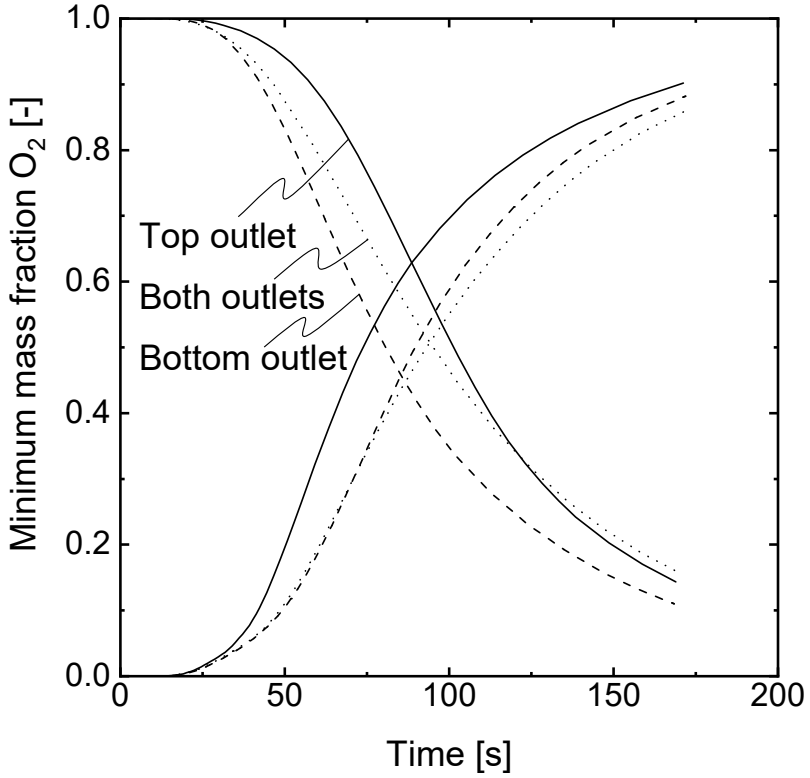

Figure 5.13.: Minimal mass fraction over time for flushing with heavier gas (N_2-O_2, increasing course) and with lighter gas (O_2-N_2, decreasing course).

5.4. Conclusion

CFD simulations were modeled by combining flow simulation and mass transfer. The aim was to replicate the nitrogen-flushing and oxygen-filling of the gas compartment of a commercial CAE cell. It has been shown that a coarse mesh below a certain number of mesh elements distorts the simulation result. Therefore, mesh refinement was an essential part of this chapter. Furthermore, there was an unfavorable combination of a very small inlet at high inlet velocity on the one side and a large volume with significantly lower velocities on the other side. Since the flow profile selection affects the simulation results but could not be determined by Reynolds number due to the significant velocity differences, both laminar and turbulent models, have been tested.

The gas compartment contains vertical internals, which stabilize the porous sODC but also affect the gas flow. The numerous internals cause flow deflections orthogonal to the main frame flow and can lead to time-variant eddies in the vertical channels despite low flow velocities. It was shown that using the *Laminar Flow* interface leads to a detailed but time-consuming reproduction of this flow pattern. The vortices change their location and shape with time. In combination with mass transfer correlations, the vortices seem to trap the initially present gas and impede exchange with the incoming new gas. The *Turbulent* κ-ϵ model managed to even these vortices and lead to a stable, stationary flow field. However, it has to be clarified whether the observed vortices occur in reality and if they affect the gas exchange. Experiments, more precisely flow visualization, aim to investigate this in Chapter 6.

To determine the flushing time of the original cell design, the minimum nitrogen mass fraction was evaluated from 2D simulations using the *Turbulent* κ-ϵ model and constant gas densities. Moreover, this flushing time represented the convection-dominated gas compartment and was assigned an additional safety margin to flush the porous sODC. Finally, the total flushing time was determined to 2938 s (36.7 min).

The simulation of the original design revealed significant dead zones. Areas of low nitrogen mass fraction were identified in the right quarter and at the bottom of the second-last channel and can be potential dead zones. In these areas, diffusion-dominated mass transport occurs, prolonging the nitrogen flushing of the gas compartment.

Further simulations considering the density differences of the gases have shown a significant influence on the distribution of the entering gas: lighter gas distributes directly to the top channel after entering and from there flows into the individual channels; heavier gas descends to the bottom of the cell and fills it from bottom to top. Thus, in addition to the left top outlet, an additional bottom outlet was added to the left cell wall. This outlet enabled an advantageous utilization of the gas density differences. First simulations promised a faster and cleaner gas exchange according to the respective

outlet. These findings are examined in the experiments of the following Chapter 6. The geometry can be further optimized to obtain a flushing time as short as possible while keeping the covered active area and pressure drop low. A genetic algorithm, such as the Gaussian Regression Process, can face this optimization problem. Optimization possibilities are discussed in Chapter 7.

6. Experimental Visualization of Gas Flow in an Industry Cell

6.1. Introduction

While Chapter 5 discussed a CFD model of the flushing process between the hydrogen- and oxygen-filled gas compartment in switchable CAE, experimental validation is essential to ensure safe operation in reality. The previous chapter unraveled obstacles to a secure and complete flushing procedure. CFD simulations showed that the stabilizing elements of CAE gas compartments impede unhindered gas flow and lead to shielding effects. These internals pose a risk of dead zone formation and prolong the gas exchange between hydrogen and oxygen. In addition, a pronounced dependency on different gas densities was identified. Experiments shall further validate these hypotheses.

The present chapter shows the results of the experimental visualization of the gas flow in an industry-sized CAE gas compartment. For this purpose, the gas compartment is isolated from the rest of the CAE cell and covered with a plastic pane. Here, the simulation results of Chapter 5 are compared to the experimental observations for the flushing procedure in the gas compartment. In agreement with the lab-scale experiments of Chapter 3 no current is applied and no reactions take place.

According to Figure 5.1, the flushing process covers

- a nitrogen flush of a hydrogen-filled compartment and subsequent filling with oxygen after the H_2 mode,
- a nitrogen flush of a oxygen-filled compartment after the O_2 mode.

The oxygen concentration is monitored in multiple locations during the flushing process to evaluate the flushing time. It is desired to keep the flushing time as short as possible to reduce the electrolyzer´s downtime and minimize the amount of waste gas. In addition, the flow is visualized utilizing a fog generator to identify potential dead zones. Dead zones should be avoided to reduce the risk of explosive oxyhydrogen formation. In particular, the fog experiments highlight the influence of higher gas density and visualize emerging flow patterns. Finally, the results of the concentration and fog experiments are used to rate the cell geometry and, if necessary, to

optimize the design. As far as possible, adjustments to the cell geometry are implemented and tested compared to the original geometry.

6.2. Experimentals

6.2.1. Implementation of an Industry-Scale Setup

Figure 6.1 shows a commercial electrolysis cell with a gas compartment, flow distributors, an elastic mesh and the sODC from left to right. The gas compartment of the cell was isolated to perform concentration and flow visualization experiments. The gas flow through the compartment was investigated with no current applied and no reactions taking place.

Setup

Figure 6.2 shows the experimental setup. A pressure regulator reduced the pressure to the required 2 bar pre-pressure entering the gas flow controller (model 35836, Anolyt MTC, Müllheim, GER).

Furthermore, the gas flow controller measured pressure and temperature. Additionally, the temperature was measured before the inlet of the cell (Pt100 temperature sensor TDIP15, Pyroscience, Aachen, GER). Via flexible polyurethane (PU) tubes with 12 mm outer diameter (OD), the gas was directed to the pressure sensor (S-11, WIKA Alexander Wiegand, Klingenberg am Main, GER) and finally to the cell inlet. At the cell outlet, gases were disposed of at ambient pressure. A minimum length of 12 mm OD tubing at the cell outlet, leading to an exhaust hood, ensured low back pressure. An oxygen sensor and an outlet pressure sensor (S-11, WIKA Alexander Wiegand, Klingenberg am Main, GER) were installed at the cell outlet. T-connectors and shut-off valves were installed to switch between operations with and without the fog generator. In the case of fog experiments, the gas was re-directed to a glass tube with 10 cm inner diameter (ID) for fog mixing. In the glass tube, fog from a fog lance entered via one large inlet, mixed with the nitrogen entering through a second inlet. The

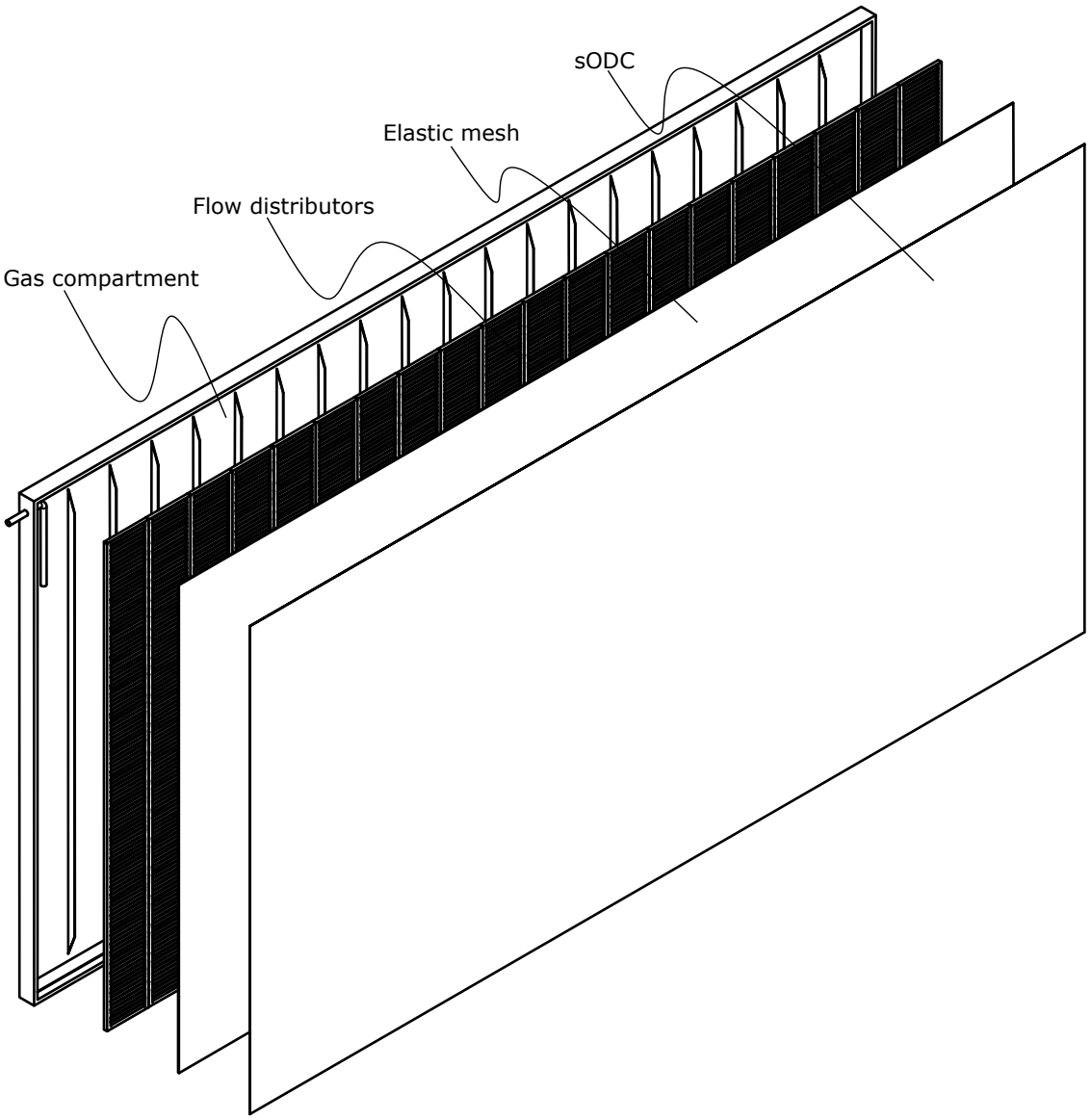

Figure 6.1.: Electrolysis cell with the gas compartment, flow distributors, an elastic mesh and the sODC from left to right.

nitrogen-fog mixture was then discharged inside the industry cell. A control box (ZUMOLab, Wesseling, GER) monitored the devices and tracked the data points. This setup enables high-resolution online measurements for optimal monitoring of the concentration and flushing experiments.

Experiments were performed at room temperature. The volume flow was adjusted to 60 L min^{-1} in most cases, and additionally to 75 L min^{-1} and 90 L min^{-1} at elevated volume flows. The outlet of the cell was directed into a local extraction device.

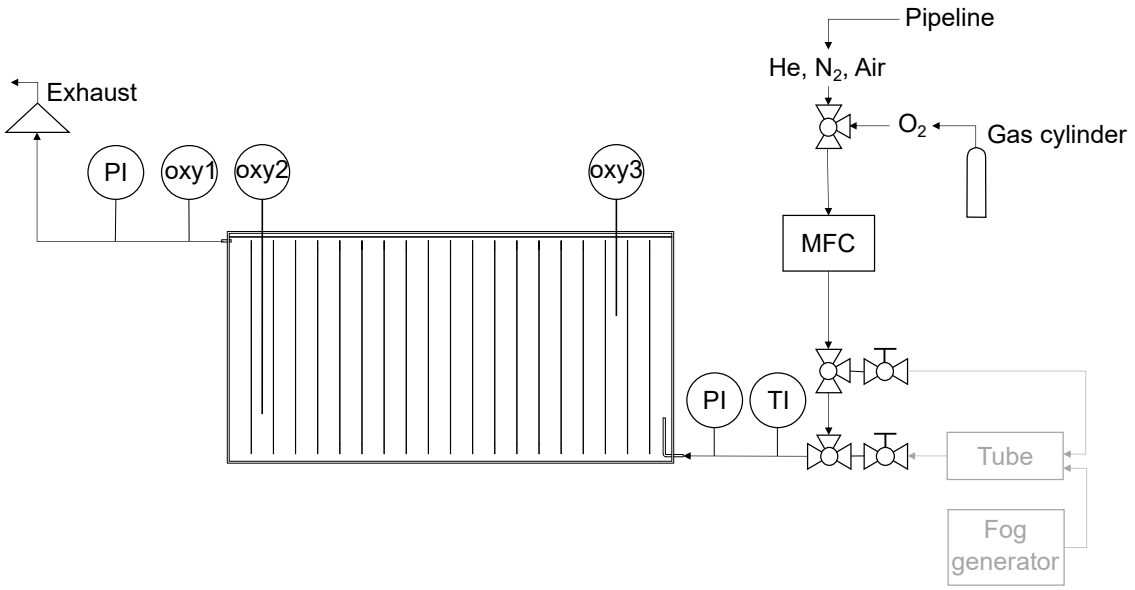

Figure 6.2.: Flow chart of the experimental setup including a mass flow controller, several sensors and a variably connectable fog unit leading to a simplified sketch of the cell.

Devices

Any unnecessary inner parts were removed to enable a direct view of the inner part of the cell. Unneeded inlets were trimmed and welded shut as close to the cell body as possible. The inner part contained vertical bars with cutouts at the top and at the bottom ends to enable horizontal gas exchange. A 10 mm polycarbonate (PC, Nordic Panel, Stade, GER) pane was installed on top of the frame for visual investigation. In addition, three additional vertical supporting beams were installed onto the PC pane for stability reasons (marked in Figure 6.4). For adequate gas investigation, several requirements for the analysis methods should be fulfilled:

- Detect a large range, preferably 0 vol.-% to 100 vol.-% oxygen to monitor the full flushing process,
- Accurate measurement method ($<$ 0.1 vol.-% oxygen),
- Fast response time to be able to run a fast transient measurement ($<$ 5 s),
- Little cross-sensitivity to other gases, and

- Flexible with the possibility to measure at different spots.

Based on those requirements, the ultra-fast and -sensitive Pyroscience oxygen sensor (OXROB 10 sensors, FireSting-PRO FSPRO-4, both Pyroscience, Aachen, GER) was selected to detect oxygen. The principle of operation of the oxygen sensor is explained in more detail in the appendix (see Chapter A). The oxygen concentration was measured at the outlet (probe oxy1 in Figure 6.3), and at two potential dead zones detected in Chapter 5. Figure 5.10 of the CFD simulations shows the concentration distribution after t = 500 s (at that time an average nitrogen concentration of 95 % is reached). The concentration distribution reveals potential dead zones in the outer quarter on the right and the bottom left part. Therefore, the additional oxygen samples oxy2 and oxy3 are positioned as marked in Figure 6.3.

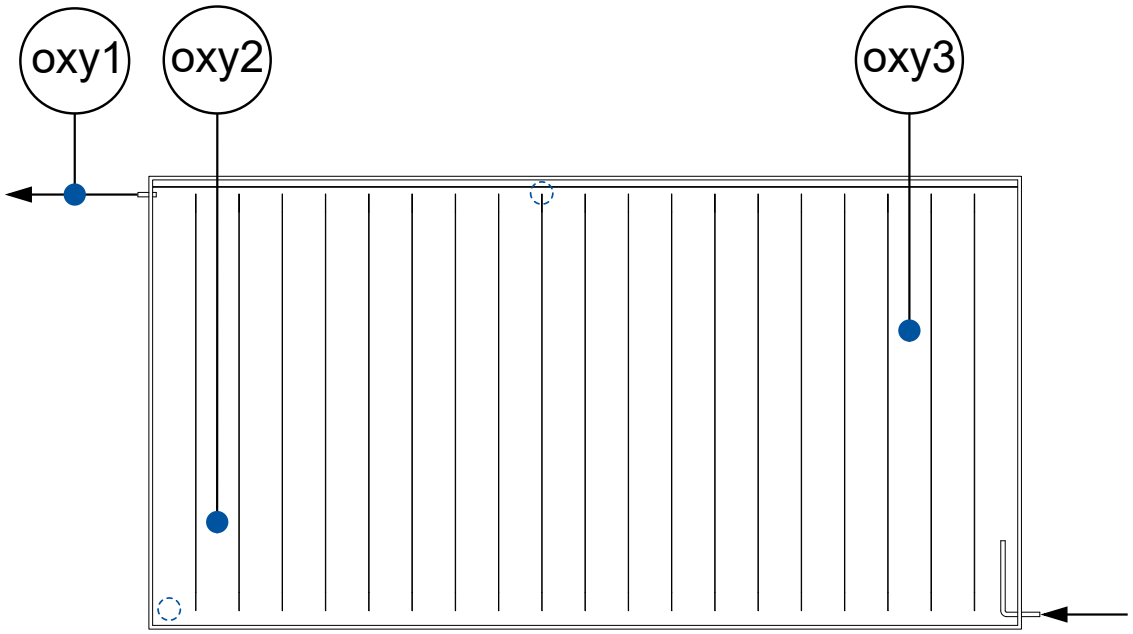

Figure 6.3.: Location of the oxygen sensors oxy1-oxy3 and suggested sensor locations for future experiments (dotted circles)

Gas probes were taken via gas bags at times between 25 s and 5 min, depending on the gas combination, to measure argon (Ar) or helium (He). On the basis of the conducted CFD simulations, concentration measurements

were established at the outlet. The content of the gas bags was evaluated using the gas chromatograph Trace GC Ultra (Thermo Scientific, Waltham, US).

A fog generator (fog lance NS2, Safex, Tangstedt, GER) was used for the flow visualization experiments. The fog generator produces homogeneous particles from evaporating polyols (Heavy Fog, Smoke Factory, Großburgwedel, GER). The generator heated the polyol and distributes the evaporating fluid via a 2 mm metal nozzle in the fog lance. Mixing was done in a glass tube with an inner diameter of 30 mm. The ends were covered with 3D-printed adapter pieces printed in RGD525 High Temperature (3D printer: Objet Eden 260V, Stratasys, Eden Prairie, USA). An O-ring ensured the sealing between the adapter and the glass tube. The glass tube had two boreholes at the inlet: A 12 mm connector for the air supply and a thread for a 4 mm PTFE pipe to guide the fog inside the glass tube. At the end of the glass tube, a thread connected a 12 mm tube with the setup. nitrogen was provided via the gas flow controller to the mixing tube. The fog-nitrogen mixture passed the pressure gauge and entered the standard cell inlet. The fog experiments were monitored using a Nikon 750D camera, placed on a tripod orthogonal affronting the cell.

The area opposite the industry cell was covered with black sheets reducing reflections and enabling appropriate photographs. Figure 6.4 shows a photograph of the setup, including the industry cell, the fog lance, the mass flow meter and sensors, the camera and a black background cover. Experiments included filling the empty cell with fog and flushing a fog-filled cell with nitrogen at 60 L min^{-1}.

Materials

Concentration measurements with pure gases and visualization experiments with a fog generator and nitrogen as carrier gas were performed. For the concentration measurements, oxygen (oxygen 3.5, Westfalen AG, Münster, GER) was used for the O_2 mode, helium (helium 5.0, Nippon Gases, Madrid,

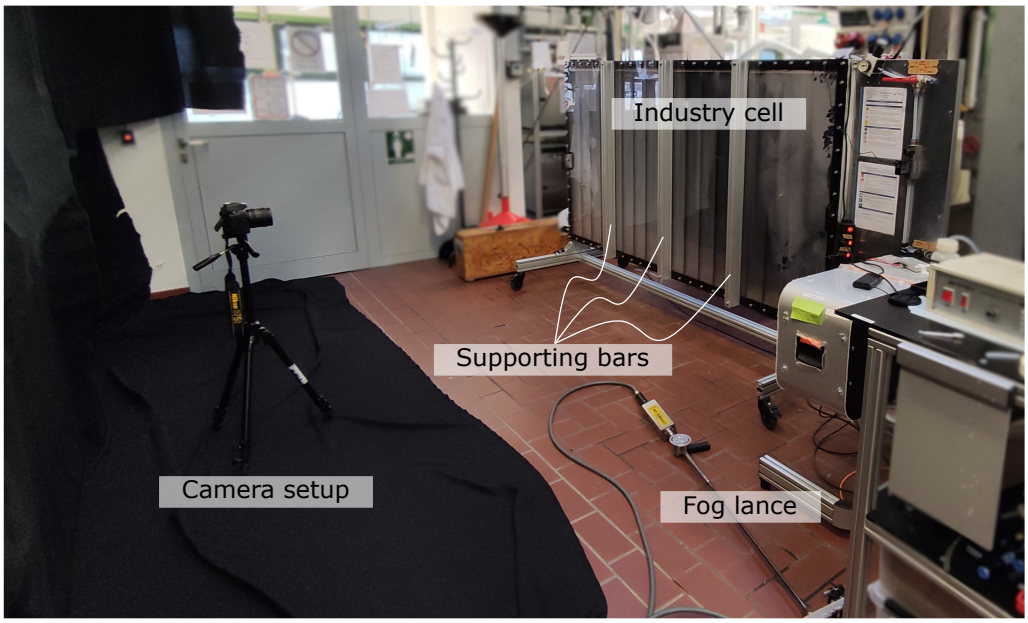

Figure 6.4.: Photograph of the setup including the industry cell, the fog lance, the camera and black background cover.

ESP) as a substitute for the H_2 mode, nitrogen (nitrogen 5.0, Westfalen AG, Münster, GER) as a flushing gas, and synthetic air (Air Products, Allentown, US) as well as argon (argon 5.2, Air Products, Allentown, US) as additional gases. Table 6.1 summarizes the materials used.

Table 6.1.: Details of the gases used in this thesis

Gas	Supplier	Marking	Purity [vol-%]	Density [kg m^{-3}]
Helium	Nippon Gases	Helium 5.0	99.999 %	0.1785
Nitrogen	Westfalen	Nitrogen 5.0	99.999 %	1.15
Artificial Air	Air Products	Zero	20.9 %	1.225
Oxygen	Westfalen	Oxygen 3.5	99.95 %	1.31
Argon	Air Products	Argon 5.2	99.998 %	1.784

Efficiency Factor

The flushing time depends on the density of the gas used and the volume flow entering the cell. Therefore, a dimensionless parameter is used to assess the suitability of different gases for the flushing process. This parameter, introduced as the *efficiency factor*, puts the total flushing gas volume V_{flush} required to complete a flushing process with the cell volume V_{cell} in relation. The efficiency factor enables the comparison between gases independent of the selected volume flow.

6.2.2. Experimental Procedure

Following the theoretical scheme for the flushing procedure in Figure 5.1, a similar sequence is implemented for the flushing experiments according to Figure 6.5. oxygen was replaced by artificial air in experiments with higher flow rates in the switching procedure O_2 to H_2 mode. For safety reasons, hydrogen was replaced by helium in the switching procedure H_2 to O_2 mode. First, the helium-filled gas compartment was flushed with artificial air to enable detection of oxygen. For the second part of the flushing procedure, a nitrogen-filled compartment was filled with oxygen. oxygen was replaced by artificial air in the experiments at elevated volume flows (75 and 90 L min^{-1}). In the case of artificial air, the explosion limits were scaled accordingly the air composition.

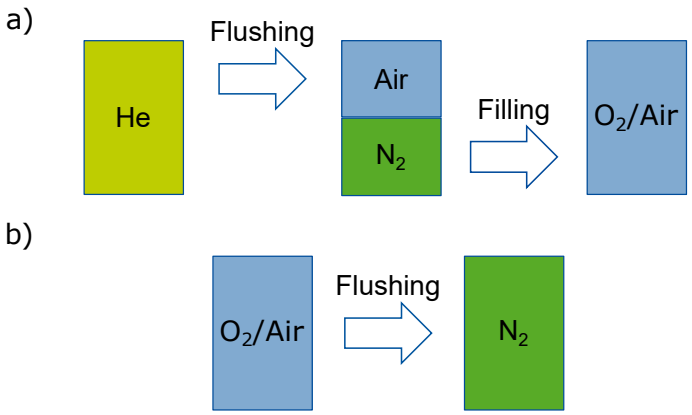

Figure 6.5.: Switching procedure of the experimental investigations of a industry cell for the switching a) H_2 to O_2 mode, and, b) O_2 to H_2 mode.

6.3. Results and Discussion

6.3.1. Fog Results

The fog experiments aimed to visualize the flow distribution in the entire gas compartment directly. First, in addition to the pressure difference measurements in Chapter 6.3.2, the pressure difference was determined to 20 mbar to 25 mbar when the fog was used.

In the first fog experiment, the nitrogen-filled compartment was filled with fog. This represents the change from H_2 mode (lighter gas) to O_2 mode (heavier gas). Figure 6.6 a) shows images at different time steps with the fog entering at the bottom right and leaving through the top outlet on the left. The fog gradually fills the cell from right to left. After 24 s, the first right quarter is already filled with fog. However, the second and third images show a whiter space here (the fog gets denser). The image after 38 s shows individual fog streams moving downwards from an outer top frame flow in the second quarter. Also, a white horizontal area forms at the bottom wall, indicating accumulation due to the descent of the fog (visible in the image after 78 s). During the experiment, the fog fills the channels streak-like from the top. The fog falls chaotically through the individual channels. In the process, individual vortices form and decay irregularly (see images after 92 s and 116 s). The horizontal fog layer at the lower cell wall becomes denser with time. Finally, the fog becomes thicker in the right channels, where it was present first. The fog-filling process takes 1.9 min in total.

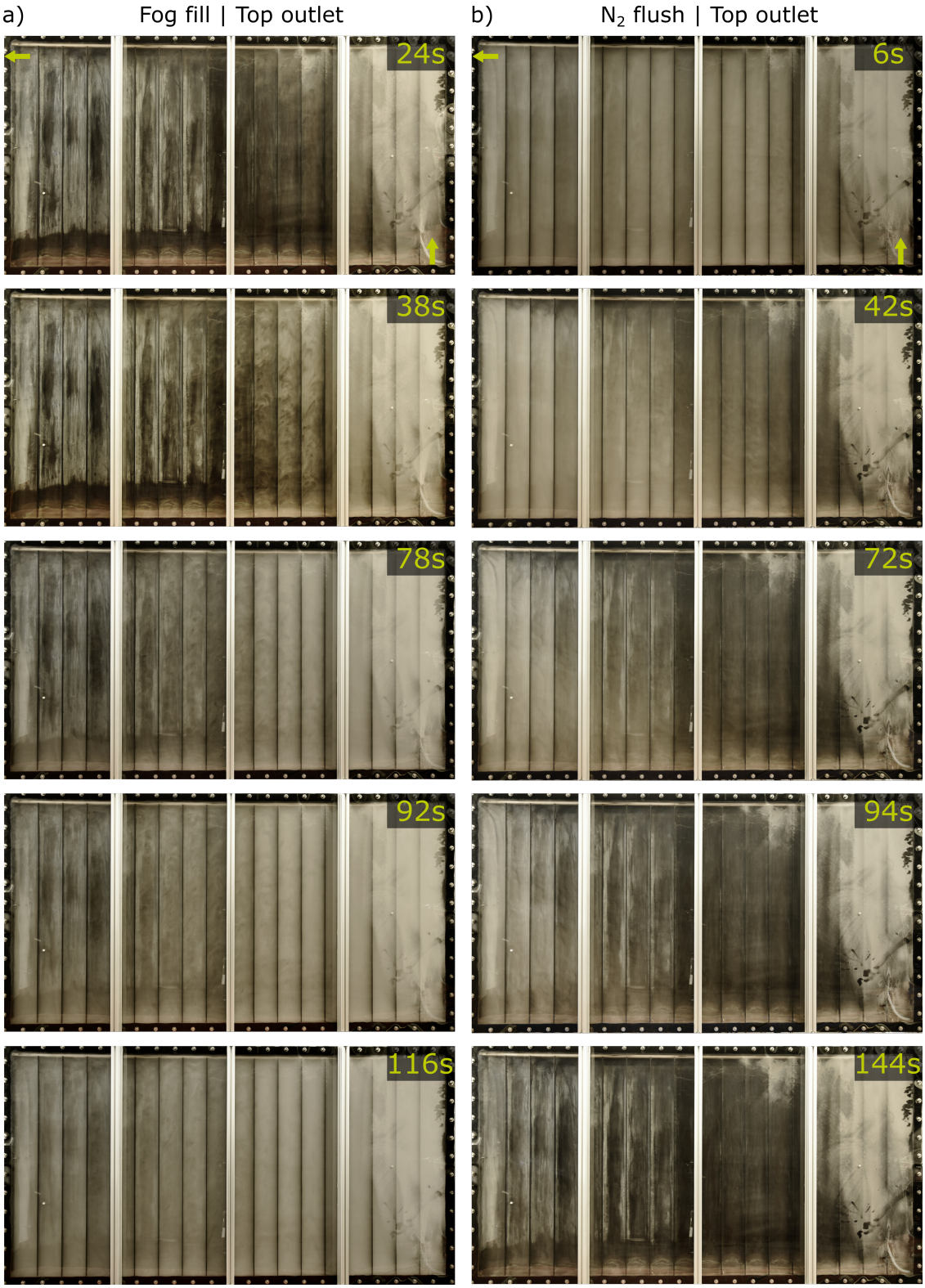

Figure 6.6.: Photos of visualization experiments at different time steps with a) fog and b) nitrogen at the inlet (bottom right) while using the top outlet.

In the second fog experiment, the fog-filled compartment is flushed with nitrogen. This represents the change from O_2 mode (heavier gas) to H_2 mode (lighter gas). Figure 6.6 b) shows images at different time steps with nitrogen entering at the bottom right and leaving through the top outlet on the left. The first image shows strong condensation in the right quarter since the entering hot fog causes a significant temperature difference here. After several seconds, nitrogen quickly distributes via the top horizontal frame channel towards the outlet on the top left (image after 6 s). nitrogen displaces the fog in the individual channels one after the other from top to bottom and right to left within the first four images. In the channels, irregular mixing effects with forming and decaying eddies occur. In the image after 72 s, fine streamlines of nitrogen and fog can be seen at the outlet. Finally, a visible layer of fog remains on the bottom wall across the entire cell width, visible in the image after 144 s. The layer can be observed for a very long time until the end of the process (approx. 2.9 min).

On the basis of the CFD simulations considering different gas densities in Chapter 5.3.3, a second outlet was mounted at the bottom left, as close to the bottom wall as possible. The fog experiments were repeated using the bottom outlet. Figure 6.7 shows images after different time steps while the bottom outlet is used.

In the fog-filling process, the entering fog quickly fills the first quarter on the right (image after 12 s in Figure 6.7 a). The channels to the left are filled chaotically and randomly from bottom to top (images after 40 s and 70 s). Vortices form and spread with time. In contrast to Figure 6.6 a), a thinner fog layer forms at the bottom, as the fog presumably escapes quickly through the bottom outlet. The filling of the cell occurs mainly from the bottom up, always with a simultaneous drag of fog through the bottom outlet. Almost a triangular fog front forms towards the outlet, which can be seen in images after 70 s and 270 s. The irregular fog distribution extends the filling process to about 5 min.

Finally, the cell is flushed with nitrogen again (Figure 6.7 b). As nitrogen enters, a fine transparent layer immediately forms in the horizontal top chan-

nel (image after 6 s). With time, the dense fog becomes more transparent channel by channel from right to left and slowly from top to bottom (image after 28 s). As the process proceeds, the fog becomes more transparent in all channels from the top down, with the fastest progress in the two right quadrants (image after 28 s). At the same time, an nitrogen short-circuit flow forms at the left wall directly to the outlet, creating fine unmixed streamlines of nitrogen and fog (image after 74 s). The longest accumulation of fog persists in channels 4-6 from the left. A fog residual in the bottom horizontal channel is still visible even after 142 s. The entire flushing process lasts about 2.5 min.

Based on the fog experiments, additional sensors can be placed in the top area around the seventh bar from the left and

bottom left corner to determine a more precise flushing time in the concentration measurements (indicated by dotted circles in Figure 6.3).

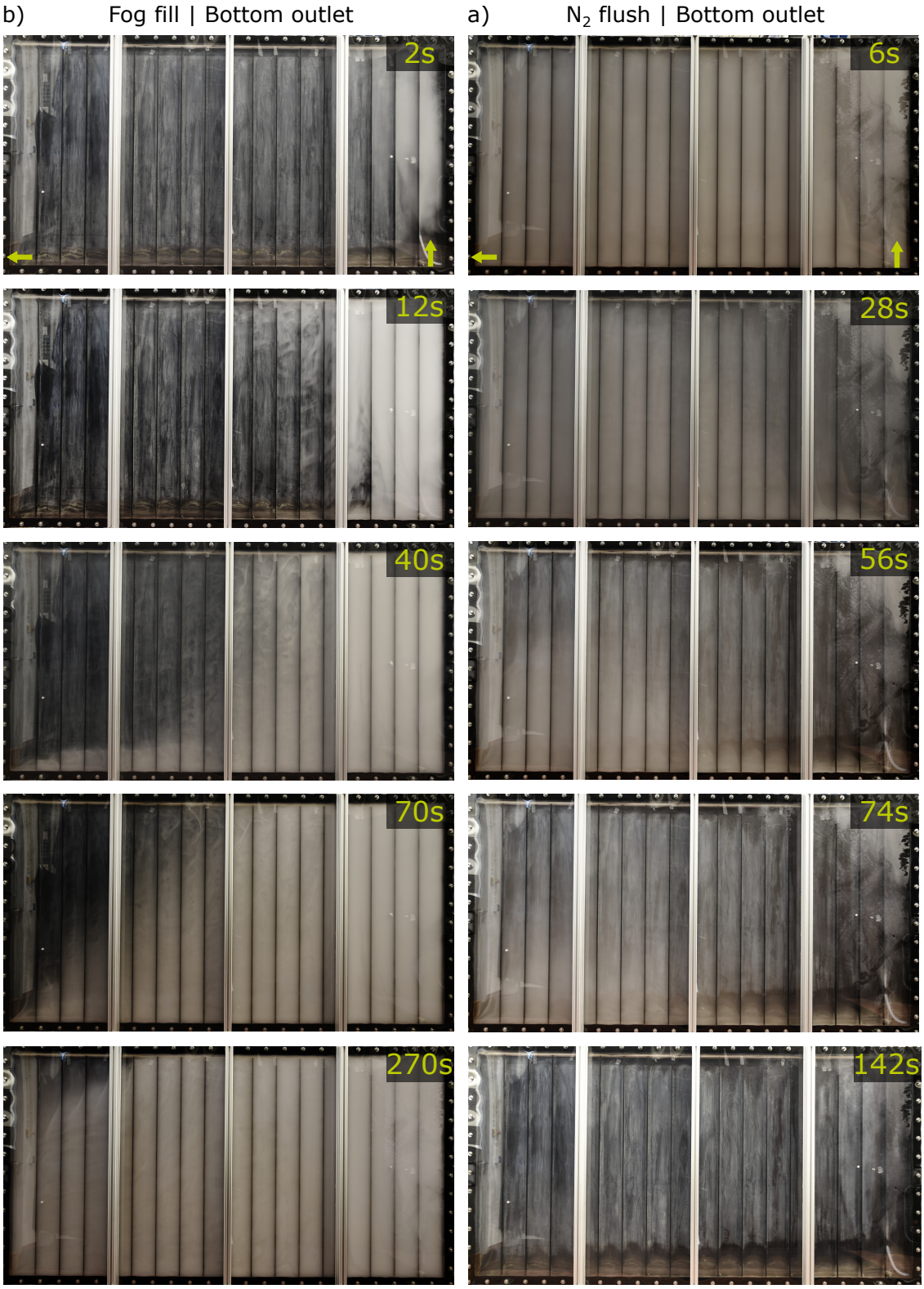

Figure 6.7.: Photos of visualization experiments at different time steps with a) fog and b) nitrogen at the inlet (bottom right) while using the bottom outlet.

6.3.2. Concentration Results

Before commissioning the experiments, the pressure drop over the cell is recorded for the three different volume flows and listed in Table 6.2.

Table 6.2.: Volume flow with the according pressure drop using air

Volume flow [L min^{-1}]	pressure drop [mbar]
60	9
75	13
90	17

A continuous measurement at the three measuring points oxy1-oxy3 is possible via the oxygen sensors and O2-containing gases. Thus, the time-dependent change in the gas composition can be investigated.

Top Outlet

Figure 6.8 a) shows the switching from nitrogen to oxygen as an example. oxy3, the sample in the 3rd channel from the right, is the first to detect oxygen. The oxygen concentration rises quickly in this sampling point and is the first to exceed the limit value of 96 %. oxy2 and oxy1 show no oxygen for a long time and then increase sharply with some delay to oxy3. Thus, in the N_2-O_2 alternation, the outlet is the last place where nitrogen is still encountered. The flushing time is determined by oxy1 to 184 s.

As the last sensor to exceed the explosion limit, oxy1 is located at the outlet. This leads to the conclusion that no hotspots are present and that nitrogen is completely removed from the compartment. However, as only three measurement points are available, it cannot be excluded whether hot spots can appear at other locations.

In the O_2-N_2 transition (Figure 6.8 b), the content of oxygen falls from 100 % to 0 % since nitrogen is now used for flooding. Figure 6.8 b) shows

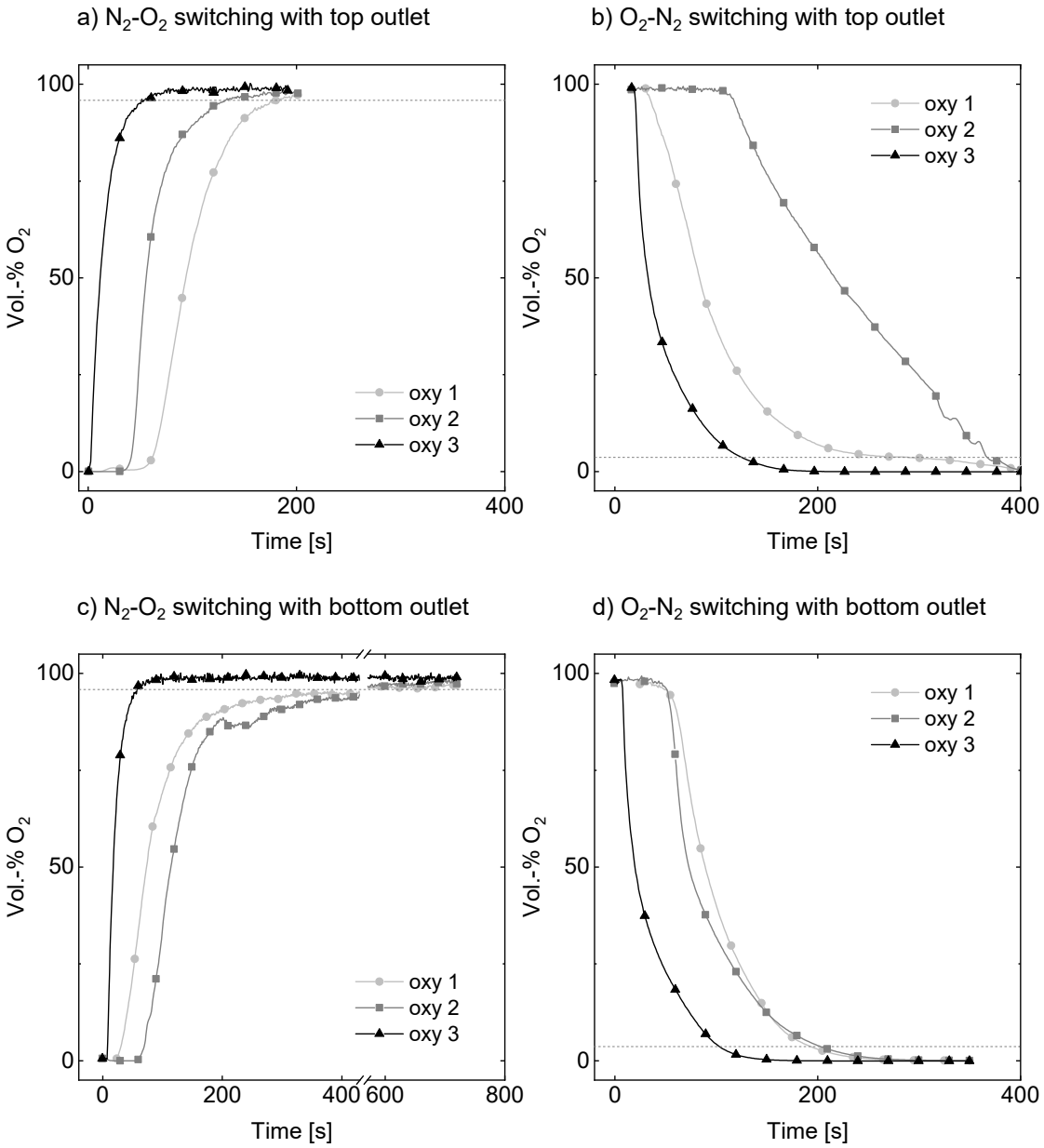

Figure 6.8.: oxygen concentration over time for various combinations of oxygen and nitrogen and top (a) and b) or bottom (c) and d) outlet.

an immediate drop of oxygen in oxy3. This time, oxy1 at the outlet follows shortly behind with a decline in oxygen. In oxy2, the measuring point in the second-last left channel, no change can be seen for a long time until a slow drop in oxygen initiates. Here, oxygen can be detected for the most prolonged duration. The flushing time is determined based on oxy2 to 351 s.

A threefold repetition of the experiments has shown good agreement between the measurements.

A qualitative comparison between fog experiments and concentration measurements shows good agreement: In the change from light to heavy gas, the right measuring point oxy3 detects a change first, followed by oxy2 and then oxy1, thus gradual flooding from right to left in the direction of the outlet. In the shift from heavy to light gas, a change in the outlet oxy1 follows shortly after the first change in oxy3. A change is detectable in oxy2 only after a long interval.

Bottom outlet

In a repetition of the O_2-N_2 experiments, the bottom outlet is used with all other conditions remaining the same. In both sequences, purging with lighter or heavier gas while using the bottom outlet, a change in concentration is directly detectable in sensor oxy3 on the right.

If the heavier oxygen is introduced, the rapid increase in oxy3 is followed by the sensor at the outlet, oxy1. Shortly afterward, the oxygen concentration also increases in oxy2. However, the overall gas exchange takes much longer than in the other constellations (see significantly longer x-axis in Figure 6.8 c). The flushing time is the longest of the four cases with 531 s.

Using the lighter nitrogen in Figure 6.8 d), the two sensors, oxy2 (second last channel) and oxy1 (at the lower outlet), follow oxy3 with some distance. There is only a slight difference in the concentration curve between oxy1 and oxy2. This suggests that, at this point, the flushing process is almost completed. oxy2 determines the flushing time with 194 s.

A significant difference between the O_2-N_2 switchings can be noted in the concentration course of oxy2: The concentration drop runs much slower and starts later in the case of the top outlet (Figure 6.8 b). Thus, a disadvantageous consequence can be assumed from the combination of lighter gas and the top outlet.

Qualitative similarity to the fog experiments can also be established when using the bottom outlet. If the gas compartment is filled with heavier gas

(oxygen or fog), a bypass flow develops at the left channel towards the bottom outlet. Oxy2, therefore, detects a drop in concentration last. In the second case, the lighter nitrogen promotes an almost simultaneous filling of the left channels when using the bottom outlet. However, it takes longer than in the oxygen flush until a change is detected in the outlet (oxy1).

Different Densities

As previously discussed, the density difference of the gases has a notable impact on the evolving flow pattern in the gas compartment. Concentration experiments were repeated with the system O_2-Ar to evaluate whether a denser gas than oxygen decreases the flushing time. The density difference between Ar-O_2 ($\Delta\rho = 3.355\,\mathrm{kg\,m^{-3}}$) is similar to O_2-N_2 ($\Delta\rho = 0.179\,\mathrm{kg\,m^{-3}}$). Therefore, the flushing of an oxygen-filled compartment with argon and the other way round were conducted at $60\,\mathrm{L\,min^{-1}}$ and the top outlet.

First, flushing with heavier gases is compared. Figure 6.9 shows the concentration gradient of a oxygen-flush of a nitrogen-filled gas compartment (squares), and a argon-flush of an oxygen-filled cell (circles). Data from sample point oxy3 on the right side is plotted in black and grey, oxy2 in the bottom left corner in green, and oxy1 at the outlet in blue. The darker colors indicate the N_2-O_2 flushing process.

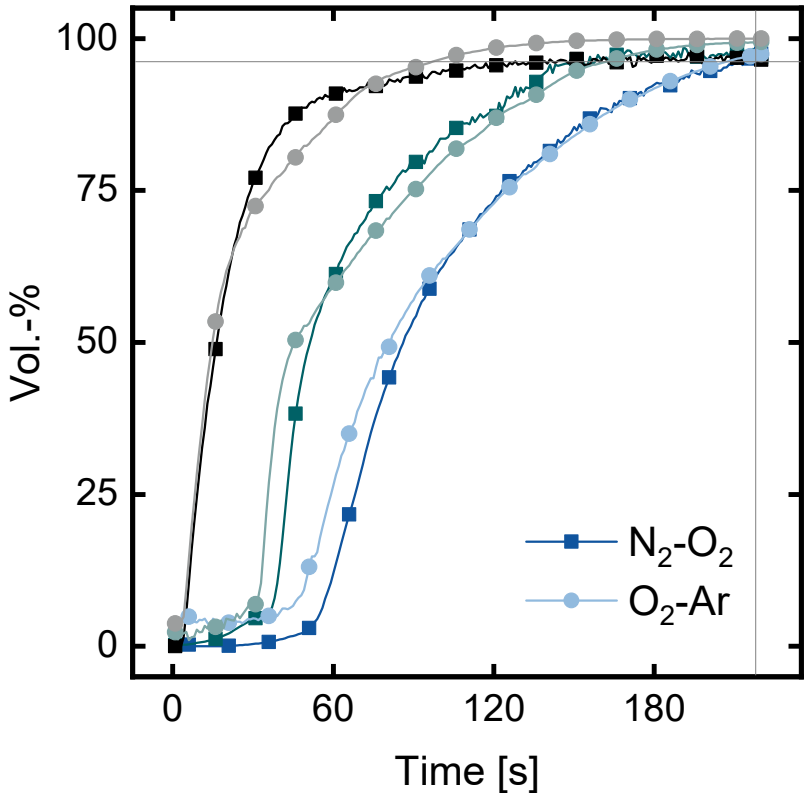

Figure 6.9.: Concentration gradient N_2-O_2 and O_2-Ar at 60 L min^{-1} (oxy3 - black, oxy2 - green, oxy1 - blue, top outlet).

A strong resemblance between the flushing processes can be observed. The concentration gradients show an almost identical course. Small deviations occur at 0 % and 100 %. The O_2-Ar change is slightly faster (199 s) than the N_2-O_2 change (214 s).

In addition, the flushing process was reversed to flushing with lighter gases. Figure 6.10 shows the O_2-N_2 (squares) and the Ar-O_2 (circles) concentration courses over time. Again, the darker colors indicate the O_2-N_2 combination. The data points match the observations of the flushing with lighter gas in Figure 6.8, as the concentration change in oxy1 (blue) at the outlet is followed by oxy2 (green) for both gas combinations. The total flushing times of 739 s for the O_2-N_2 flush, and 730 s for the Ar-O_2 flush are similar, but significantly longer than flushing with a denser gas in Figure 6.9.

Both plots prove the effect of the density difference. Furthermore, the results demonstrate that replacing the flushing gas to argon in the switching

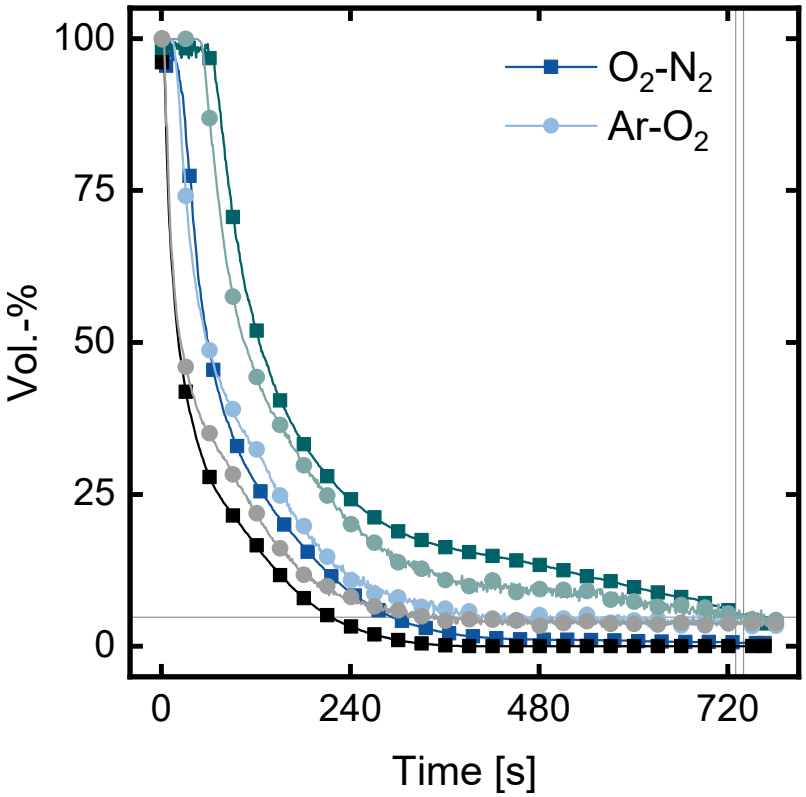

Figure 6.10.: Concentration gradient Ar-O_2 and O_2-Ar at 60 L min^{-1} (oxy3 - black, oxy2 - green, oxy1 - blue, top outlet).

from O_2 to H_2 mode can significantly reduce the flushing time.

The density influence on the flushing process was further investigated with other gas combinations. A He-Ar combination was added to create an even more concise density difference. While there is a density difference of $\Delta\rho = 1.61\,\mathrm{kg\,m^{-3}}$ for Ar-He, it is only $\Delta\rho = 0.16\,\mathrm{kg\,m^{-3}}$ for O_2-N_2. Similar concentration courses are observed for all four combinations (see Figure A.1). However, the Ar-He combination (bottom outlet) was the fastest, while the He-Ar combination (top outlet) had the longest flushing time. Particular linear correlations between the concentration courses could not be identified.

Different Volume Flows

Figure 6.11 displays the flushing times for various gas combinations at different volume flow rates using the top outlet. Increasing the volume flow substantially decreases the flushing time in all gas combinations. In the case of the Air-N_2 combination, it can be halved when increasing the volume flow by 25 % to 75 L min^{-1}. At 90 L min^{-1}, the flushing times are all quite similar only varying within 50 s.

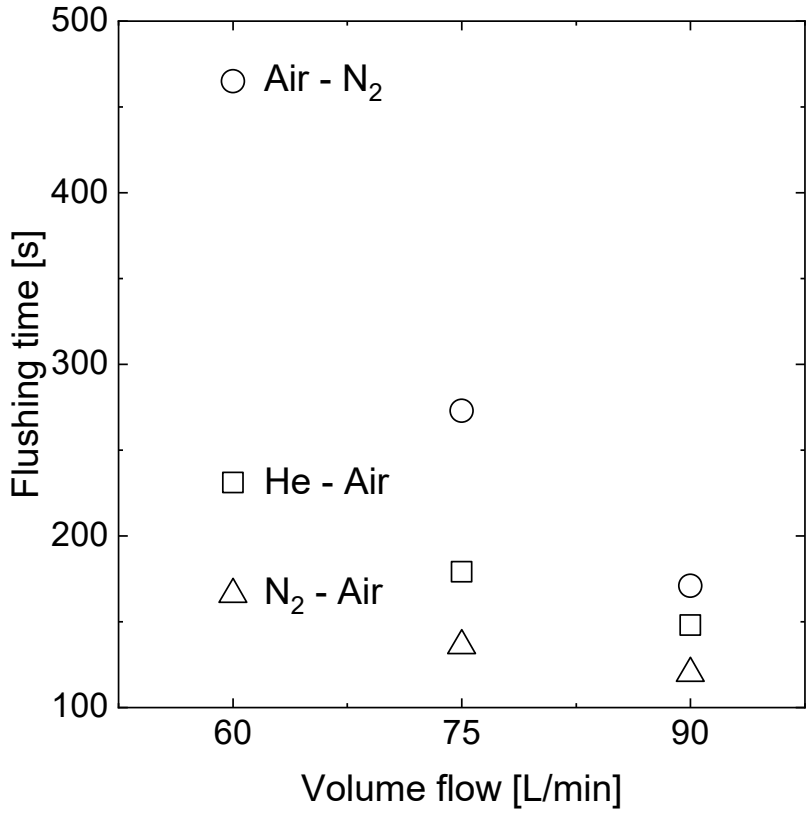

Figure 6.11.: Flushing times for different volume flows and gas combinations using the top outlet.

Flushing Times

Finally, the flushing times are estimated. According to Figure 6.5, the flushing time in the change from H_2 to O_2 mode consists of two steps: The flushing of the helium-filled gas compartment and then the filling with oxygen. However, in the change from O_2 to H_2 mode, only the flushing of the oxygen-filled compartment with nitrogen is required. Figure 6.12 summarizes the

flushing times between oxygen and nitrogen for different outlets, and gas exchanges in combination with helium as substitute for hydrogen.

The target is to achieve the shortest possible flushing time. Therefore, the bottom outlet with 194 s in the O_2-N_2 combination is selected for the O_2-H_2 mode change.

A flushing time of 181 s is used for the first step of the H_2-O_2 mode change, originating from the He-N_2 combination with the top outlet. The He-Air combination in Figure 6.12 would extend the flushing time. For the second step, the time of the N_2-O_2 combination using the top outlet is used (184 s).

In summary, a flushing time of **194 s** can be determined for the O_2-H_2 mode change and a flushing time of **365 s** for the H_2-O_2 mode change. However, the results are a first approximation. Faster flushing can be expected at higher volume flow rates and by displacing oxygen with argon instead of nitrogen.

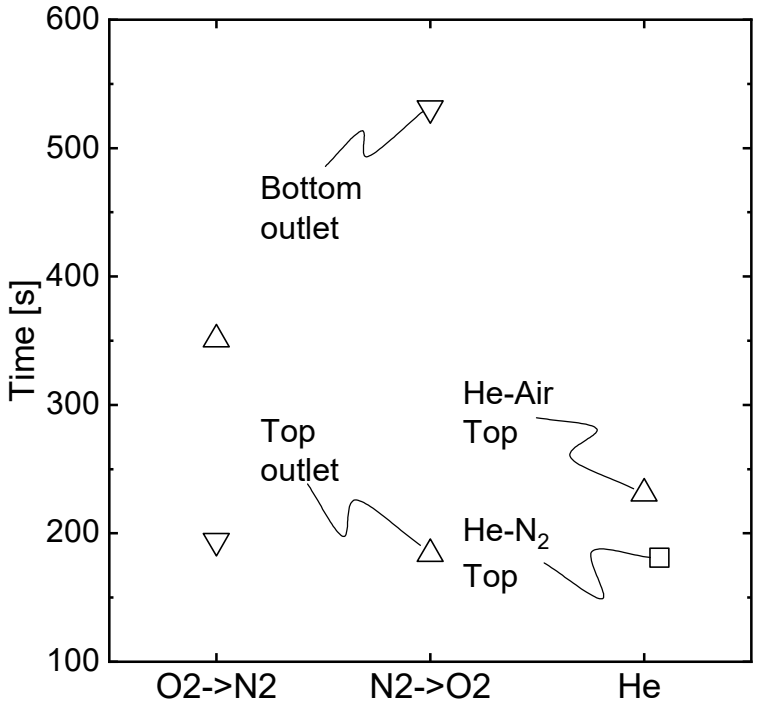

Figure 6.12.: Flushing times from O_2 to H_2 mode, from H_2 to O_2 mode including oxygen filling, and for He-Ar changes.

6.4. Conclusion

In this chapter, the correlation between gas density and concentration distribution discovered in previous CFD simulations was validated by experimental investigations on a commercial industry-sized cell. Visualization experiments employing fog unraveled dead zones and maldistributions in the gas compartment of the industry cell. The fog experiments confirmed those assumptions. Following these results, a second outlet was implemented at the cell bottom in addition to the top outlet to utilize the density differences. On the other hand, using both outlets was not proven beneficial. Still, the fog experiments showed remaining dead zones and fog accumulations. Cell design adaptations should further reduce those potential dead zones to facilitate a secure and complete gas exchange.

Concentration measurements extended the visualization experiments to assess actual flushing times. The switching processes O_2-H_2 and H_2-O_2 modes were investigated. The O_2-H_2 mode change only demands flushing of the oxygen-containing gas compartment with an inert gas. In that case, the flushing time was determined to 194 s using the bottom outlet. Comparing the top outlet, a flushing repetition of oxygen with argon achieved a flushing time reduction by 73 %. In general, it was observed that the flushing process of a denser gas flushed by a lighter gas takes significantly longer due to the agglomeration of the denser gas in the bottom left corner of the compartment. Consequently, the agglomerate dissolves very slowly, resulting in inefficient and prolonged flushing. In the H_2-O_2 mode change, first hydrogen (in this case helium) needs to be replaced by an inert gas. Afterward, oxygen filling must be carried out to ensure the oxygen reduction reaction. The two-step process sums up to 365 s (He-N_2-O_2 sequence). Large deviations were noted when comparing the determined flushing times with CFD simulations from Chapter 5. The experimentally obtained flushing times of 194 s and 365 s, are much smaller than the simulated 2200 s. The reason for the large deviations might originate from the sampling location: In the experiments, flushing time is determined at the outlet or the sampling

point oxy2 on the left, while the flushing time is obtained more accurately from the minimum mass fraction in the CFD simulations.

From the concentration and fog experiments, the following can be summarized for a residue-free gas exchange:

- If the gas compartment is filled with heavier gas, the top outlet should be used,
- If the compartment is filled with lighter gas, the bottom outlet should be used.

Further flushing time reductions can derive from higher volume flows or improved flow distribution. Therefore, geometry adaptations of the gas-compartment internals are conceivable. Cell-design adaptations are discussed in the following chapter.

7. Cell Design Optimization of a Flexibly Used Industry Cell

7.1. Introduction

In Chapter 5, fluid flow simulations have been extended with models describing mass transfer to assess the concentration distribution and its effect on the flushing process. It was found that the original cell design of commercial CAE cells creates regions of low velocities that impede mass transfer (in that case, low N_2 mass fraction), which was experimentally confirmed in Chapter 6. Since the duration and efficiency of the flushing process are of great importance, the best suitable cell design should be selected for this purpose. So far, commercial industry cells are unsuitable for fast, residue-free gas exchange. Cell design modifications can help accelerate the flushing procedure.

CFD simulations are a suitable tool to screen cell design modifications quickly and cost-effectively. However, manually modifying the cell design and building the simulation model without automated geometry variation is highly time-consuming and, therefore, impractical for optimization purposes, which demand a large number of data sets. The Bayesian Optimization algorithm has demonstrated good applicability in CFD-related optimization [Bega2023] and is therefore used in this chapter to optimize the electrolysis cell geometry. The Bayesian Optimization allows finding the extrema of expensive-to-evaluate functions, like a CFD simulation with a high mesh resolution.

In this chapter, the optimization of the cell design is discussed based on CFD simulations of varied cell designs, an algorithm-based computer-aided optimization and experiments in a prototype cell. First, technically feasible geometry changes and freely selectable geometries are tested using CFD simulations. The geometry adaptations of the internals are designed based on the dead zones found in Chapters 5 and 6. Possible correlations between flow deflection due to the internals, the resulting concentration distribution and, eventually, flushing times are investigated. The flushing times of the geometry adaptations are compared to the original cell design.

Second, optimization methods are used to find a suitable geometry to minimize the flushing time, in this case, the Bayesian Optimization algorithm.

For this purpose, CFD simulations with built-in, variable geometry internals and boundary conditions of the gas flow are integrated into COMSOL Multiphysics and optimized via Bayesian Optimization (see Chapter 2.3.3 for more details).

Finally, a downscaled prototype cell is assessed in a parallel approach to the previously mentioned CFD-based Bayesian Optimization. Based on the simulations and industry-cell experiments, the flushing process is carried out and evaluated in the optimized prototype cell designs. CFD simulations are used for the initial evaluation and preselection of designed geometries. Subsequently, the selected geometries are implemented into the prototype cell and examined via concentration and fog experiments as presented in Chapter 6. Further configuration of the prototype cell with movable internals allows an in-situ modification of the internals and visualization of the flow behavior. Lastly, an optimized cell design is derived and discussed.

7.2. Simulative Optimization

7.2.1. Manual CFD Simulations Based on Flow and Concentration Distribution

This work aims to further develop the geometry of a typical industry cell in terms of uniform flow and rapid gas exchange. Therefore, different internals and geometries are investigated based on the literature discussed in Chapter 2.3. For simple geometry optimization purposes, 19 bars were implemented as internals to generate a channel quantity of 20. The number of inlets was varied to influence the flow through the channels created by the supporting bars. In this context, the number of inlets was set to one, two, four, ten and twenty (see Figure 7.1 a)-d)).

As further geometry adaptation, triangular baffle elements (Figure 7.1 e), a horizontal arrangement of the default bars (Figure 7.1 f) and the default arrangement with uniformly distributed holes in the bars (perforated bars, (Figure 7.1 g) were implemented.

Simulations of the default geometry in Chapter 5 have shown that the

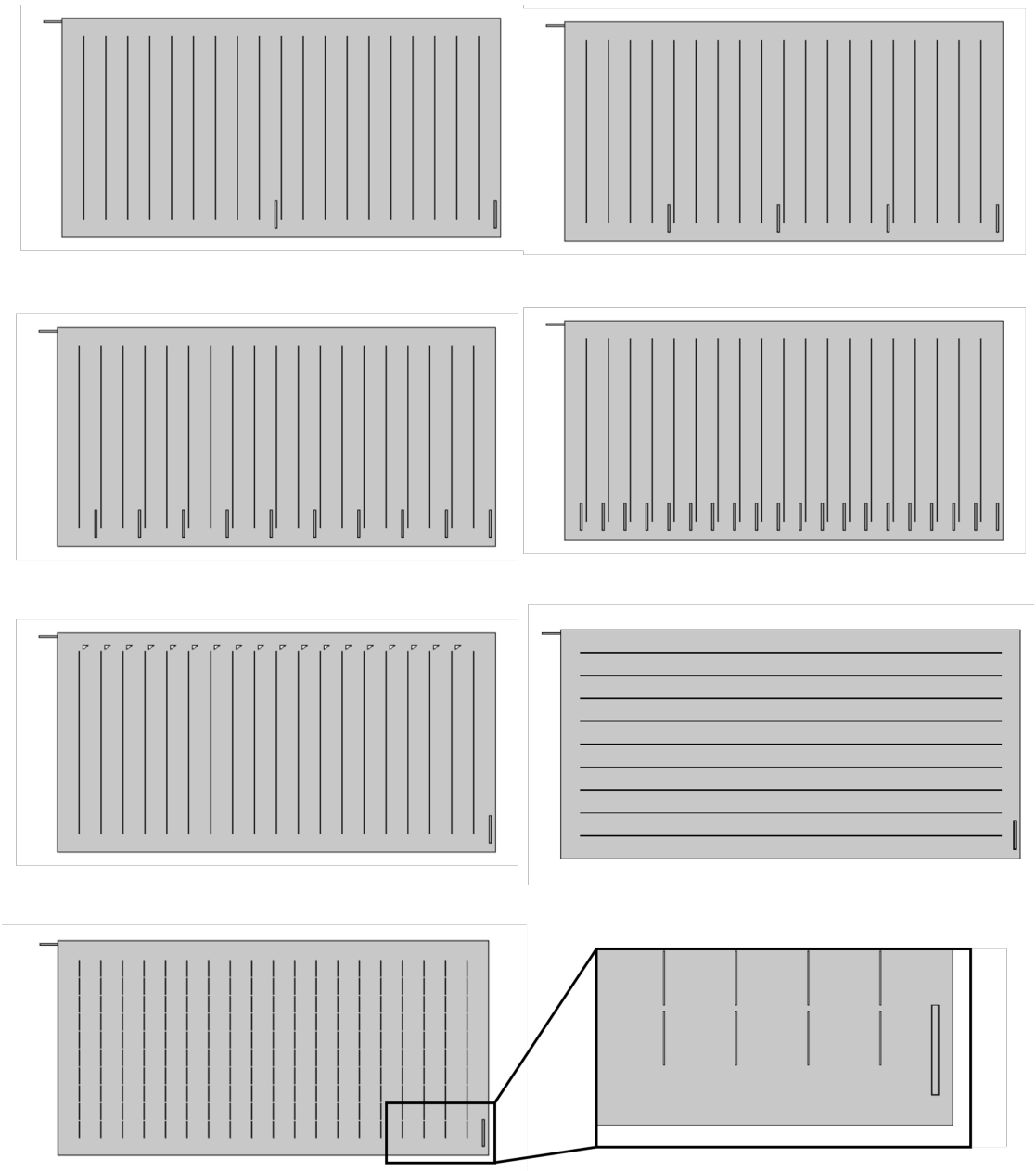

Figure 7.1.: Geometry variations with a) two inlets, b) four inlets, c) ten inlets, d) twenty inlets, e) baffles, f) a horizontal arrangement, and g) perforated bars.

current design causes an inhomogeneous flow distribution and hinders fast gas exchange. Thus, in the following, suggestions for geometry adaptations and their effect on mass transfer are discussed. The subsequent simulations were conducted using the $\kappa - \epsilon$ model. The simulations are implemented according to the boundary conditions in Chapter 5.2.2. In the case of several inlets, the total volume flow is kept constant and distributed evenly on the

inlets.

7.2.2. Algorithm-Supported Optimization Simulations

Beyond the previously presented geometries derived from an engineering perspective, the next step was systematically examining geometry modifications using an optimization algorithm. The optimization algorithm changes the geometry and analyzes the results of its changes before trying a new geometry. To optimize the geometry of the CAE cell, the Bayesian Optimization algorithm was used to find the extrema of expensive-to-evaluate functions, like the here-implemented CFD simulation with a high mesh resolution. Objective functions are chosen based on the physical problem and treated as black-box functions by the algorithm. Gaussian process Regression aims to generate predictions for suitable new inputs, updating the data set with each iteration. Detailed information can be found in Chapter 2.3.3.

Adding and removing geometry adaptations were considered as possible inputs. On the contrary, a low simulative effort can be related to shifting or rotating the interior bars, varying their distance or implementing perforations. A higher simulative action comes with additional items, such as more inlets, baffles or entirely new structures, such as a meander (see Chapter 7.2.1).

A compromise between simulative and constructive effort is the bar angle and bar distance variation as inputs for the Bayesian Optimization algorithm. Figure 7.2 shows the principle of different bar distances (’shift’) and changing the bar angle (’angle’). The bar angle was limited to -89 ° and 90 °. The bar shift was generated by varying the distance while the center bars remained fixed, and the outer bars were prohibited from colliding with the walls. Therefore, the bar shift is allowed between 0 mm to 5 mm. Combining bar shift and bar angle leads to a changing amount of bars.

The expensive-to-evaluate CFD simulations with variable geometry internals were implemented into COMSOL Multiphysics. Physical correlations, boundary conditions and simulation settings were implemented according to Chapter 5.2. An unstructured mesh with a minimum of 280,000 elements was used due to its applicability to various geometries. A Matlab-LiveLink

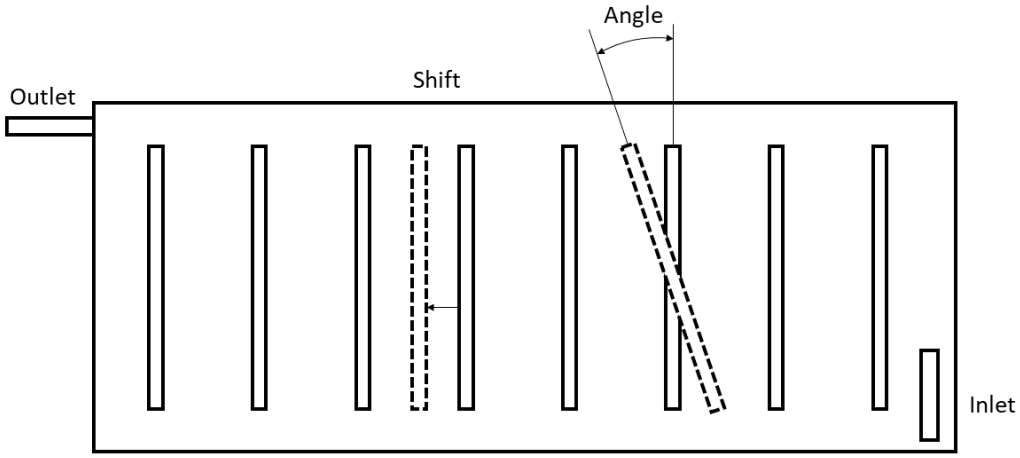

Figure 7.2.: 'Bar shift' and 'bar angle' as inputs for the Bayesian Optimization algorithm.

automatically ran loops of CFD simulations. Compared to Chapter 5.2, an additional evaluation script was added to the COMSOL code to evaluate previously selected objective functions. Objective functions were defined to optimize the flow distribution and, consequently, to deduce a better concentration distribution.

7

Objectives

Objective functions were previously chosen, focusing on velocity, concentration and their distributions. Matlab minimizes the objectives using the simulation data extracted from COMSOL. Pre-simulations showed the influence of gas entrapment (*blocked channel*), vortex formation (*vorticity fraction*, VF) and flow velocity (*volume flow*) on the gas exchange. Therefore, these parameters were chosen as objectives and are described in the following.

Blocked Channels To evaluate *blocked channels*, the concentration distribution in the gas compartment is evaluated. A detectable circulating flow is

characteristic of vortices. They form especially in the top or bottom sections of the vertical channels due to the perpendicular flow direction. Vortices can take up most of the channel width with little space for vertical fluid exchange. For two different input parameter sets, the concentration distribution is evaluated after 4 min. A flow channel is blocked, if:

- A vortex forms at each of the top and bottom parts of a channel,
- Both vortices exceed a vorticity strength of $VF = 0.3$ (see Eq. 7.1),
- The volume flow inside the channel is below the domain-averaged volume flow.

The objective function *blocked channel* is calculated with the average vorticity fraction of all vortices inside the channel and the net volume flow through the channel. The vorticity fraction VF is a tuning parameter to neglect small vortices and is specified by the ratio of fluid moving out of the vortex and fluid remaining inside the circular vortex flow (see Equation 7.1). The net volume flow represents the amount of fluid moving out of the vortex. It is calculated via the integral of the velocity over the channel cross-section. The total volume flow describes all fluid that moves inside the cross-section (the sum of the net volume flow and the fluid that does not leave the vortex). A sign change in the flow direction characterizes a vortex. The total volume flow is the integral of the absolute value of the velocity over the cross-section; in this 2D case, over the cross-sectional line. Based on preliminary manual simulations, the VF threshold for blocked channels was set to 0.3. Values below 0.3 are not considered as a vortex.

$$VF = 1 - \frac{net\ volume\ flow}{total\ volume\ flow} = 1 - \frac{|\int v^* \mathrm{d}L|}{\int |v^*| \mathrm{d}L} \tag{7.1}$$
$$\text{with} \quad v^* = v_x * \sin(\alpha) + v_y * \cos(\alpha)$$

Finally, the objective function *blocked channel* is the sum of the vorticity fractions of all vortices in the channel (discrete character) and the net volume flow through the channel (continuous character). The calculation algorithm is shown in Table 7.1. The Bayesian Optimization algorithm aimed to minimize the objective *blocked channel* generated from the procedure in Table 7.1.

Table 7.1.: Calculation of the objective *blocked channel*

```
1  Blocked Channel = 0
2  for each channel
3  |  if vortices on both ends of the channel > 0.3 then
4  |  |  Blocked Channel = VF_avg + V̇_avg/(V̇_Channel * 100)
   |  |                              +Blocked Channel
6  |  end if
7  end for
```

Volume Flow The objective *volume flow* is calculated via the average of all net volume flows through all channels. As it is desired to maximize the net volume flow for a fast species exchange, the measure is inversed for the minimization function of the Bayesian algorithm:

$$\frac{1}{\dot{V}} = \frac{1}{|\int v^* \mathrm{d}L|} \qquad \text{with} \quad v^* = v_x * \sin(\alpha) + v_y * \cos(\alpha) \tag{7.2}$$

In the optimization algorithm, the *volume flow* is either considered as the inverse of the average volume flow over all channels $1/\dot{V}_{avg}$ or as the inverse of the smallest volume of all channels $1/\dot{V}_{min}$.

Vorticity Fraction Besides the integration in the objective function *blocked channel*, the *volume fraction* is also considered a separate objective function. This objective either indicates the maximum vorticity fraction VF_{max} of the whole domain or is averaged across the entire domain as VF_{avg}.

Objective Sets

The introduced objectives are collected in three objective sets, which are optimized by the Bayesian Optimization algorithm. The objective sets are summarized in Table 7.2. The *volume flow* (see Equation 7.2) is either considered as inverse of the average volume flow over all channels $1/\dot{V}_{avg}$ or as inverse of the smallest volume of all channels $1/\dot{V}_{min}$. The *vorticity*

fraction (see Equation 7.1) is either considered as average vorticity fraction in all channels VF_{avg} or as strongest vortex VF_{max} in the channels. The value for *blocked channel* is calculated with the algorithm pictured in Table 7.1.

In the results section, the individual objectives from each objective set are denoted by their set and number, for example, the objective 'average vorticity fraction' from objective set B is called B2.

Table 7.2.: Objective sets with their objectives

Objective set	A	B	C
# 1	$1/\dot{V}_{avg}$	$1/\dot{V}_{avg}$	$1/\dot{V}_{min}$
# 2	*Blocked Channel*	VF_{avg}	VF_{max}
# 3		VF_{max}	

Analysis

The Bayesian Optimization was carried out using Matlab. First, a Matlab code extracted the velocity data from COMSOL from the vertices of the mesh elements. Then, the measurement points were fitted with equidistant evaluation lines in Matlab to evaluate the individual objectives. The evaluation lines were implemented orthogonal to the flow direction inside the channels covering the whole channel width. Figure 7.3 shows such an orthogonal evaluation line between two bars. An example of a vertex resulting from the COMSOL meshing is marked. Each evaluation line was approximated with 200 points. The vertices closest to the data points on the evaluation line were considered. They were projected onto the evaluation line via the interpolation method *trapz* in Matlab. Finally, the projected data points were used to further calculate the objectives in Matlab.

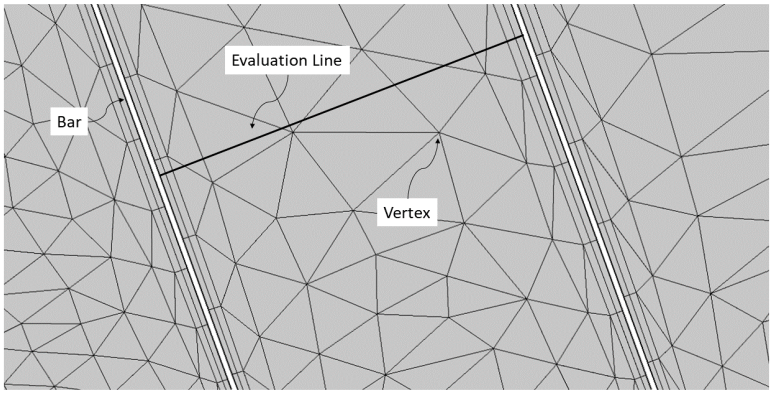

Figure 7.3.: Evaluation line between two bars placed on the COMSOL mesh.

7.3. Prototype Cell

7.3.1. Prototype Cell Design

The most promising geometries of the previously conducted simulations were tested experimentally with a prototype cell. The prototype cell was constructed using a similarity-theory-based downscaling of the industrial cell. Only the gas compartment was targeted, similar to Chapters 5 and 6. The width-to-length ratio was, therefore, kept the same as in the industry cell. The scaling factor between the prototype and industrial cell was calculated regarding the surface area ratio $A_{proto}/A_{ind} = 0.0314$. With this scaling factor, all components of the prototype cell were downscaled from the industrial cell. The cell volume resulted in 0.4 dm^3.

An exploded view of the prototype cell is shown in Figure 7.4. The cell consists of two poly(methyl methacrylate) (PMMA) panes, a nickel-plated metal sheet and five plastic frame parts. A metal sheet allows the bars to be variably attached and positioned within the cell via small magnets. In the further development of the prototype cell, the metal sheet was replaced by a polyurethane (PU) plate with through holes. The through holes were equipped with 3D-printed, rotatable elements, which could be turned during the experiment. Dividing the plastic frame into individual elements was due to manufacturing reasons. It also ensured that the frame parts could be

easily replaced. The inlet was designed to be as wide as possible to allow the fog to enter, which deviated from the industrial cell. For this purpose, one short frame part was separated, generating a 3 mm wide slit as the inlet. The cell outlet was built the same way with a 3 mm outlet slit to reduce the flow resistance further. The large openings avoided the accumulation of the gas flow and, thus, back pressure inside the gas compartment. The distances of the inlet and outlet to the cell's inner frame could not be reduced to scale but had to be increased to a more feasible distance of 4 cm. Finally, a 3 mm wide O-ring made of NBR was implemented to guarantee tightness between the upper PMMA pane and the frame parts. The selection and implementation of the bars and other interiors are discussed in the following section.

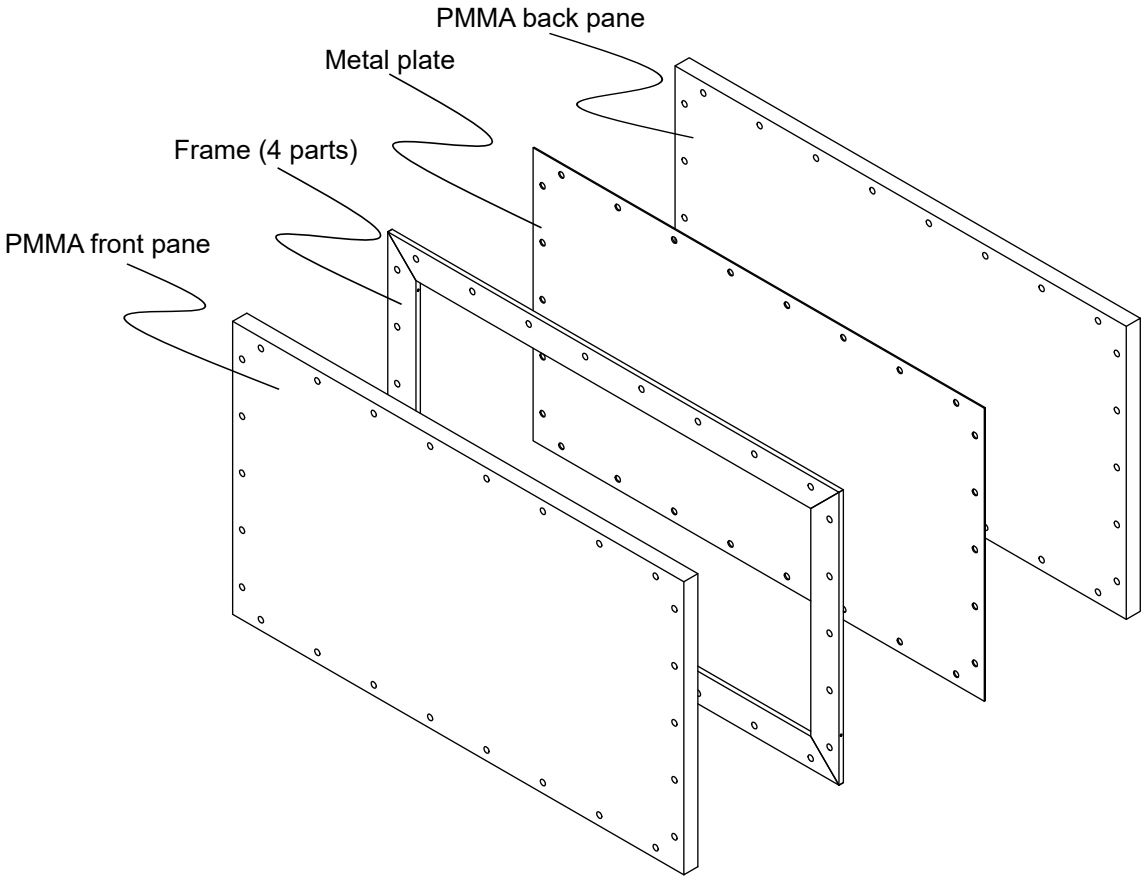

Figure 7.4.: Exploded view of the prototype cell with two PMMA panes in the back and at the front, a frame consisting of four parts, and a metal plate.

The key factors, residence time, Reynolds number, and pressure drop

(via the Darcy-Weisbach formula), were used to scale the industrial cell to the smaller prototype size. The residence time indicates the required time to fill a particular volume under certain boundary conditions. Thus, assuming ideal mixing, the residence time means the average time a gas molecule remains in the cell volume. An equivalent residence time was considered to determine the volume flow rate for the prototype cell. The hydraulic diameter in the cell interior was used as the characteristic length to calculate and compare Reynolds numbers. The hydraulic diameter is assumed rectangular with the width and height of the first channel (27.45 mm x 4.7 mm). The third parameter, the pressure drop of the cell, is calculated for pipes with flow using the Darcy-Weisbach formula (see Equation 7.3). Although the flow and, thus, the pressure loss of the cell considered here are not directly comparable with that of a pipe, the most important influencing variables can be identified using the formula. These include the flow velocity u, a friction term (in the case of pipe flow, the pipe friction coefficient λ), a pressure loss term (consisting of the pressure loss coefficients ζ_i), and two geometric quantities (in the case of pipe flow, the internal diameter d and the length of the pipe l). As a result of the consideration of fluid flow with the simultaneous variation of the cell interior, none of the influencing variables listed to determine the pressure drop can be assumed constant. Instead, all parameters influence the resulting pressure difference between the inlet and outlet of the cell and can be determined solely by experiment. Finally, the two parameters, 'flushing time' and 'efficiency factor', discussed in Chapters 5 and 6, were evaluated.

$$\Delta p = \frac{\rho \cdot u^2}{2} \cdot (\lambda \cdot \frac{l}{d} + \Sigma \zeta_i) \tag{7.3}$$

7.3.2. Prototype Cell Geometries

Such elements were considered, which are simple and, at the same time, enable different geometry designs with little adaption. The vertical bars of the **original** industrial cell serve as the reference geometry (see Figure 7.5 a).

For the selection of new geometries, variations based on designs known from other electrochemical cells, such as fuel cells, preferably cells used with gas flow.

The internals were 3D-printed using rapid prototyping (Objet Eden 260V, Stratasys, Eden Prairie USA; material VeroClear (RGD810)). The bars were designed with the same cross-section as the reference geometry but with a broad base to glue circular magnets with a diameter of 1 mm into cutouts at the bar bottoms. The magnets allowed the bars to be attached to the metal plate and still be moved (e.g., rotated or shifted) for geometry variation. Other internals than bars were also 3D printed and equipped with magnets. The selected geometries are discussed in the following.

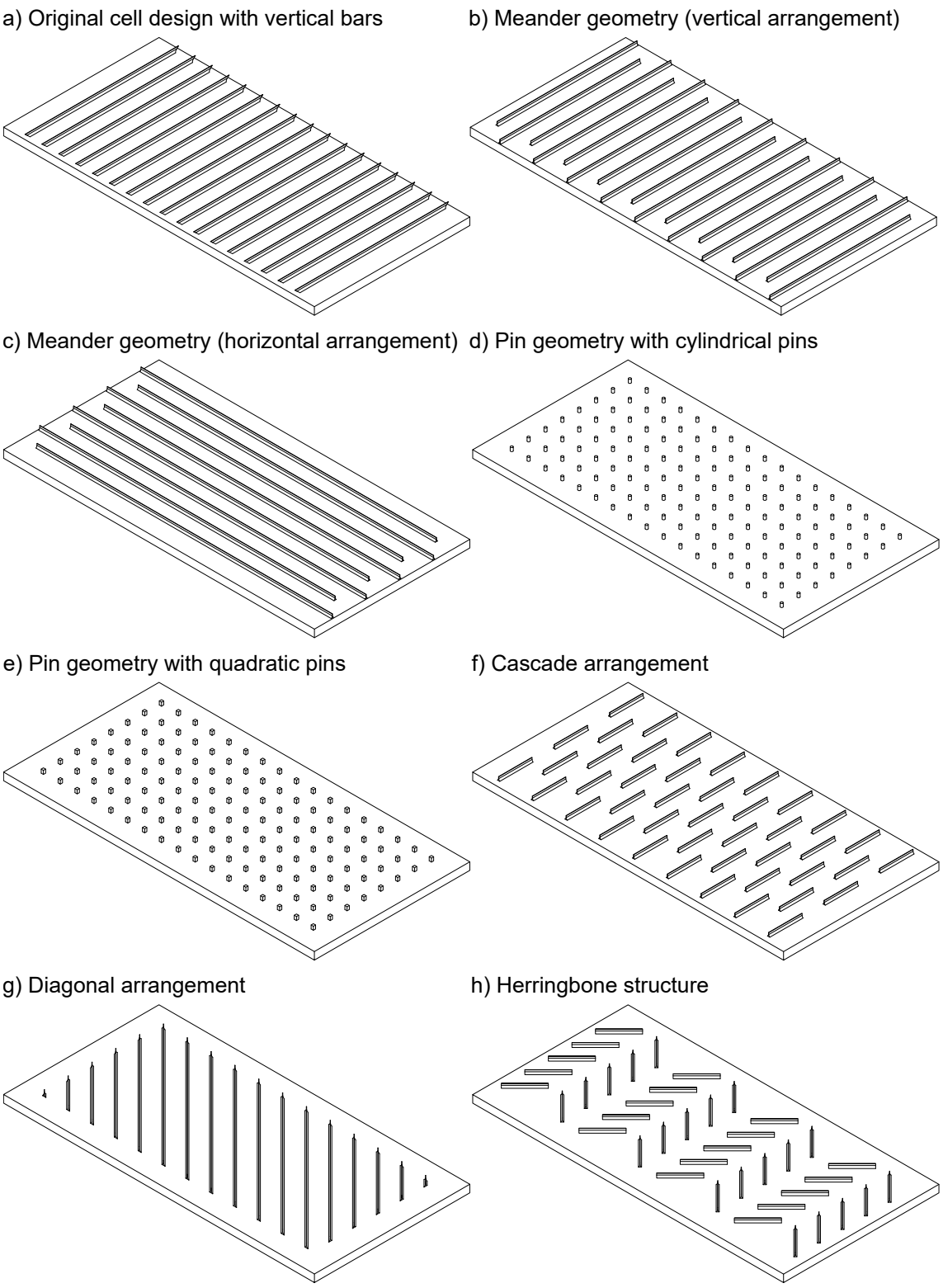

Figure 7.5.: Cell geometry variation for simulation-based preselection to be implemented in the prototype experiments.

The meander is an arrangement frequently used in electrolysis and fuel

cells. In this configuration, the bars are arranged so that the gas can only flow through the cell along one continuous path (see Figure 7.5 b). However, to avoid possible accumulations of particularly light (H_2) or heavy gas (O_2) in corners and dead zones in this application, the bars are designed with a minimum distance to the wall. The advantages of the meander-shaped arrangement are the increased average flow velocity and good flow homogeneity. The disadvantage is the high pressure loss [Mans2012]. Here, the meander is implemented as an arrangement vertical to the inlet direction (referred to as **meander**, Figure 7.5 b) and as an arrangement horizontal to the inlet direction (referred to as **meander transverse**, Figure 7.5 c).

The geometry arrangement **pin** describes **cylindrical** (Figure 7.5 d) or **cuboid** elements (Figure 7.5 e), which are positioned in a rectangular pattern with regular distances from each other. This arrangement has many flow channels, both in vertical and horizontal directions. The low pressure loss is a particular advantage when the gases flow through the void volume. However, this can be a disadvantage if an inhomogeneous flow distribution forms due to regions of lower flow resistance on the shortest path to the outlet [Li2005]. This, in turn, can lead to areas of poor mixing and, thus, dead zones [Skrz2021].

The **cascade** geometry consists of a large number of rectangular steps arranged at regular intervals from one another (see Figure 7.5 f). The basic idea of this arrangement is that the gas flow splits into two partial flows when hitting the surface of such a rectangle. This splitting is repeated when the partial flow hits the next rectangle when moving from the inlet to the outlet, so a cascade-like flow pattern eventually results. The disadvantage of this arrangement is the high pressure loss [Mans2012].

A geometry already optimized by the Bayesian algorithm with diagonal bars is referred to as **diagonal** in the following (see Figure 7.5 g). The simulative investigations are discussed in Chapter 7.4.2 and were chosen to be tested due to their great potential for a homogeneous flow and velocity distribution [Rosh2012].

Further development of this diagonal geometry with alternating angles appears like the **herringbone** structure from the literature (Figure 7.5 h). In

this geometry, the bars are arranged in a herringbone pattern. Herringbones are common as liquid mixers [Wies2018].

7.3.3. CFD Simulations for Geometry Preselection

In terms of geometric degrees of freedom, the prototype cell is somewhere between the rigid industrial cell and CFD simulations with unlimited design flexibility. Therefore, a preselection of possible geometries based on 2D CFD models discussed in Chapters 5 was performed prior to the prototype experiments.

The gas exchange was implemented at a constant gas density to keep the computational effort low, and only the comparison among the geometries was considered. The preliminary CFD simulations modeled the flushing of an O_2-filled volume with nitrogen (N_2) using the $\kappa - \epsilon$ turbulence model. The CFD simulations were used to pre-select cell design to be tested in experiments with the prototype cell. While for the geometries so far, the inflow was implemented vertically, a horizontal inflow was chosen for the geometries 'meander transverse' (Figure 7.5 c) and 'cascade' (Figure 7.5 f) to avoid disadvantages due to the inflow behavior. The time-dependent simulation considered the first 280 s of the gas exchange for all geometries. Consequently, the velocity and concentration distributions of the flow field and the pressure difference between the cell inlet and outlet were compared between the different cell geometries.

To determine the incoming volume flow rate, the equivalence of the Reynolds number at the inlet and the equivalence of the residence time were considered in a similarity analysis between the industry and the prototype cell. A small inlet diameter would be required to match the equivalent Reynolds number of $Re = 5189$ from the industry cell. The inlet diameter would result in order of magnitude that could not be manufactured. Instead, the equivalence of residence times was considered. In that case, the volume flow rate entering the cell was converted by the volumetric scaling factor 0.006. This results in a volume flow rate of 0.33 L min^{-1}, which was set as

the default value in all simulations and experiments with the prototype cell. In that case, a Reynolds number of $Re = 21$ results. The CFD simulations to determine pressure differences were performed with a higher volume flow of $4\,\mathrm{L\,min^{-1}}$ to enable detectable pressure differences.

The preselection of the geometries was evaluated in a structured manner through a utility analysis based on five different criteria: flushing time, homogeneity of the flow (concentration differences), the pressure difference between inlet and outlet, arrangement effort of the bar geometries (number of internals to be installed), and active cell area covered by the bar surfaces. The homogeneity of the flow was evaluated via the percentage difference between the maximum concentration of remaining O_2 in the cell and the O_2 concentration at the outlet. The *flushing time* was chosen as the key parameter in this work. *Flow homogeneity* was selected as the second most important parameter due to its importance for a highly efficient flushing operation. The *pressure difference* was the third important parameter since it can be used to estimate the pumping energy required to operate the cell. The fourth parameter was the *arrangement effort*, which is evaluated based on the number of physical elements. In the last place was the *covered cell area* since, for this parameter, a negative effect on the efficiency of the cell operation can only be assumed.

7.3.4. Experimental Setup

Figure 7.6 shows the flow chart for the prototype experiments, including the gas supply via lab-intern pipelines, a mass flow controller (MFC), two pressure indicators (PI), three O_2 sensors (oxy1, oxy2, oxy3), and the optional glass pipe and fog generator.

As in Chapter 6, concentration measurements with N_2-O_2 mixtures were performed in the prototype cell to evaluate the flushing time. Again, Pyroscience O_2 sensors were used (OXROB 10 sensors, FireSting-PRO FSPRO-4, both Pyroscience, Aachen, GER). The pressure drop between the cell inlet and outlet was measured at a N_2 flow using electronic pressure sensors ('EL-PRESS P-502C', Bronkhorst, Ruurlo, NL). The flow rate was regulated

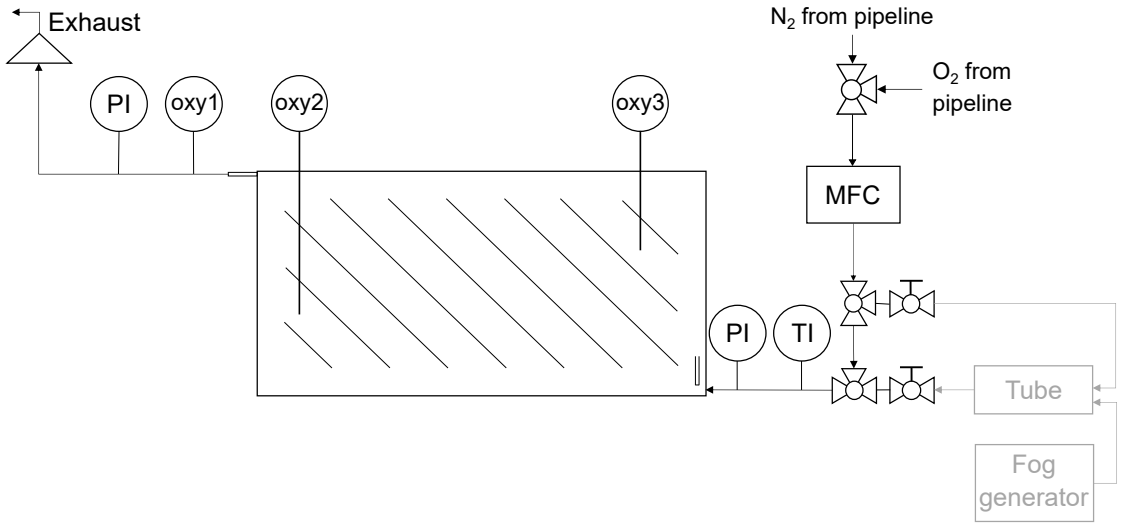

Figure 7.6.: Flow chart for the prototype-cell experiments.

to 4 L min^{-1} instead of 0.33 L min^{-1} (approx. 12 times the original value) to generate measurable pressure differences on this geometric scale. Finally, the data were evaluated with the corresponding software 'Flow Viewer' and 'Flow Plot'.

Similar to Chapter 6, a fog generator was used ('FlowMarker®', Günther Schaidt SAFEX® Chemie GmbH, Berlin, GER) for flow visualization experiments. The FlowMarker® produces a smaller fog volume without an additional, directed volume flow compared to the fog lance in Chapter 6. Therefore, it is a viable alternative for the smaller scale of the prototype cell. The FlowMarker® uses a long-lasting, thermally inactive fog made from a polyol fog fluid that is not harmful to health ('Super Fog' [Günt2011]). To generate the fog, a battery inside the device increases and maintains the operating temperature of a built-in heater. The fog fluid is then passed through the heater. Before leaving the unit, the fog passes through a heat exchanger. Additionally, it mixes with ambient air to obtain a similar density. As the mixture exits the nozzle, it evaporates instantaneously. During the evaporation process, energy gets withdrawn from the ambient, causing the humid air to drop below the dew point and form fine water droplets around the alcohol molecules – the larger the water droplets, the longer the fog lasts [Schu2022]. The advantages of this method are, on the one hand,

the thermal inactivity and low temperature of the fog (ambient temperature) and, on the other hand, the residue-free dissolution in contrast to oil-based methods. The FlowMarker® provides a low-pulse, laminar fog emission, which is advantageous for visualization experiments. Similar to Chapter 6, the generated fog was mixed directly with the N_2 inflow at desired volume flow via a Y-connector.

All flow visualization experiments were recorded with a Nikon 750 D SLR camera placed on a tripod in front of the cell. The background behind the camera was covered with black cloth to avoid reflections of the environment in the PMMA pane (comparable to the experimental setup in Chapter 6). The images captured during the visualization experiments were then quantitatively analyzed using MATLAB. The MATLAB routine first loads the images and automatically renames them uniformly. The user can select a representative sample image, which is used to determine the template for the crop function. In the same step, the threshold values are set, converting all images from 'color' to 'grayscale images'. The grayscale image is then transformed into a so-called 'binary image', distinguished only between 'black' or 'white'. The cell part filled with fog is converted to white; the rest of the cell is assigned black. The black and white fractions indicate the filling level of the cell in percent over time. The influence of the cell thickness is neglected in this consideration, and uniform distribution of the fog front in 2D over the thickness is assumed.

7.4. Results and Discussion

In the following, the results of the manual CFD simulations with alternative geometries, a method-based optimization of the cell geometry, and an experimental evaluation of variably moving internals in a prototype cell are presented.

7.4.1. Optimized Cell Designs Based on Flow and Concentration Distribution

The flushing time is the most crucial target parameter for comparing different cell geometries. This chapter's simulations treat the gas exchange of O_2-N_2. The flushing time is defined as the time needed to reach a mass fraction of 95 % N_2 in the gas compartment. The flushing time can be evaluated for either an average or the global minimum of the N_2 mass fraction. The minimum mass fraction indicates the last spots where O_2 is still present. Table 7.3 summarizes the flushing times of the averaged and the minimum N_2 mass fraction for different inlet quantities. However, it is recommended to consider the minimum N_2 mass fraction to evaluate the actual flushing times using CFD simulations.

Table 7.3.: Flushing times of the different inlet quantities.

Number of inlets	**Flushing time** Average N_2 mass fraction	**Flushing time** Minimum N_2 mass fraction
1	538 s	2200 s
2	713 s	1466 s
4	804 s	1556 s
10	339 s	1467 s
20	157 s	289 s

The results in Table 7.3 do not show a proportional correlation between flushing time and the number of inlets. The geometries with two and four inlets reveal the longest flushing times regarding averaged N_2 mass fractions. Their velocity properties are examined in more detail in the following.

Figure 7.7 shows the velocity fields with streamlines of the gas compartment with two (Figure 7.7 a) and four inlets (Figure 7.7 b). In the case of two inlets, the streamlines indicate that the volume flow in the right half interferes

with the incoming jet from the second inlet and is redirected downwards in the 10th channel. The streamlines suggest that part of the incoming gas remains in the right half. In the case of four inlets, a similar phenomenon occurs. The four inlets split the velocity flow field into four quarters. Again, the incoming jet of the three left inlets hinders the flow from the right via the top flow channel. Instead, fluid flow is redirected in the channels before the 2nd, 3rd and 4th inlet. Some streamlines seem to pass to the neighboring left quarters, which could explain the shorter flushing time compared to the two-inlet geometry.

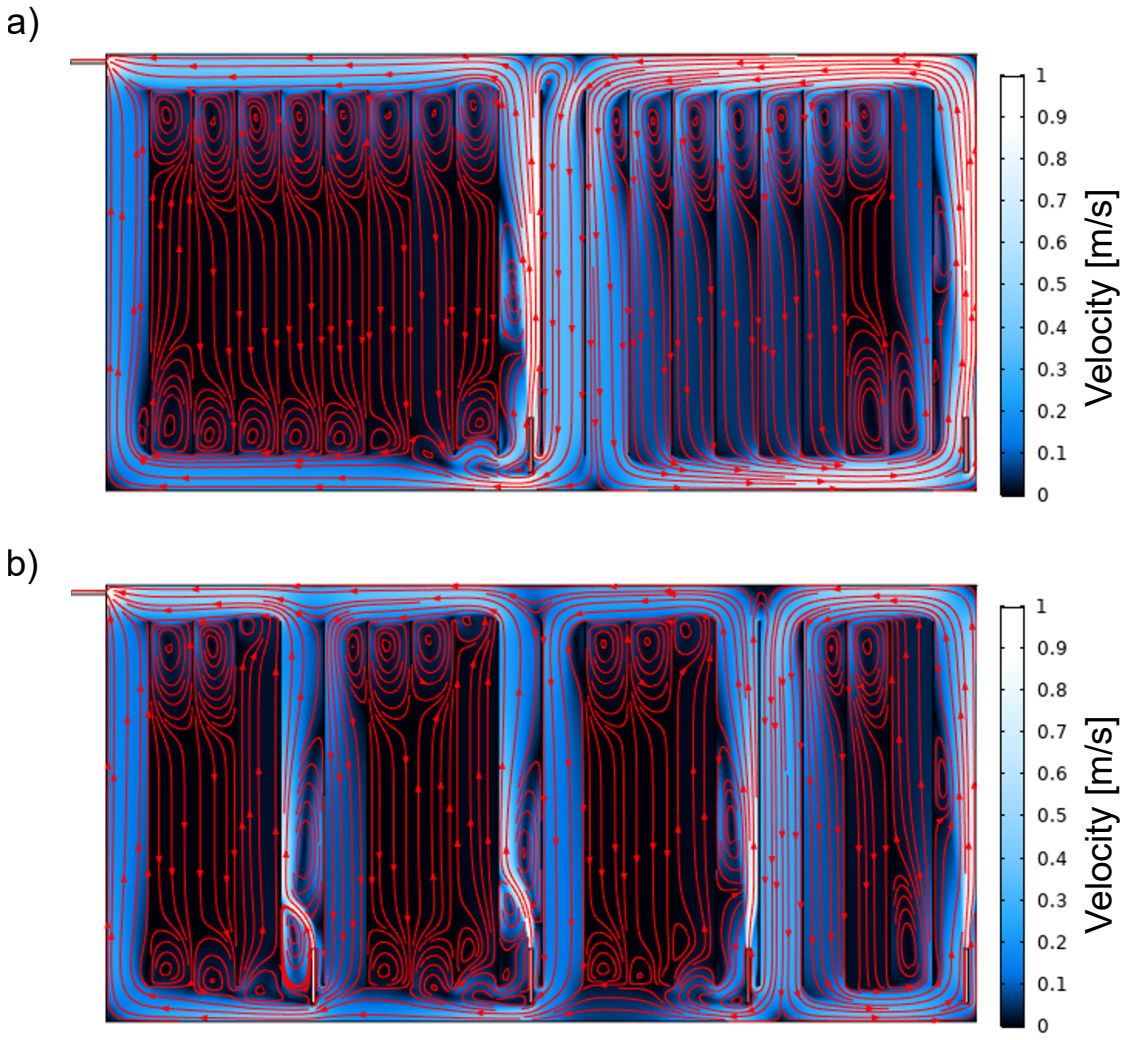

Figure 7.7.: Streamlines for the geometry with a) two inlets, and b) four inlets.

The mass fraction distributions are examined in more detail to investigate the correlation between flushing time, concentration and inlet quantity. Figure 7.8 shows the N_2 distribution at the moment when 95 % of the averaged N_2 mass fraction is acquired. This moment is reached at different times for the various geometries. The incoming volume flow contains $w_{in,N2} = 1$, indicated by white. Areas with a high O_2 mass fraction, referred to as hotspots or stagnant zones, exhibit darker colors (yellow to red). Stagnant zones pose a significant risk since oxyhydrogen formation cannot be excluded here.

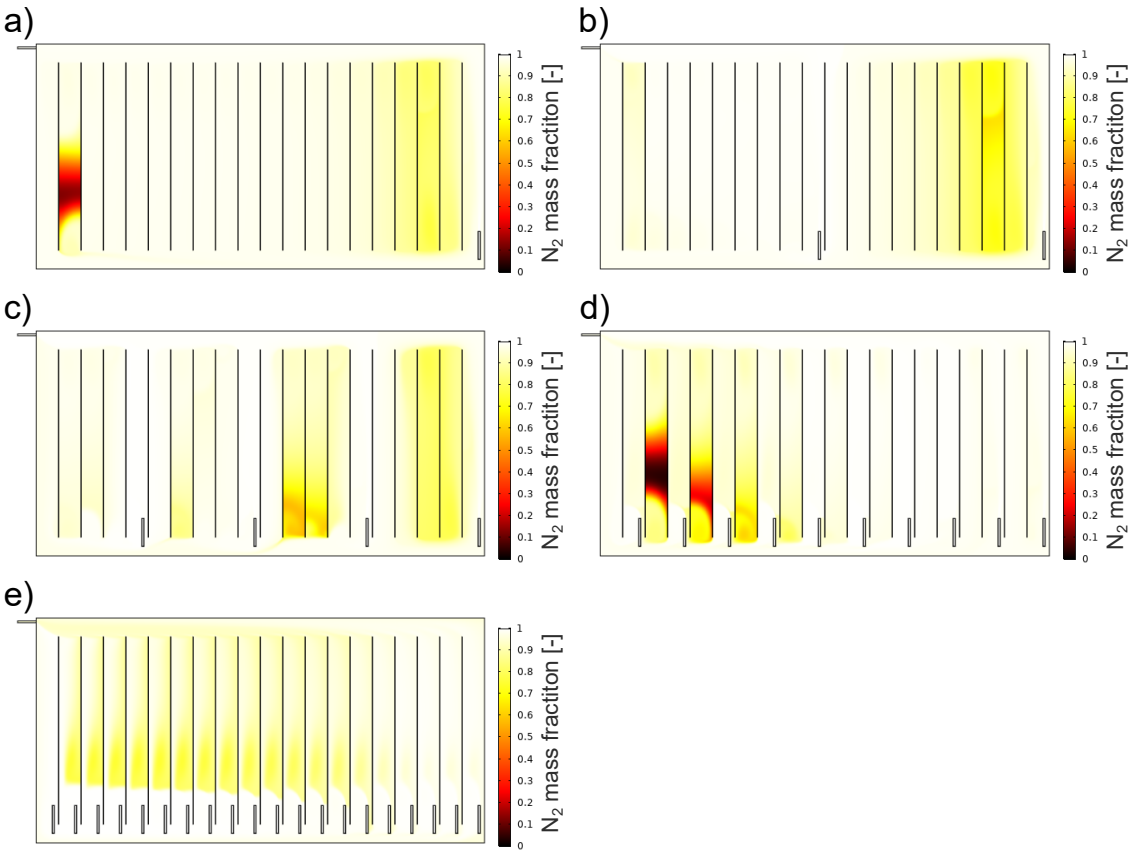

Figure 7.8.: N_2 distribution when 95 % average N_2 mass fraction are reached in a gas compartment with a) one, b) two, c) four, d) 10, and e) twenty inlets.

The geometry with one inlet shows a stagnant zone in the 19th flow channel as well as an area of elevated O_2 concentration in the right compartment half (see the yellow site in Figure 7.8 a). The geometries with two and four inlets also show locations with a higher O_2 mass fraction in the right half

(yellow areas in Figure 7.8 b and c). Those stagnant zones could result from the blockage through the circulating frame flow in the right quarters. The geometry with ten inlets shows stagnant zones in the 18th, 16th and 14th flow channels (Figure 7.8 d). The most homogeneous distribution of N_2 can be achieved with the implementation of twenty inlets (Figure 7.8 e). In Figure 7.8 e, yellow areas are still visible but are not as pronounced as in the other cases. Darker orange or red regions do not occur.

Figure 7.9 shows the course of the minimum mass fraction for different inlet quantities over time. The geometry with twenty inlets shows by far the fastest increase in minimum mass fraction. It is followed by the geometries with two, four and ten inlets. Their courses intersect when reaching the 95 % limit. The default geometry with only one inlet follows at a large offset as the last in the mass fraction progress.

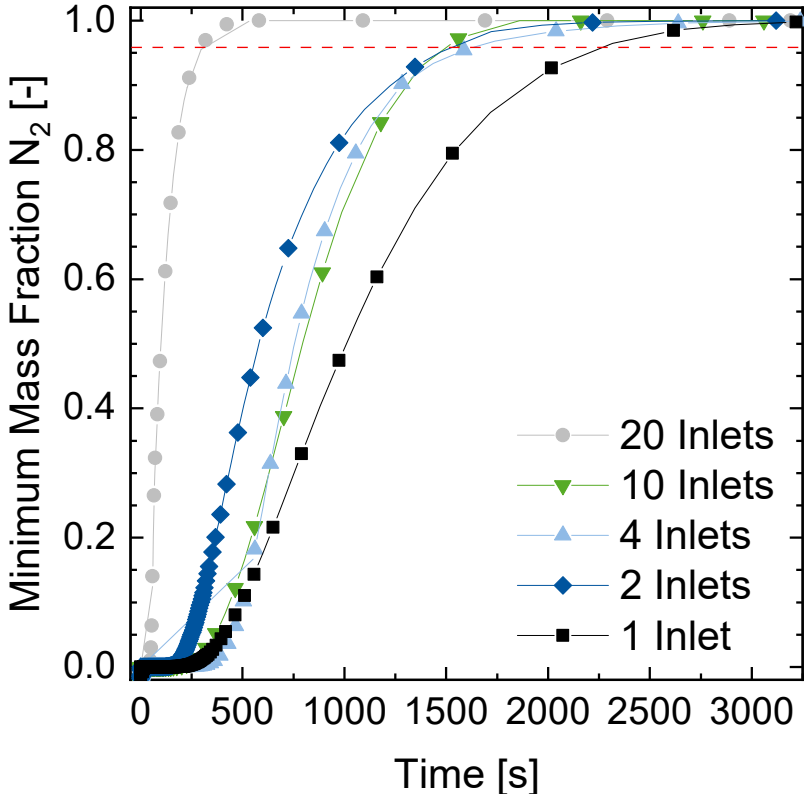

Figure 7.9.: Minimum N_2 mass fraction and resulting flushing time for various inlets.

The resulting flow profiles of the other arbitrary geometry adaptations

presented in Figure 7.1 are shown in Figure 7.10. A facile way to modify the

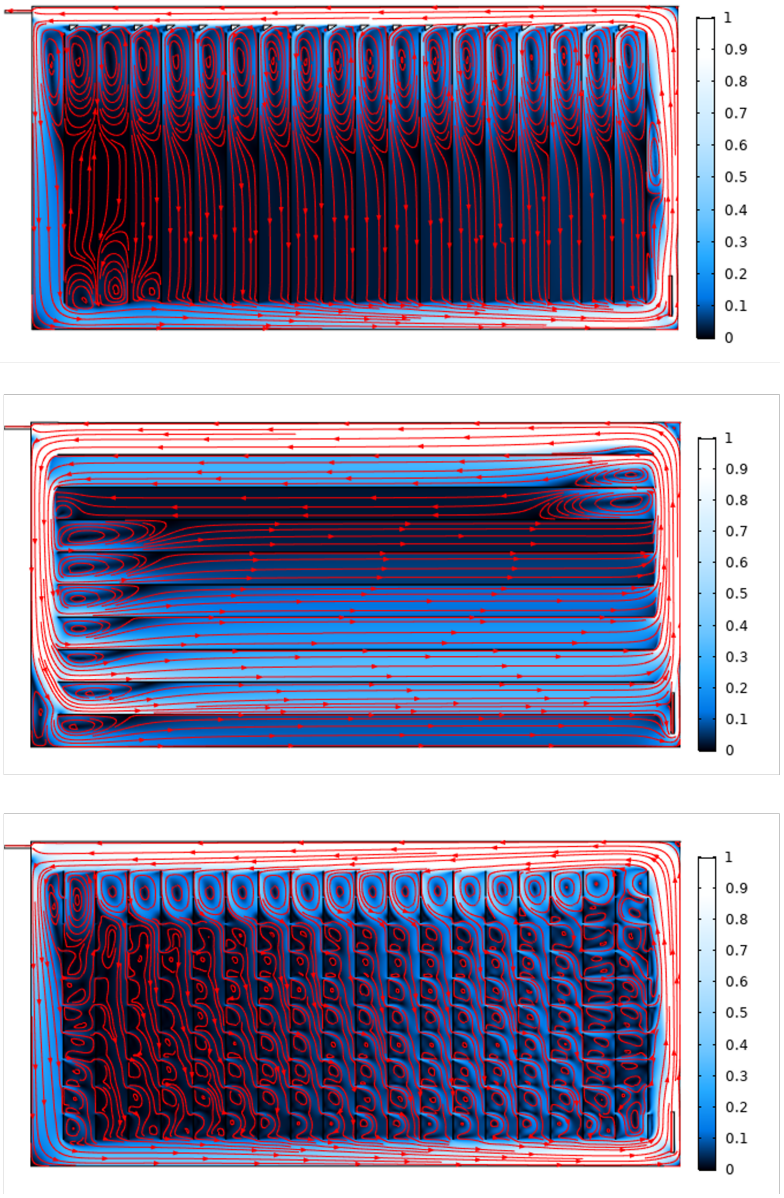

Figure 7.10.: Velocity profiles with streamlines for geometry adaptions: a) triangular baffles, b) horizontal alignment, c) perforated bars.

existing initial geometry is to install **baffle geometries** in each channel inlet. Triangles, as an example, are implemented in the horizontal top channel, directing the volume flow, which enters from the bottom inlet and follows the outer framework (see Figure 7.10 a)). The triangles help to fasten the gas exchange in the center of the individual channels and the gas compartment itself. The resulting flushing time is reduced by 31 % to 1523 s. The installed

components could be further optimized, for example, in size or shape, to enable as little coverage of active area as possible.

Another modification is the **horizontal** instead of the vertical-bar alignment. Therefore, nine bars were placed horizontally inside the gas compartment. The horizontal channels still induce velocity differences in the individual channels, which can be further reduced via an adaptation of the channel amount and distance (see Figure 7.10 b)). The flushing time decreases slightly to 2029 s. As this geometry cannot be easily implemented but requires a cell reconstruction, it is not further investigated.

Perforations of the vertical bars leave additional spaces for the fluid to enter and exchange between adjacent flow channels. Therefore, perforations with a diameter of 1 cm were implemented. Thus, one bar was split into ten shorter bars. However, the perforation of the supporting bars leads to a pressure drop increase of only 0.32 Pa, i.e., 1 % towards the original cell with 35.72 Pa and, thus, is neglected. Figure 7.10 c) illustrates the velocity profile, including streamlines induced by the perforations. A smoother and even velocity distribution compared to the original geometry is achieved. The perforations enable horizontal gas expansion into the adjacent flow channels. This cell design creates a higher average velocity, which results in a flushing time reduction from 2200 s (original geometry) to 777 s. However, as the flow distributors in the gas compartment also serve as stabilization elements for the sODC, it must be evaluated to which extent perforations can be realized.

The flushing times of the baffles, the perforations and the default geometry with twenty inlets are compared to the original geometry in Figure 7.11. The original geometry marks the longest flushing time at 2200 s. It is the benchmark flushing time to be reduced through cell design adaptation. The baffles already result in a 31 % reduction compared to the original geometry, which is further improved when implementing perforations in the vertical bars (65 % reduction). The highest reduction is achieved with twenty inlets, resulting in a flushing-time reduction of 87 %.

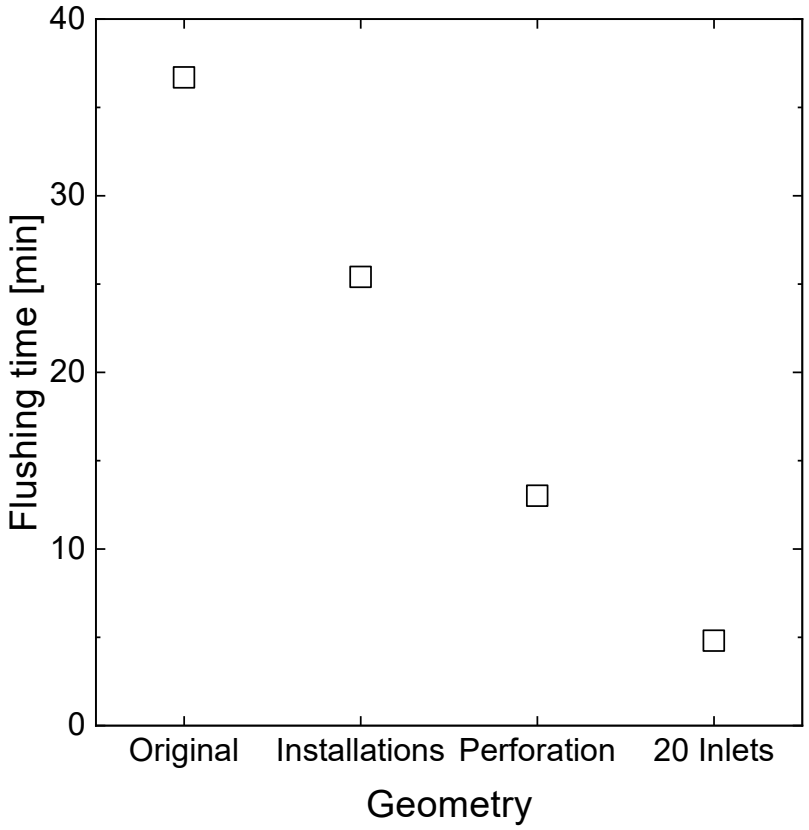

Figure 7.11.: Flushing times of geometry adaptations with baffles, perforations and twenty inlets compared to the original geometry.

Finally, the second section view is evaluated to estimate the flushing delay due to diffusive mass transfer in the porous sODC (see Figure 5.3) as a function of various inlets. The inlet velocity of each channel was extracted at the top and bottom lines of each channel according to Figure 7.12 for the ten-inlet geometry. Velocities were extracted only for those channels without own inlet. In the case of the twenty-inlet domain, all channels were evaluated. The extracted velocities were averaged and then used as new input boundaries.

The averaged N_2 mass fraction is used to evaluate the flushing time. The averaged N_2 mass fraction in the flow channel and the sODC develop almost in parallel, with a slight delay in the porous sODC. Figure 7.13 displays the flushing time between the convective flow of the empty channel and the porous sODC. However, the differences of 3.47 s to 3.68 s are similar for all investigated geometries, independent of the individual inflow

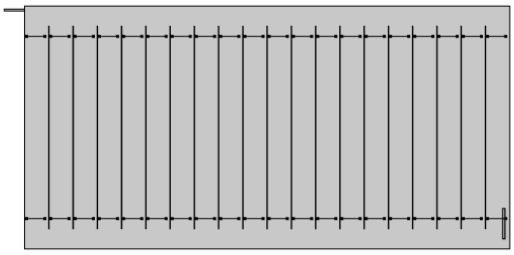

Figure 7.12.: Example arrangement of probes in the gas compartment to evaluate the velocities in the individual channels for the ten-inlet geometry.

velocity. Therefore, as a follow-up to the approach in Chapter 5.3.2, +3.68 s is proposed as an additional safety margin for flushing time calculations.

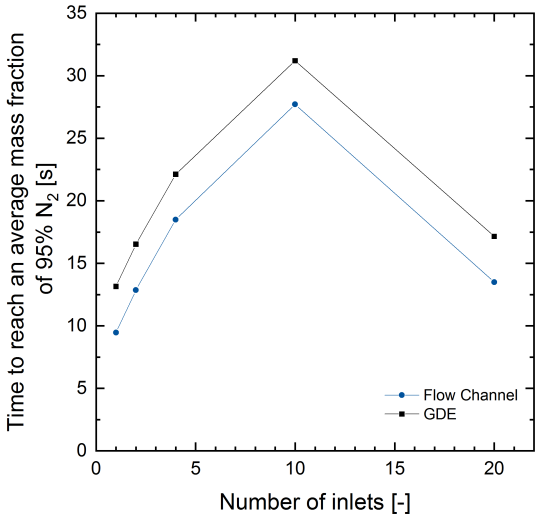

Figure 7.13.: Time to reach 95% N_2 mass fraction in flow channel or the sODC for different numbers of inlets.

However, this value should be regarded with a certain degree of caution, as

- in reality, there may be additional (partly also porous) elements above the sODC,
- the CFD simulations tend to give a too short flushing time due to their

simplifications, and

- the determined flushing times and models need further verification with the original cell.

7.4.2. Model-Based Simulative Results

The objective sets were chosen in a manner that all needs to be minimized. However, the individual objectives of the objective sets at some point reach a Pareto efficiency and cannot be minimized any further at the same time. Some iterations reduce all objectives a little and some iterations reduce a single objective a lot, but without further knowledge, a weighting of the objectives cannot be predicted. In the following, the best result of the minima from each objective set are discussed. The effect of the minimized objectives is analyzed and can support refining the correlation between the flow pattern and the flushing time.

Optimization of the Objectives

Original Geometry Figure 7.14 shows the concentration distribution and streamlines of the original geometry after four minutes (inflow contains $w_{in} = 1$). In the original geometry (no geometrical changes), each channel has at least one vortex, and the far left channel shows two vortices. After four minutes, all vortices show a higher fraction of the remaining species in the concentration plot. The blocked channel with two vortices on the left and the four channels on the right side of the cell show additional areas of remaining species. The blocked channel has an area with entirely replaced gas, while in the four channels on the right, the whole channel is affected by the slower gas exchange. They seem to build an internal stream disconnected from the main stream around the channels and slowly mix their content with the rest of the geometry. These observations coincide with the findings in Chapter 5. Thus, it was assumed that reducing or avoiding vortices in channels can improve mixing and reduce the flushing time.

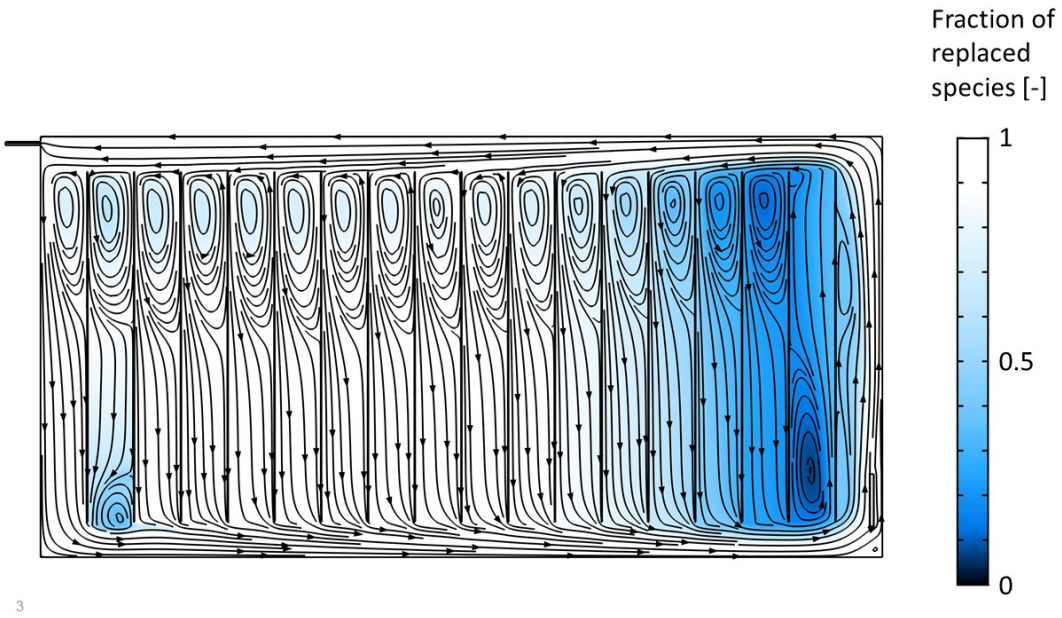

Figure 7.14.: Concentration distribution after four minutes for the original geometry without any geometrical adaptations.

Set A In objective set A, the reciprocal average volume flow ($1/\dot{V}_{avg}$, A1) and the blocked channels (*Blocked Channel*, A2) were used as objective functions. Table 7.4 summarizes the best results for objective set A compared to the original geometry. While the optimized A1 reduces the original geometry by more than half, A2 increases in size. Regarding minimizing the second target, A2 is reduced to the desired number of 0 for several combinations. At the same time, A1 is reduced to roughly half the value of the original geometry.

The absence of blocked channels for the best result of A2 and the improved volume flow compared to the original geometry promise a faster flush of the gas compartment. Therefore, this result is analyzed regarding its flushing behavior. A graph that summarizes all iterations of objective set A with their geometries and objective values is given in the Appendix A.3.

Set B In objective set B, besides the reciprocal average volume flow like in A1 ($1/\dot{V}_{avg}$, B1), the average vorticity (VF_{avg}, B2) and the maximum vorticity (VF_{max}, B3) were used as objective functions (see Table 7.5). For the minimal

Table 7.4.: Objective sets A

	Original	min A1	min A2
A1 — $1/\dot{V}_{avg}$	170.59 s m^{-2}	78.92 s m^{-2}	93.7 s m^{-2}
A2 — *Blocked Channel*	1.03	1.95	0
Bar angle	0°	–76.86°	–85.74°
Bar shift	0 mm	2.86 mm	3.75 mm

B1, both B1 and B2 get reduced to almost one-third, while B3 remains at the initial value. In the second set, although B2 gets reduced a lot to 22 %, the improvement of B1 is only by one-third, and B3 again remains close to the initial value. Finally, in the third set, B3 gets reduced by a third, B1 by half and B2 to one-third. The results of the iterations are given in the Appendix, Figure A.4.

Table 7.5.: Objective sets B

	Original	min B1	min B2	min B3
B1 — $1/\dot{V}_{avg}$	170.59 s m^{-2}	75.75 s m^{-2}	106.53 s m^{-2}	96.65 s m^{-2}
B2 — VF_{avg}	0.734	0.25	0.165	0.27
B3 — VF_{max}	0.981	0.991	0.979	0.684
Bar angle	0°	–77.75°	–70.56°	–80.41°
Bar shift	0 mm	4.89 mm	3.19 mm	3.64 mm

Set C In objective set C, the reciprocal of the minimum volume ($1/\dot{V}_{min}$, C1) and the maximum vorticity (VF_{max}, C2), which is equal to B3, were used as objectives (see Table 7.6). Minimizing C1, it gets reduced to 20 % while C2 remains at the original cell's value. C2 can be minimized by 10 % only (C1 reduces to 40 %). All iterations for objective set C can be found in the Appendix Figure A.5.

Table 7.6.: Objective sets C

	Original	min C1	min C2
C1 — $1/\dot{V}_{min}$	2725.5 s m^{-2}	467.3 s m^{-2}	1115.7 s m^{-2}
C2 — VF_{max}	0.981	0.9997	0.877
Bar angle	0°	84.59°	–79.48°
Bar shift	0 mm	3.23 mm	4.12 mm

Overall, the Bayesian Optimization algorithm successfully reduced all objectives and found some geometries that even reduced all objectives simultaneously. However, regarding the broad range of inputs (bar angle between –89.00 ° and 75.85 °, bar shift between 0 mm and 4.89 mm), resulting optima were rather similar. Thus, the vorticity, believed to be a significant cause for channel blocking and, thus high flushing time, is discussed in more detail.

Figure A.6 in the Appendix shows the correlation between the inputs 'bar angle' and 'bar shift' regarding the objectives average and the maximum vorticity fraction. It can be noticed that the two marked black lines have similar values for the inputs (–80.41 °, –78.80 °, 3.64 mm for both), but large changes in the maximum vorticity. To be more precise, the maximum vorticity changes from 0.684 to 0.980, which is a major change caused by a slight change of inputs. On the other side, substantial input variations do not necessarily lead to changes in the objective maximum vorticity. This shows a rather independent and unstable behavior of the vortices on geometry changes. Most likely, the performance of the Bayesian Optimization algorithm was affected by this behavior regarding its possibility to calculate the posterior. This led to several iterations that could not be incorporated into the data set of successful iterations. Therefore, better solutions may exist than those found by the algorithm.

Flushing Time

So far, optimized geometries have been evaluated only regarding resulting flow behavior. In the following, the connection regarding concentration distribution is rated via flushing time evaluation.

As mentioned in Chapter 5, the flushing time is the time until the concentration of replaced species reaches 95 %. The concentration is evaluated averaged over the whole area (*Average*) and for the smallest fraction of replaced species in the whole area (*Minimum*). Table 7.7 provides an overview of the considered flushing times of the optimized objective sets discussed so far. The maximum simulation time was 30 min and is exceeded by some

data sets.

Table 7.7.: Flushing time in minutes

Replaced species $> 95\,\%$	Original	A1	A2	B1	B2	B3	C1	C2
Average	**12**	28	¿30	28	28	¿30	**19**	¿30
Minimum	**21**	¿30	¿30	¿30	¿30	¿30	**25**	¿30

The original geometry takes 12 min until the geometry is flushed for the average case. Considering the minimum concentration takes 21 min for the flush. The fastest flush of the optimized geometries is realized for C1 and takes 19 min for the average case and 25 min for the case of minimum concentration. Both numbers exceed the original geometry meaning that the Bayesian Optimization could not succeed in a flushing time reduction. The increase in flushing time for all optimized geometries A1-C2 shows that the method does not include all influences and has to be reworked.

The original geometry is compared to the results with the highest improvement (C1, B3 and A2) to analyze flow and concentration distribution correlations further. Therefore, the N_2 concentration distributions after 4 min are analyzed. The optimized geometries all reduce the amount of bars and show negative bar angles (incline from left to right) apart from set C1, where the bars incline from right to left. The channels still contain at least one vortex; some show two vortices (blocked channels).

In set C1, the amount of bars reduces from seventeen to eight, and the number of blocked channels is two. The streamlines suggest that the fluid from some channels moves into the same channels where it originates. This effect leads to a circular fluid movement without access to the fluid surrounding this circle. Also, the center of the vortices contains a higher fraction of remaining species than the fluid outside. This is also the main difference for the blocked channels in the original cell, showing a higher

concentration in the vortices and almost entirely exchanged gas. On the contrary, the outer space of the cell domain is successfully flushed, and O_2 is exchanged after 4 min. One possible reason for the poor flushing efficiency can be the length and width of the channels. Since the whole channel is almost always affected by blocking vortices, longer and broader channels lead to a larger amount of remaining O_2. This effect is a possible reason for the lack of reducing the flushing time. Improved mixing across the channels could be a solution to solve this problem. The velocity plot Figure 7.15 for C1 indicates a correlation between the lowest fraction of replaced species and the small velocity inside the top two blocked channels.

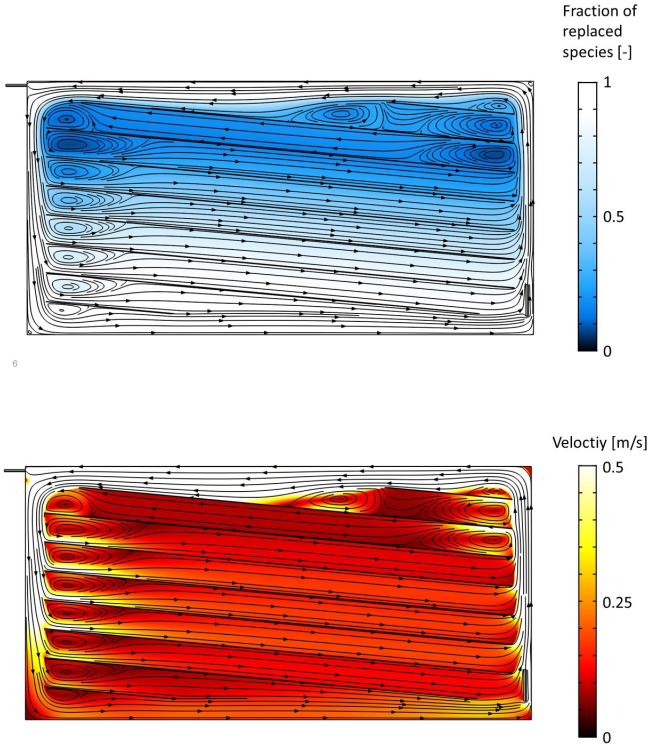

Figure 7.15.: C1: a) Concentration distribution after 4 min for an incoming flow of $w_{in} = 1$, b) streamlines and velocity distribution.

The major differences in the flow field of objective B3 (see Figure 7.16) compared to C1 are the amount and position of the vortices. This geometry has two channels without vortex and two with two vortices. The flow field in Figure 7.16 b) is superior to C1. Taking the concentration distribution in Figure 7.16 a) into account, this geometry shows an inferior result: The

channel containing two vortices shows darker blue colors and thus seems to suffer more from insufficient species exchange compared to the blocked channels in C1. In the blocked channels of B3, the concentration of replaced species reaches zero. Here, the vortex shows even a higher concentration than the channel surrounding the vortex, indicating a very strong influence from the blockage. The streamlines in Figure 7.16 b) indicate a lack of mixing with the main stream. A sharp concentration defect in the second channel from the bottom shows a possible simulation error without physical cause. The blocked channel in B3 shows a much darker color than the other channels indicating very low velocities down to $\sim 0.007\,\mathrm{m\,s^{-1}}$. This observation suggests that a lower velocity causes a higher fraction of remaining species (corresponding to a lower concentration). While the concentration increases, the fluid velocity decreases towards the vortex centers.

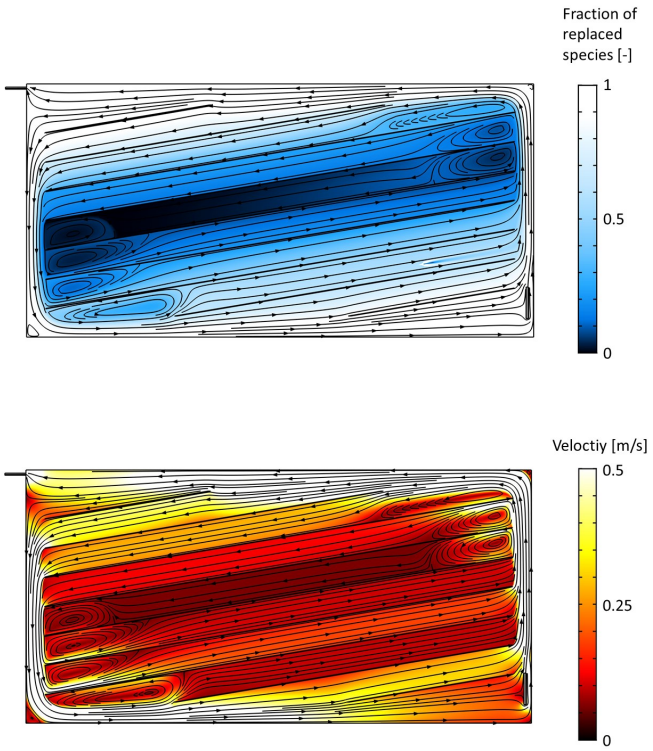

Figure 7.16.: B3: a) Concentration distribution after 4 min for an incoming flow of $w_{in} = 1$, b) streamlines and velocity distribution.

Results for objective set A2 disprove the theory that a geometry without blocked channels by two vortices has a homogeneous flushed area and,

thus, a short flushing time. Figure 7.17 a) shows one vortex in each channel. Two channels display a very dark color, indicating low concentration and inferior gas exchange. Similar to the other simulations, the space near the cell walls is completely flushed, and some channels do not mix with the main stream. The velocity plot in Figure 7.17 b) shows relatively low velocities in the channels with the lowest concentration. The velocity in other channels is higher but does not correlate with the amount of replaced species. The bottom channel indicates a small velocity but is fully replaced simultaneously, while other channels with the same velocity have only small amounts of replaced species.

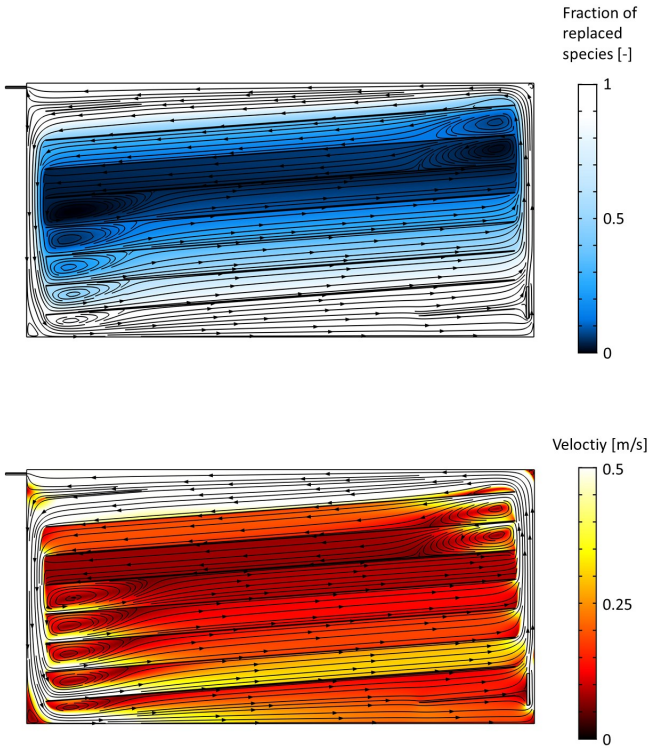

Figure 7.17.: A2: a) Concentration distribution after four minutes for an incoming flow of $w_{in} = 1$, b) streamlines and velocity distribution.

7.4.3. Experimental Results

The experimental geometry-optimization approach focuses on such internals that can be 3D-printed and combined flexibly. The evaluation of the

3D-printed geometries is based on the weighting model discussed in Chapter 7.3.3. Finally, the flushing time and pressure drop were analyzed for various prototype cell designs.

However, the visualization experiments could not be verified with the prototype cell since not enough fog could be accumulated to fill the cell. Figure 7.18 shows fog generated from the FlowMarker® entering the prototype cell inlet. Only thin fog layers are visible. Fog accumulation could be further improved by, for example, placing multiple inlets in the cell, accumulating the fog in the glass tube in batches, or by implementing a negative pressure at the outlet.

Figure 7.18.: Prototype-cell inlet with fog using the FlowMarker®.

Therefore, experimental geometry variation was performed regarding concentration and pressure drop measurements. Figure 7.19 shows flushing times for the original geometry, the meander, the meander transverse, and the cascade at two different volume flows. As in the industrial cell experiments, a higher gas flow rate decreases the flushing time. Only the meander structure leads to a noticeable reduction in flushing time from 204 s0 to 170 s at 0.33 L min^{-1}. However, the modular prototype cell shows potential for on-the-fly cell design optimization via experiments. Furthermore, the modular prototype experiments could be used to verify the geometry adaptions found by the Bayesian Optimization.

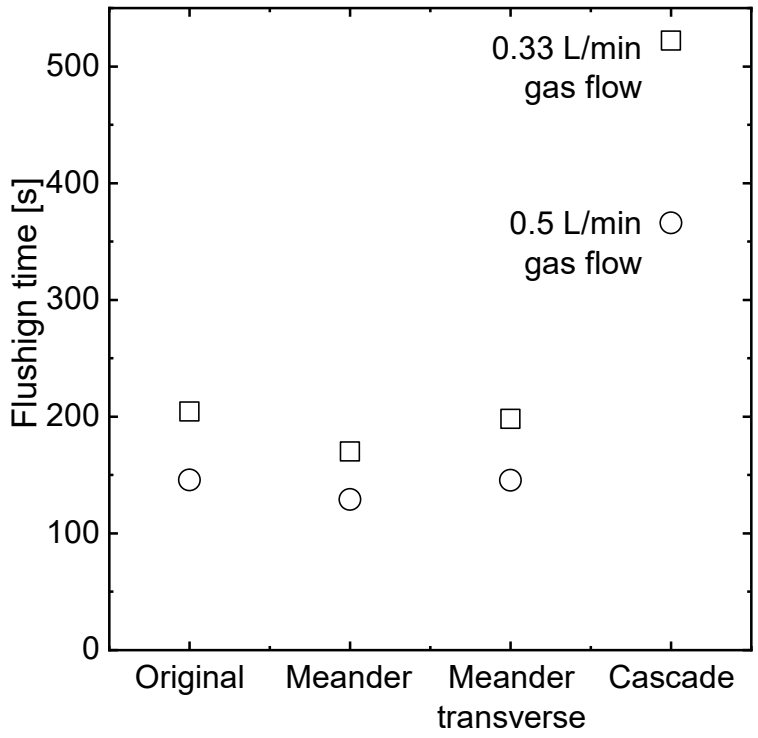

Figure 7.19.: Flushing times of concentration experiments of selected prototype cell designs.

While the cascade geometry significantly extends the flushing time to 522 s (0.33 L min^{-1}), the pressure drop in this geometry (611 mbar) is lower than in the original geometry (613 mbar, N_2 flow). However, examination of the pressure drops otherwise revealed only minor differences between the various prototype geometries in the order of 611 mbar to 620 mbar (N_2 flow), and is therefore not used for further geometry evaluation.

7.5. Conclusion

This chapter presents three approaches for cell design optimizations: CFD simulations, optimization algorithms, and experiments with a modular prototype cell. Several geometry adaptations were implemented and evaluated regarding their flushing time. First, flow simulations were combined with mass transport models to obtain flushing times. The arbitrary geometry

adaptations contained several inlets (one to twenty in number), triangular baffles in the top channel, perforations in the vertical bars, or consisted of horizontal bars. All geometry adaptations have led to a reduction in the flushing time. The geometry with twenty inlets achieved the most significant decrease with 87 % to 4.9 min. It was shown that regardless of the number of inlets, a safety margin of +3.68 s can be added on top due to the porous sODC.

A Bayesian Optimization algorithm implemented in Matlab was used to modify the bar angle and shift of the gas compartment internals to obtain a homogeneous concentration distribution for a minimized flushing time. However, it was decided to instead improve only the flow pattern due to the high computational cost of the concentration simulations and to reduce the abstraction level. The fluid flow through the channels generated vortices inside them which strongly influenced the flushing behavior. Therefore, pronounced flow characteristics were aggregated in three different objective sets. A custom evaluation algorithm in Matlab extracted the simulation data from COMSOL, calculated the objectives and passed them to the Bayesian Optimization algorithm to be minimized. Regarding the desired objectives, the Bayesian Optimization algorithm increased the channel volume flow and reduced vorticity. Against expectations, the optimized geometries could not reduce the flushing time compared to the original geometry. It was observed that local circular currents emerged from vortices, which then only minimally interacted with the incoming gas from the main fluid stream. This fluid entrapment impeded a thorough species exchange in the entire domain. The optimization algorithm generated fewer and, thus, wider channels in most cases. These larger channel areas were observed to suffer the most from the disconnection through blocking vortices.

In the concentration experiments, a clear reduction in flushing time could only be observed for a meander structure. Visualization experiments with fog could directly clarify the effects of possible geometry changes and accelerate the design optimization. Fog experiments with the prototype cell, however, still need further adjustments regarding the setup.

In conclusion, the optimization efforts only partially improved the cell geometry. However, the CFD simulations and the Matlab algorithm provide a framework that can be extended by further promising objective functions. One possibility is to refine the correlation between flow pattern and flushing time or to adjust the Bayesian Optimization algorithm based on concentration-related objectives directly. Other adaptations could be analyzed in more detail. Especially, bar perforations and several inlets showed to be promising. Lastly, it has been demonstrated that experiments with moving internals can be used flexibly, directly visualizing the effect of geometry changes on the flow distribution. Still, larger fog volumes are required for the examination.

8. Conclusion

With the Renewable Energy Sources Act (EEG2023) amendment, as an example, the German government recently announced aims to cover a minimum of 80 percent of gross electricity consumption to be covered by renewables by 2030. However, renewable energy generation is expected to be accompanied by strong fluctuations in the amount provided and, consequently, higher electricity prices. In particular electricity-based production processes, such as the chlor-alkali process, can help level out deviations in the energy grid. The so-called demand-side management is already tested in many industrial sectors. In CAE, the introduction of switchable oxygen depolarized cathodes (sODC) represents a considerable step forward in this flexibilization. The sODC catalyzes the energy-efficient oxygen-reduction reaction (ORR) with oxygen (O_2) consumption and the energy-intensive hydrogen-evolution reaction (HER) with hydrogen (H_2) production. Thorough flushing of the gas compartment in the cell is essential to enable switching at the same cathode in the same electrolysis cell.

This thesis investigated factors for a long and safe operation of sODC in flexible electrolysis with multiple switching steps. Conventional ODCs have already been studied in detail. In this thesis, the advanced sODC was investigated for the first time within a large number of switching cycles and in direct comparison to conventional ODCs. Particular importance was assigned to the cathode and cell potentials of the two cathode reactions and how these develop at different current densities and volume currents. The long-term stability of the sODC was evaluated based on the cell potential at up to 1,600 switching cycles at a predefined current density. The effects of switching cycles were estimated using contact angle measurements of the sODC before and afterward. The long-term switching experiments resulted in a cell potential increase of +5.1 % in H_2 mode and +7.8 % in O_2 mode. Substantial cell potential increases occurred in cases of flooding; to be more precise, electrolyte breakthrough through the sODC into the gas space. The increase of cell potential in combination with flooding is attributed to electrowetting. Further research on sODC composition in combination with long-term testing and switching cycles is required to make the sODC more

stable for long-term operation.

Another important aspect of switching between the two cathode reactions is the evacuation of the gas compartment of the cell to exclude oxyhydrogen formation. The gas compartment contains structures to support the porous sODC. These internals redirect the incoming gas flow so that dead zone formation occurs in the current design of commercial cells. The design impedes a fast and residue-free gas exchange. Therefore, another goal of this thesis was to investigate the supporting internals of a commercial cell design and how they affect the flow distribution during gas exchange. Gas exchange means that another gas enters through the cell inlet to displace the existing gas in the case of flushing or oxygen filling.

Monitoring the concentration distribution via CFD simulations and fog experiments unraveled potential dead zones. The current cell design favors gas accumulations in the lower cell part on the outlet side. These hotspots prolong the gas displacement. Consequently, the concentration was analyzed not only at the outlet of the cell but also at the identified hotspots (experiments) and through minimal mass fractions (CFD simulations). In that way, the flushing time could be predicted. The CFD simulations revealed a flushing time of 36.7 min.

Moreover, gas density differences showed an enormous influence on the flooding and filling of the cell. Incoming lighter gas rises and fills the cell from top to bottom. Heavier gas descends quickly to the bottom and displaces the existing gas from the bottom to the top towards the outlet. Therefore, in a first approach, a second outlet was implemented at the lower left corner. In that way, gas density differences can be optimally utilized and result in an acceleration of the gas exchange. CFD simulations and experiments showed that the gas density differences could be utilized, which resulted in faster gas exchange.

To further enhance the gas exchange, geometry adaptations of the internals were varied and implemented in further CFD simulations. Different geometries and several inlets were tested. A simple configuration could be realized via perforations of the existing vertical bars in the default cell design. The perforated design reduced the flushing time by 65 %. The most con-

siderable reduction with 87 % occurred in the case of one separate inlet in each channel but would require a more dedicated geometry transformation.

In addition to these manual cell configurations, optimization-based simulations were implemented. Here, an attempt was made to use objective functions and the flow pattern to infer improved concentration distribution and, thus, faster flushing. However, flushing time reduction was not achieved with the optimization-based algorithm. Therefore, further research, e.g., in combination with CFD simulations and optimization algorithms, is necessary with respect to cell design enhancement and flushing effectiveness. Further, experimental visualization possibilities, such as those presented with fog, are a helpful addition to verify the geometry changes.

A. Appendix

Functionality of the Optical Oxygen Sensor

The O_2 sensors are based on the optical luminescence method. The optical O_2 sensor consists of an O_2-sensitive indicator and a probe body. The indicator is a fiber optic cable with a transparent polymer membrane attached to the tip [Béni2017]. The membrane is coated with a luminescent O_2-sensitive dye, the luminophore. The probe body consists of an LED and a photodiode. The LED emits pulsed orange-red light with a wavelength of 610 to 630 nm. The light pulse excites the polymer membrane's luminophore, emitting infrared light with a wavelength of 760 to 790 nm. The photodiode can excite the indicator and receive its O_2 concentration-dependent light emission [Pyro]. In contact between the luminophore and the O_2 molecules, the gas molecules reduce the intensity of the emitted infrared radiation. The probe body picks up the infrared radiation via the photodiode and can thus infer O_2 concentration in the measurement volume. The fiber optic cable transmits both the LED's exciting light and the luminophore's infrared radiation between the indicator and the probe body. The measurement method is characterized by high precision and reliability, low energy consumption, and fast response time [Pyro].

Other Gas Combinations of the Experimental Industry-Cell Flush

The density effect was further investigated with more density difference pronounced density differences. Therefore, a He-Ar combination was compared to N_2-O_2. The gas combinations were used with the top outlet in the case of heavier flushing gas and the bottom outlet in the case of flushing with lighter gas. Figure A.1 shows the data points of the gas bag samples of the He-Ar combination. The measurement points were approximated with a spline to estimate the flushing times. The continuous measurements of the O_2-N_2 combination are shown as a continuous line.

When displacing heavy with lighter gas, the Ar-He combination with the bottom outlet initially shows a rapid concentration drop at the outlet. However, the flushing time of the according density combination O_2N_2 is in a similar

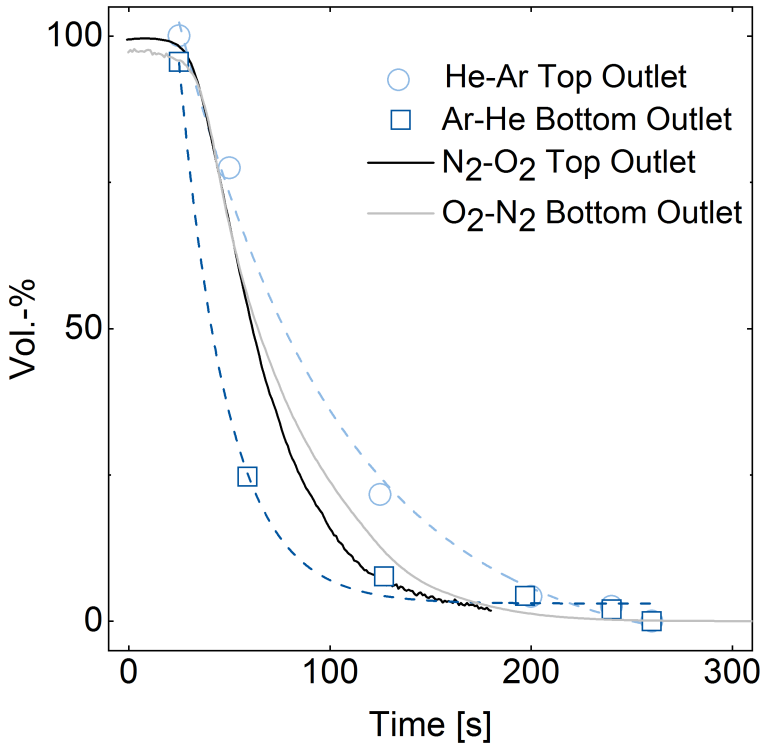

Figure A.1.: Comparison of various gas combinations and different outlets sampled at the outlet.

range at 188 s (197 s for Ar-He, see Figure 6.12). For the combination of lighter gas displaced by heavier gas, the He-Ar (209 s) transition is slightly faster than N_2-O_2 (184 s).

A similar curve for all four options can be observed, consistent with the e-functions known from the residence time distributions.

Original Geometry for the Bayesian Optimization

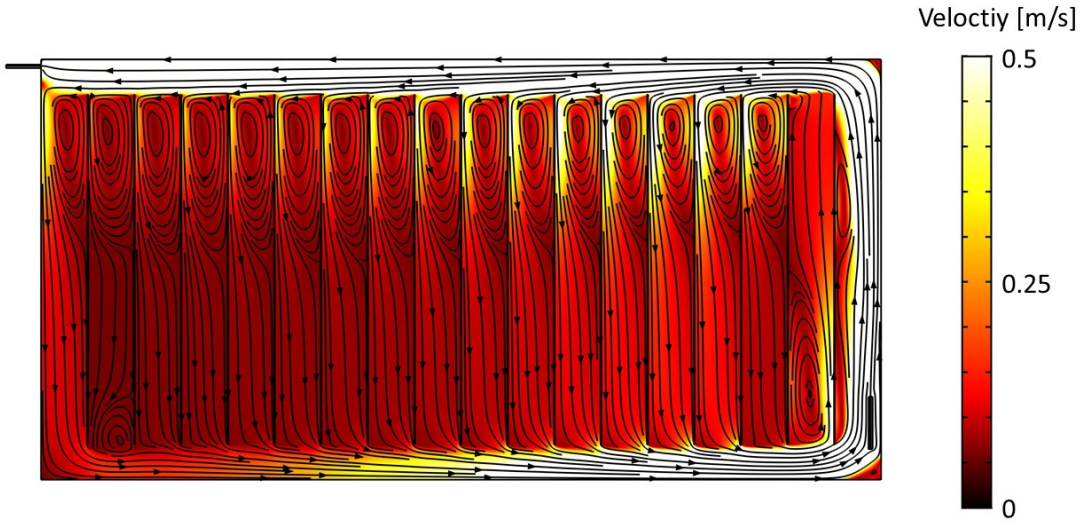

Figure A.2.: Velocity plot with streamlines for the original cell geometry for steady state conditions.

Individual Optimization Iterations for Objective Sets A to C

The first two y-axes show the pair of inputs used to parametrize the geometry. The remaining y-axes show the values of the objectives for this geometry. All values belonging to the same iteration are connected via a line. The ranges of the input and objective values are written on top and bottom of each y-axes. The best result for each objective is highlighted with a black line. The scattered line shows the results of the original geometry.

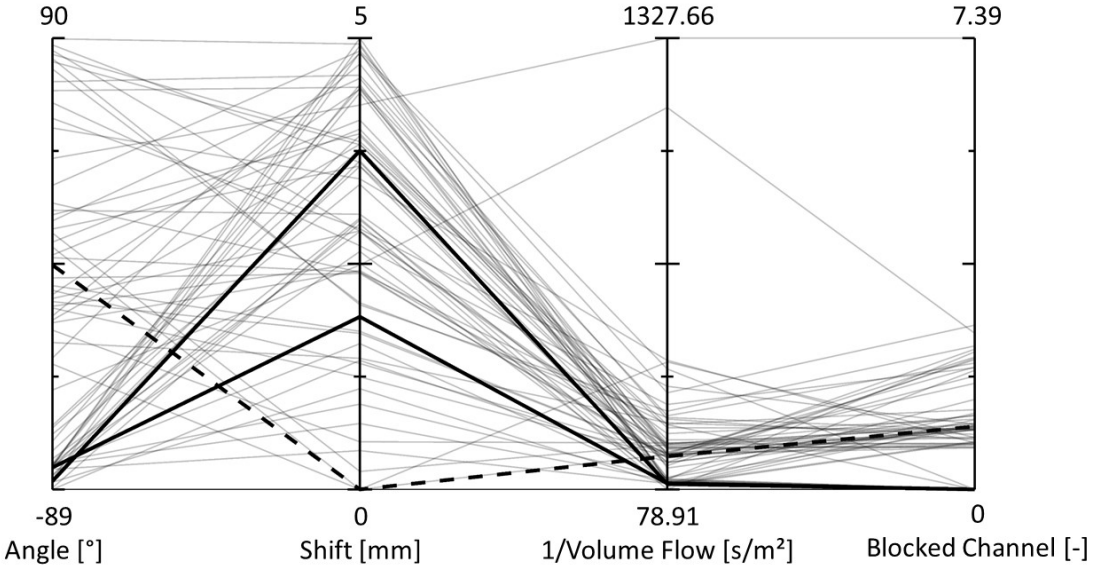

Figure A.3.: All iterations from objective set A

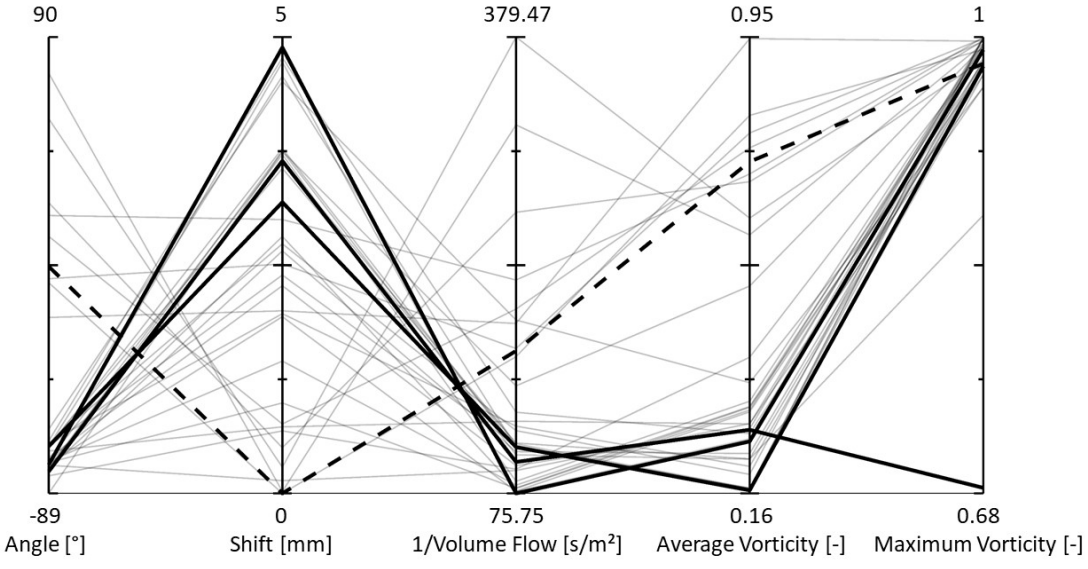

Figure A.4.: All iterations from objective set B

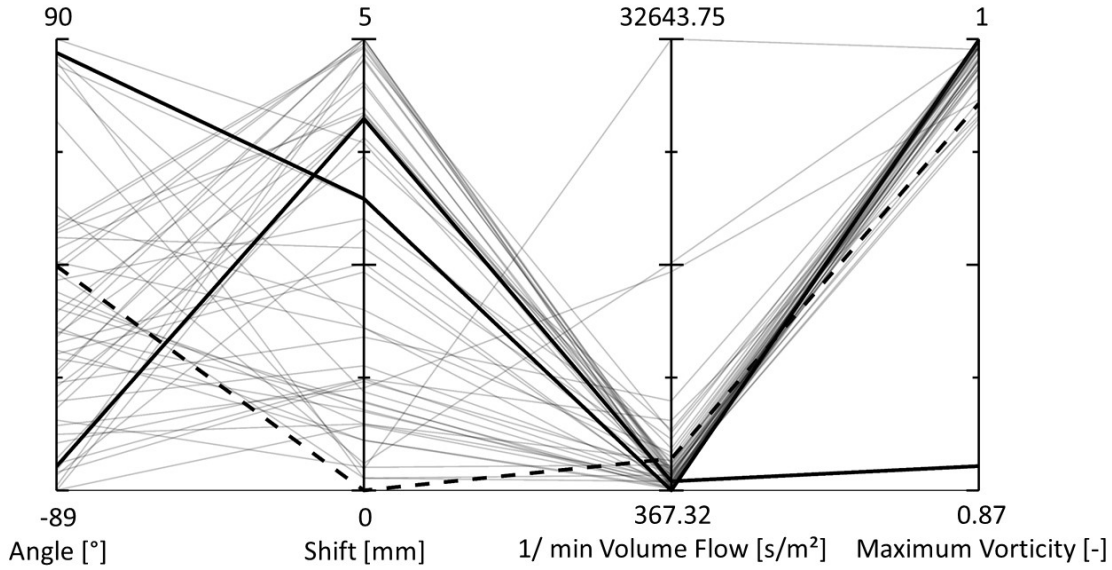

Figure A.5.: All iterations from objective set C

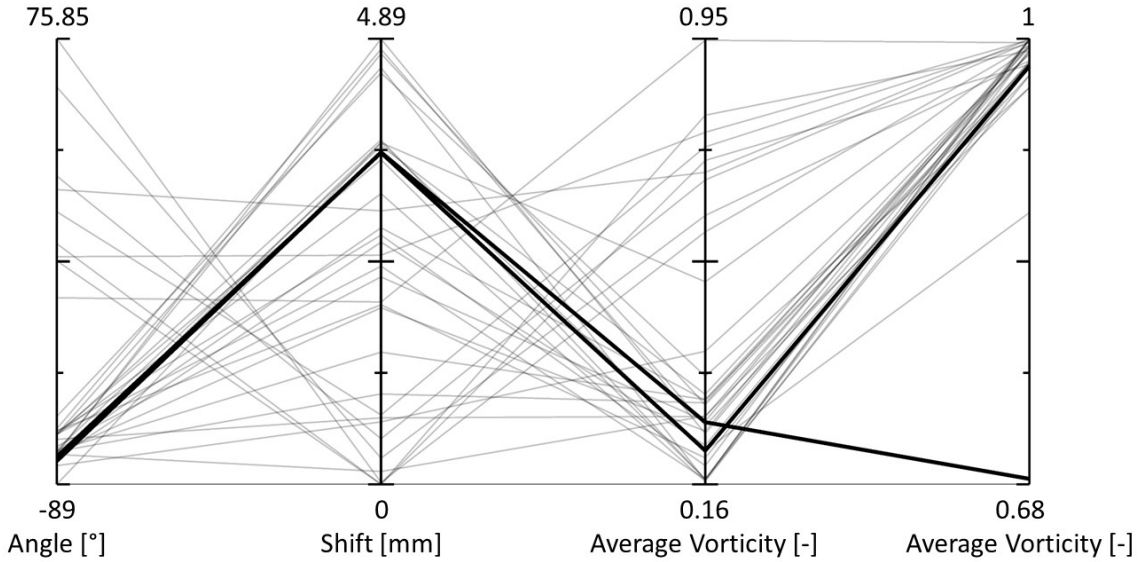

Figure A.6.: Correlation between the inputs bar angle and bar shift (first two y-axes) regarding the objectives *average* and *maximum vorticity fraction* (last two y-axes) from objective set B.

Bibliography

[Abba2008] F. Abbasi and H. Rahimzadeh. “Applying a Modified Two-Fluid Model to Numerical Simulation of Two-Phase Flow in the Membrane Chlor-Alkali Cells”. *Iran J. Chem. Chem. Eng.* 27 (2008). (Cit. on pp. 20, 34).

[Adam2008] N. Adams. *Fluidmechanik I Einführung in die Dynamik der Fluide*. Lehrstuhl für Aerodynamik Technische Universität München, 2008 (cit. on pp. 27, 29).

[Ahle2009] G. Ahlers, S. Grossmann, and D. Lohse. “Heat transfer and large scale dynamics in turbulent Rayleigh-Bénard convection”. *Reviews of Modern Physics* 81.2 (2009). (Cit. on p. 33).

[Amor2014] E. Amores, J. Rodríguez, and C. Carreras. “Influence of operation parameters in the modeling of alkaline water electrolyzers for hydrogen production”. *International Journal of Hydrogen Energy* 39.25 (2014). (Cit. on p. 15).

[Amor2017] E. Amores, J. Rodríguez, J. Oviedo, and A. De Lucas-Consuegra. “Development of an operation strategy for hydrogen production using solar PV energy based on fluid dynamic aspects”. *Open Engineering* 7.1 (2017). (Cit. on p. 15).

[Ande2012] B. Andersson, R. Andersson, L. Håkansson, M. Mortensen, R. Sudiyo, and B. Van Wachem. *Computational fluid dynamics for engineers*. Cambridge University Press, 2012 (cit. on p. 86).

[Angu2020] A. Angulo, P. van der Linde, H. Gardeniers, M. Modestino, and D. Fernández Rivas. “Influence of Bubbles on the Energy Conversion Efficiency of Electrochemical Reactors”. *Joule* 4.3 (2020). (Cit. on p. 20).

[Angu2022] A. E. Angulo, D. Frey, and M. A. Modestino. “Understanding Bubble-Induced Overpotential Losses in Multiphase Flow Electrochemical Reactors”. *Energy & Fuels* 36.14 (2022). (Cit. on p. 20).

[Ashi1997] T. Ashida, S. Wakita, M. Tanaka, Y. Nishiki, and T. Shimamune. “Chlor-alkali electrolysis with a zero-gap type oxygen cathode”. *Denki Kagaku* 65 (1997). (Cit. on p. 18).

[Atki2016] M. Atkins and M. Boer. “Chapter 2 - Flow Visualization”. In*Application of Thermo-Fluidic Measurement Techniques*. Elsevier Inc., 2016. Pp. 15–59. (Cit. on p. 33).

[Ausf2018] F. Ausfelder, H. E. Dura, K. Arnold, G. Holtz, R.-U. Dietrich, and S. Estelmann. “Flexibilitätspotenziale und -perspektiven der Chlor-Alkali Elektrolyse”. In*Flexibilitätsoptionen in der Grundstoffindustrie: Methodik, Potenziale, Hemmnisse*. Ed. by F. Ausfelder, A. Seitz, and S. von Roon. Frankfurt am Main: DECHEMA Gesellschaft für Chemische Technik und Biotechnologie e.V., 2018. (Cit. on p. 3).

[Balz2003] R. J. Balzer and H. Vogt. “Effect of Electrolyte Flow on the Bubble Coverage of Vertical Gas-Evolving Electrodes”. *Journal of The Electrochemical Society* 150.1 (2003). (Cit. on pp. 21, 39).

[Bane2014] R. Banerjee and S. G. Kandlikar. “Liquid water quantification in the cathode side gas channels of a proton exchange membrane fuel cell through two-phase flow visualization”. *Journal of Power Sources* 247 (2014). (Cit. on p. 34).

[Bard2001] A. J. Bard and L. R. Faulkner. *Electrochemical Methods: Fundamentals and Applications*. 2nd. Wiley, 2001 (cit. on p. 18).

[Bega2023] M. J. Begall, A. M. Schweidtmann, A. Mhamdi, and A. Mitsos. “Geometry optimization of a continuous millireactor via CFD and Bayesian optimization”. *Computers & Chemical Engineering* 171 (2023). (Cit. on pp. 31, 33, 130).

[Beng2000] C. Bengoa, A. Montillet, P. Legentilhomme, and J. Legrand. “Characterization and modeling of the hydrodynamic behavior in the filter-press-type FM01-LC electrochemical cell by direct flow visualization and residence time distribution”. *Industrial and Engineering Chemistry Research* 39.7 (2000). (Cit. on p. 33).

[Béni2017] P. Bénit, D. Chrétien, M. Porceddu, C. Yanicostas, M. Rak, and P. Rustin. “An Effective, Versatile, and Inexpensive Device for Oxygen Uptake Measurement”. *Journal of Clinical Medicine* 6.6 (2017). (Cit. on p. 174).

[Berg1982] D. Bergner. “Membrane cells for chlor-alkali electrolysis”. *Journal of Applied Electrochemistry* 12.6 (1982). (Cit. on p. 14).

[Bien2022] F. Bienen, M. C. Paulisch, T. Mager, J. Osiewacz, M. Nazari, M. Osenberg, B. Ellendorff, T. Turek, U. Nieken, I. Manke, and K. A. Friedrich. “Investigating the electrowetting of silver-based gas-diffusion electrodes during oxygen reduction reaction with electrochemical and optical methods”. *Electrochemical Science Advances* 3.1 (2022). (Cit. on pp. 23, 62, 63).

[Bird2002] R. Bird, W. Stewart, and E. Lightfoot. *Transport Phenomena, Second Edition*. John Whiley & Sons, Inc, 2002 (cit. on p. 28).

[Bisa1991] J. M. Bisang. “Theoretical and experimental studies of current distribution in gas-evolving electrochemical reactors with parallel-plate electrodes”. *Journal of Applied Electrochemistry* 21.9 (1991). (Cit. on p. 20).

[Brad2018] E. Bradford, A. M. Schweidtmann, and A. Lapkin. “Efficient multiobjective optimization employing Gaussian processes, spectral sampling and a genetic algorithm”. *Journal of Global Optimization* 71 (2018). (Cit. on p. 31).

[Brau2020] J. Brauns and T. Turek. “Alkaline water electrolysis powered by renewable energy: A review”. *Processes* 8.2 (2020). (Cit. on p. 15).

[Brée2019] L. C. Brée, K. Perrey, A. Bulan, and A. Mitsos. “Demand side management and operational mode switching in chlorine production”. *AIChE Journal* 65.7 (2019). (Cit. on pp. 4, 14, 15, 26, 44, 50).

[Brée2020] L. C. Brée, A. Bulan, R. Herding, J. Kuhlmann, A. Mitsos, K. Perrey, and K. Roh. “Techno-Economic Comparison of Flexibility Options in Chlorine Production”. *Industrial and Engineering Chemistry Research* 59.26 (2020). (Cit. on pp. 14, 15, 50).

[Broc2010] E. Brochu, V. M. Cora, and N. d. Freitas. *A Tutorial on Bayesian Optimization of Expensive Cost Functions, with Application to Active User Modeling and Hierarchical Reinforcement Learning*. 2010 (cit. on p. 32).

[Bula2017] A. Bulan, R. Weber, and F. Bienen. *Difunctional electrode and electrolysis device for chlor-alkali electrolysis*. Patent WO 2017/174563 A1. 2017 (cit. on pp. 3, 13, 19–21, 26, 36, 38, 48, 53, 56, 84).

[Chav2015] N. Chavan, S. Pinnow, G. D. Polcyn, and T. Turek. "Non-isothermal model for an industrial chlor-alkali cell with oxygen-depolarized cathode". *Journal of Applied Electrochemistry* 45.8 (2015). (Cit. on pp. 23, 34).

[Chen2012] R. Chen, V. Trieu, H. Natter, J. Kintrup, A. Bulan, and R. Hempelmann. "Wavelet analysis of chlorine bubble evolution on electrodes with different surface morphologies". *Electrochemistry Communications* 22 (2012). (Cit. on pp. 20, 21).

[Chli2004] J. Chlistunoff. *Advanced Chlor-Alkali Technology*. Tech. rep. New Mexico: Los Alamos National Laboratory, 2004, pp. 1–100 (cit. on p. 11).

[COMS2017] COMSOL Multiphysics. *COMSOL Reference Manual*. COMSOL Multiphysics GMbH, 2017 (cit. on p. 31).

[Dohl2003] H. Dohle, R. Jung, N. Kimiaie, J. Mergel, and M. Müller. "Interaction between the diffusion layer and the flow field of polymer electrolyte fuel cells - Experiments and simulation studies". *Journal of Power Sources* 124.2 (2003). (Cit. on p. 34).

[Durs2006] F. Durst. *Grundlagen der Strömungsmechanik Eine Einführung in die Theorie der Strömungen von Fluiden*. Springer-Verlag, 2006 (cit. on pp. 27, 29, 30).

[Erya2022] I. Eryazici, N. Ramesh, and C. Villa. "Electrification of the chemical industry—materials innovations for a lower carbon future". *MRS Bulletin* 46.December (2022). (Cit. on p. 3).

[Euro2021] Eurochlor. *Eurochlor 2021 - Chlor Alkali Industry Review 2020-2021*. Tech. rep. 2021, pp. 2013–2015 (cit. on pp. 3, 12).

[Fede2001] F. Federico, G. N. Martelli, and D. Pinter. “Chapter 9 Gas-diffusion Electrodes for Chlorine-related Production Technologies”. 8 (2001). (Cit. on p. 11).

[Figu2013] R. S. Figueiredo, R. Bertazzoli, and C. A. Rodrigues. “Copper/Carbon/PTFE oxygen-depolarized cathodes for chlor-alkali membrane cells”. *Industrial and Engineering Chemistry Research* 52.16 (2013). (Cit. on pp. 16, 19, 50, 53).

[Fock1986] W. W. Focke and P. G. Knibbe. “Flow visualization in parallel-plate ducts with corrugated walls”. *Journal of Fluid Mechanics* 165 (1986). (Cit. on p. 33).

[Fran2019] D. Franzen, B. Ellendorff, M. C. Paulisch, A. Hilger, M. Osenberg, I. Manke, and T. Turek. “Influence of binder content in silver-based gas diffusion electrodes on pore system and electrochemical performance”. *Journal of Applied Electrochemistry* 49.7 (2019). (Cit. on pp. 16, 23, 63, 65).

[Furu1998] N. Furuya and H. Syojaku. “Ag base oxygen cathodes for chlor-alkali membrane cells”. In*The Electrochemical Society Proceedings*. 1998, pp. 243–250 (cit. on pp. 17, 18).

[Furu2000] N. Furuya and H. Aikawa. “Comparative study of oxygen cathodes loaded with Ag and Pt catalysts in chlor-alkali membrane cells”. *Electrochimica Acta* 45.25-26 (2000). (Cit. on pp. 4, 15, 19, 44, 53, 56, 62).

[Gebh2019] M. Gebhard, M. Paulisch, A. Hilger, D. Franzen, B. Ellendorff, T. Turek, I. Manke, and C. Roth. “Design of an in-operando cell for X-ray and neutron imaging of oxygen-depolarized cathodes in chlor-alkali electrolysis”. *Materials* 12.8 (2019). (Cit. on pp. 19, 53).

[Gili1981] L. J. Giling. “Gasflow Patterns in Horizontal Epitaxial Reactor Cells As Observed By Interference Holography.” *Proceedings - The Electrochemical Society* 81-7 (1981). (Cit. on p. 34).

[Grou2019] S. Group. *SIGRACET Gas Diffusion Layers for PEM Fuel Cells, Electrolyzers and Batteries*. Jan. 2019. URL: http://www.sglgroup.com (visited on 01/2019) (cit. on p. 84).

[Günt2011] Günther Schaidt Safex-Chemie GmbH. *Safety Data Sheet*. 2011 (cit. on p. 146).

[Hama2005] C. H. Hamann and W. Vielstich. *Elektrochemie*. Wiley-VCH, 2005 (cit. on p. 24).

[Haug2017a] P. Haug, M. Koj, and T. Turek. “Influence of process conditions on gas purity in alkaline water electrolysis”. *International Journal of Hydrogen Energy* 42.15 (2017). (Cit. on pp. 15, 20, 21, 39, 46).

[Haug2017b] P. Haug, B. Kreitz, M. Koj, and T. Turek. “Process modelling of an alkaline water electrolyzer”. *International Journal of Hydrogen Energy* 42.24 (2017). (Cit. on p. 39).

[Jala2009] A. A. Jalali, F. Mohammadi, and S. N. Ashrafizadeh. “Effects of process conditions on cell voltage, current efficiency and voltage balance of a chlor-alkali membrane cell”. *Desalination* 237.1-3 (2009). (Cit. on p. 46).

[Jean2018] P. Jeanty, C. Scherer, E. Magori, K. Wiesner-Fleischer, O. Hinrichsen, and M. Fleischer. “Upscaling and continuous operation of electrochemical CO2 to CO conversion in aqueous solutions on silver gas diffusion electrodes”. *Journal of CO2 Utilization* 24 (2018). (Cit. on pp. 22, 64).

[Jöri2011] J. Jörissen, T. Turek, and R. Weber. “Chlorherstellung mit Sauerstoffverzehrkathoden. Energieeinsparung bei der Elektrolyse”. *Chemie in Unserer Zeit* 45.3 (2011). (Cit. on pp. 3, 12, 14, 18, 21, 22, 50, 51, 56, 57, 64).

[Kald2022] A. M. Kalde, M. Grosseheide, S. Brosch, S. V. Pape, R. G. Keller, J. Linkhorst, and M. Wessling. “Micromodel of a Gas Diffusion Electrode Tracks in-operando Pore-Scale Wetting Phenomena”. *SMALL* (2022). (Cit. on pp. 24, 62, 63).

[Kint2017] J. Kintrup, M. Millaruelo, V. Trieu, A. Bulan, and E. S. Mojica. “Gas diffusion electrodes for efficient manufacturing of chlorine and other chemicals”. *Electrochemical Society Interface* 26.2 (2017). (Cit. on pp. 50, 56).

[Kiro2004] Y. Kiros, M. Pirjamali, and M. Bursell. “Oxygen Reduction Electrodes in Chlor-alkali Electrolysis”. In*Proceedings International Hydrogen & Fuel Cells*. Toronto, Canada, Sept. 2004 (cit. on p. 19).

[Kiro2006] Y. Kiros, M. Pirjamali, and M. Bursell. “Oxygen reduction electrodes for electrolysis in chlor-alkali cells”. *Electrochimica Acta* 51.16 (2006). (Cit. on pp. 11, 14, 17, 19, 20, 44, 50, 53, 61, 64).

[Kiro2008] Y. Kiros and M. Bursell. “Low energy consumption in chlor-alkali cells using oxygen reduction electrodes”. *International Journal of Electrochemical Science* 3.4 (2008). (Cit. on pp. 44, 50, 53, 61).

[Klau2017] F. Klaucke, T. Karsten, F. Holtrup, E. Esche, T. Morosuk, G. Tsatsaronis, and J. U. Repke. “Demand Response Potenziale in der chemischen Industrie”. *Chemie-Ingenieur-Technik* 89.9 (2017). (Cit. on pp. 3, 4, 12, 14).

[Klau2020] F. Klaucke, C. Hoffmann, M. Hofmann, and G. Tsatsaronis. “Impact of the chlorine value chain on the demand response potential of the chloralkali process”. *Applied Energy* 276 (2020). (Cit. on p. 26).

[Kuwe2016] R. Kuwertz, N. Aoun, T. Turek, and U. Kunz. “Influence of PTFE Content in Gas Diffusion Layers Used for Gas-Phase Hydrogen Chloride Electrolysis with Oxygen Depolarized Cathode”. *Journal of The Electrochemical Society* 163.9 (2016). (Cit. on p. 56).

[Laur2018] E. Laurien and H. Oertel jr. *Numerische Strömungsmechanik: Grundgleichungen und Modelle - Lösungsmethoden - Qualität und Genauigkeit*. Vierweg+Teubner Verlag, 2018 (cit. on pp. 28, 31).

[Lech2011] S. Lecheler. *Numerische Strömungsberechnung, Schneller Einstieg durch anschauliche Beispiele, 2.Auflage*. Vierweg+Teubner Verlag, 2011 (cit. on pp. 28–31).

[Lee2013] B. Lee and K. Park. “Numerical Optimization of Flow Field Pattern by Mass Transfer and Electrochemical Reaction Characteristics in Proton Exchange Membrane Fuel Cells”. *International Journal of Electrochemical Science* (2013). (Cit. on p. 34).

[Li2005] X. Li and I. Sabir. “Review of bipolar plates in PEM fuel cells: Flow-field designs”. *International Journal of Hydrogen Energy* 30.4 (2005). (Cit. on p. 143).

[Mans2012] A. P. Manso, F. F. Marzo, J. Barranco, X. Garikano, and M. Garmendia Mujika. “Influence of geometric parameters of the flow fields on the performance of a PEM fuel cell. A review”. *International Journal of Hydrogen Energy* 37.20 (2012). (Cit. on p. 143).

[Mill2013] P. Millet. *Chlor-alkali technology: Fundamentals, processes and materials for diaphragms and membranes*. Vol. 2. 11. Woodhead Publishing Limited, 2013, pp. 384–415 (cit. on p. 3).

[Moor2000] J. Moorhouse. *Modern Chlor-Alkali Technology Volume 8*. Vol. 8. 2000 (cit. on pp. 11, 80).

[Mori2000] T. Morimoto, K. Suzuki, T. Matsubara, and N. Yoshida. “Oxygen reduction electrode in brine electrolysis”. *Electrochimica Acta* 45.25-26 (2000). (Cit. on pp. 25, 53).

[Mori2021] Y. Morita, S. Rezaeiravesh, N. Tabatabaei, R. Vinuesa, K. Fukagata, and P. Schlatter. *Applying Bayesian Optimization with Gaussian Process Regression to Computational Fluid Dynamics Problems*. 2021 (cit. on p. 33).

[Mous2008] I. Moussallem, J. Jörissen, U. Kunz, S. Pinnow, and T. Turek. “Chlor-alkali electrolysis with oxygen depolarized cathodes: History, present status and future prospects”. *Journal of Applied Electrochemistry* 38.9 (2008). (Cit. on pp. 3, 4, 11, 14–17, 56, 80).

[Mous2012] I. Moussallem, S. Pinnow, N. Wagner, and T. Turek. “Development of high-performance silver-based gas-diffusion electrodes for chlor-alkali electrolysis with oxygen depolarized cathodes”. *Chemical Engineering and Processing: Process Intensification* 52 (2012). (Cit. on pp. 15–19, 22, 23, 25, 53).

[Naga2003] N. Nagai, M. Takeuchi, T. Kimura, and T. Oka. “Existence of optimum space between electrodes on hydrogen production by water electrolysis”. *International Journal of Hydrogen Energy* 28.1 (2003). (Cit. on pp. 20, 37).

[Naka1999] S. Nakamatsu, K. Saiki, A. Sakata, H. Aikawa, and N. Furuya. “Liquid-permeable gas diffusion electrode for chlor-alkali membrane cells”. In *The Electrochemical Society Proceedings*. 1999, pp. 196–208 (cit. on pp. 17, 18).

[Nara2003] V. Narayanan, R. H. Page, and J. Seyed-Yagoobi. “Visualization of air flow using infrared thermography”. *Experiments in Fluids* 34.2 (2003). (Cit. on p. 34).

[Nie2010] J. Nie and Y. Chen. “Numerical modeling of three-dimensional two-phase gas–liquid flow in the flow field plate of a PEM electrolysis cell”. *International Journal of Hydrogen Energy* 35.8 (2010). (Cit. on p. 34).

[Oert2015] H. Oertel jr., M. Böhle, and T. Reviol. *Strömungsmechanik für Ingenieure und Naturwissenschaftler*. Springer-Verlag, 2015 (cit. on pp. 28, 29).

[Okaj2005] K. Okajima, K. Nabekura, T. Kondoh, and M. Sudoh. “Degradation Evaluation of Gas-Diffusion Electrodes for Oxygen-Depolarization in Chlor-Alkali Membrane Cell”. *Journal of The Electrochemical Society* 152.8 (2005). (Cit. on p. 11).

[Otas2019] J. I. Otashu and M. Baldea. “Demand response-oriented dynamic modeling and operational optimization of membrane-based chlor-alkali plants”. *Computers & Chemical Engineering* 121 (2019). (Cit. on p. 14).

[Park2018] S. Park, J. Na, M. Kim, and J. M. Lee. “Multi-objective Bayesian optimization of chemical reactor design using computational fluid dynamics”. *Computers & Chemical Engineering* 119 (2018). (Cit. on p. 33).

[Paul2019] M. C. Paulisch, M. Gebhard, D. Franzen, A. Hilger, M. Osenberg, N. Kardjilov, B. Ellendorff, T. Turek, C. Roth, and I. Manke. “Gas Diffusion Electrodes during Oxygen Reduction Reaction in Highly Alkaline Media”. *Materials* 12.17 (2019). (Cit. on pp. 23, 62, 63).

[Paul2021] M. C. Paulisch, M. Gebhard, D. Franzen, A. Hilger, M. Osenberg, S. Marathe, C. Rau, B. Ellendorff, T. Turek, C. Roth, and I. Manke. “Operando Synchrotron Imaging of Electrolyte Distribution in Silver-Based Gas Diffusion Electrodes During Oxygen Reduction Reaction in Highly Alkaline Media”. *ACS Applied Energy Materials* 4.8 (2021). (Cit. on pp. 23, 62, 63).

[Pinn2011] S. Pinnow, N. Chavan, and T. Turek. “Thin-film flooded agglomerate model for silver-based oxygen depolarized cathodes”. *Journal of Applied Electrochemistry* 41.9 (2011). (Cit. on p. 23).

[Pyro] Pyro Science. *Optical Oxygen Sensors*. Abgerufen am: 12.10.2022. URL: https://www.pyroscience.com/en/products/theory/optical-oxygen-sensors (cit. on p. 174).

[Qiu2001] X. L. Qiu and P. Tong. "Large-scale velocity structures in turbulent thermal convection". *Physical Review E - Statistical Physics, Plasmas, Fluids, and Related Interdisciplinary Topics* 64.3 (2001). (Cit. on p. 33).

[Rasm2006] C. E. Rasmussen and C. K. I. Williams. *Gaussian Processes for Machine Learning*. the MIT Press, 2006. 266 pp. (cit. on p. 32).

[Rive2015] E. P. Rivero, M. R. Cruz-Díaz, F. J. Almazán-Ruiz, and I. González. "Modeling the effect of non-ideal flow pattern on tertiary current distribution in a filter-press-type electrochemical reactor for copper recovery". *Chemical Engineering Research and Design* 100 (2015). (Cit. on p. 34).

[Roh2019a] K. Roh, L. C. Brée, K. Perrey, A. Bulan, and A. Mitsos. "Optimal Oversizing and Operation of the Switchable Chlor-Alkali Electrolyzer for Demand Side Management". *Computer Aided Chemical Engineering* 46.2017 (2019). (Cit. on p. 14).

[Roh2019b] K. Roh, L. C. Brée, K. Perrey, A. Bulan, and A. Mitsos. "Flexible operation of switchable chlor-alkali electrolysis for demand side management". *Applied Energy* 255.September (2019). (Cit. on pp. 14, 15, 26).

[Roh2022] K. Roh, L. C. Brée, K. Perrey, A. Bulan, and A. Mitsos. "On economic operation of switchable chlor-alkali electrolysis for demand-side management". In*Simulation and Optimization in Process Engineering*. Ed. by M. Bortz and N. Asprion. Elsevier, 2022. Chap. 9, pp. 225–242. (Cit. on pp. 4, 14, 15, 26).

[Röhe2019a] M. Röhe, A. Botz, D. Franzen, F. Kubannek, B. Ellendorff, D. Öhl, W. Schuhmann, T. Turek, and U. Krewer. "The Key Role of Water Activity for the Operating Behavior and Dynamics of Oxygen Depolarized Cathodes". *ChemElectroChem* 6.22 (2019). (Cit. on p. 56).

[Röhe2019b] M. Röhe, F. Kubannek, and U. Krewer. "Processes and Their Limitations in Oxygen Depolarized Cathodes: A Dynamic Model-Based Analysis". *ChemSusChem* (2019). (Cit. on p. 4).

[Rosh2012] R. Roshandel, F. Arbabi, and G. K. Moghaddam. “Simulation of an innovative flow-field design based on a bio inspired pattern for PEM fuel cells”. *Renewable Energy* 41 (2012). (Cit. on p. 143).

[Roy2006] A. Roy, S. Watson, and D. Infield. “Comparison of electrical energy efficiency of atmospheric and high-pressure electrolysers”. *International Journal of Hydrogen Energy* 31.14 (2006). (Cit. on pp. 20, 21, 39).

[Russ2011] G. P. Russo. “6 - Flow visualization”. In*Aerodynamic Measurements*. Ed. by G. P. Russo. Woodhead Publishing, 2011. Pp. 161–216. (Cit. on p. 33).

[Saik1999] K. Saiki, A. Sakata, H. Aikawa, and N. Furuya. “Reduction in power consumption of chlor-alkali membrane cell using oxygen depolarized cathode”. In*The Electrochemical Society Proceedings*. 1999, pp. 188–195 (cit. on p. 18).

[Saka1998] A. Sakata, N. Furuya, A. Uchimura, and K. Saiki. “Application of oxygen cathode to brine electrolysis”. In*The Electrochemical Society Proceedings*. 1998, pp. 237–242 (cit. on p. 16).

[Saka1999] A. Sakata, M. Kato, K. Hayashi, H. Aikawa, and K. Saiki. “Long term performances of gas diffusion electrode in laboratory cells”. In*Proceedings of the Chlor-Alkali and Chlorate Technology: RB MacMullin Memorial Symposium, 196th Meeting of the Electrochemical Society, Hawaii*. 1999, pp. 99–21 (cit. on p. 16).

[Saue2019] A. Sauer, E. Abele, and H. U. Buhl. *Energieflexibilität in der deutschen Industrie*. Vol. 63. September. Stuttgart: Fraunhofer IRB Verlag, 2019, pp. 1–6 (cit. on pp. 3, 4, 14).

[Schm1982] D. Schmid and N. Medic. “Elektrochemische Energieumwandlung einschließlich Speicherung”. *Dechema-Monographien* 92 (1982). (Cit. on p. 16).

[Schm2003] V. M. Schmidt. *Elektrochemische Verfahrenstechnik: Grundlagen, Reaktionstechnik, Prozeßoptimierung.* Wiley-VCH, 2003. DOI: 10.1002/3527602143 (cit. on pp. 12, 18, 20).

[Schr2002] V. Schröder. *Explosionsgrenzen von Wasserstoff und Wasserstoff/Methan-Gemischen*. Forschungsbericht 253, Bundesanstalt für Materialforschung und -prüfung. 2002 (cit. on p. 72).

[Schr2004a] V. Schröder, B. Emonts, H. Janßen, and H.-P. Schulze. “Explosion Limits of Hydrogen/Oxygen Mixtures at Initial Pressures up to 200 bar”. *Chemical Engineering & Technology* 27.8 (2004). (Cit. on p. 79).

[Schr2004b] W. Schröder. *Fluidmechanik*. Süsterfeldstr. 83, 52072 Aachen: Wissenschaftsverlag Mainz, 2004 (cit. on pp. 27, 30).

[Schu2022] B. Schubert. *Wie Nebel hilft, Erkenntnisse zu gewinnen*. 2022 (cit. on p. 146).

[Schw2013] R. Schwarze. *CDF-Modellierung: Grundlagen und Anwendungen bei Strömungsprozessen*. Springer-Verlag, 2013 (cit. on p. 31).

[Seib2018] C. Seibel and J.-W. Kuhlmann. “Dynamic Water Electrolysis in Cross-Sectoral Processes”. *Chemie-Ingenieur-Technik* 90.10 (2018). (Cit. on p. 15).

[Sira2008] S. Siracusano, T. Denaro, V. Antonucci, A. S. Aricò, C. Urgeghe, and F. Federico. “Degradation of oxygen-depolarized Ag-based gas diffusion electrodes for chlor-alkali cells”. *Journal of Applied Electrochemistry* 38.12 (2008). (Cit. on pp. 4, 16, 44, 62).

[Skrz2021] P. Skrzypacz, N. Chalkarova, B. Golman, V. Andreev, and F. Schieweck. “Numerical simulations of dead zone formation in the catalytic flow-through membrane reactor”. *Computers & Chemical Engineering* 152 (2021). (Cit. on p. 143).

[Staa1985] R. Staab and D. Schmid. “Entwicklungsstand der Membranelektrolyse mit Sauerstoffverzehrkathode”. *Dechema-Monographien* 98 (1985). (Cit. on pp. 16, 18).

[Step2005] J. Stephen D. Cramer; Bernard S. Covino. “Electrochemical Series”. In*Corrosion: Materials*. ASM International, Jan. 2005. (Cit. on p. 49).

[Togh2018] S. Toghyani, E. Afshari, E. Baniasadi, and S. A. Atyabi. “Thermal and electrochemical analysis of different flow field patterns in a PEM electrolyzer”. *Electrochimica Acta* 267 (2018). (Cit. on p. 34).

[Tran2019] A. Tran, J. Sun, J. M. Furlan, K. V. Pagalthivarthi, R. J. Visintainer, and Y. Wang. “pBO-2GP-3B: A batch parallel known/unknown constrained Bayesian optimization with feasibility classification and its applications in computational fluid dynamics”. *Computer Methods in Applied Mechanics and Engineering* 347 (2019). (Cit. on p. 33).

[Tran2020] A. Tran, M. Eldred, T. Wildey, S. McCann, J. Sun, and R. J. Visintainer. *aphBO-2GP-3B: A budgeted asynchronous parallel multi-acquisition functions for constrained Bayesian optimization on high-performing computing architecture*. 2020 (cit. on p. 33).

[Uchi1997] A. Uchimura, O. Ichinose, and N. Furuya. “Gas Diffusion Electrodes Loaded with Silver Catalyst for Chlor-Alkali Electrolysis”. *Denki Kagaku* 12.65 (1997). (Cit. on p. 11).

[Ursu2012] A. Ursua, P. Sanchis, and L. M. Gandia. “Hydrogen Production from Water Electrolysis : Current Status and Future Trends”. *Proceedings of the IEEE* 100.2 (2012). (Cit. on p. 15).

[Venn2019a] J.-B. Vennekoetter, R. Sengpiel, and M. Wessling. “Beyond the catalyst: How electrode and reactor design determine the product spectrum during electrochemical CO2 reduction”. *Chemical Engineering Journal* 364 (2019). (Cit. on p. 25).

[Venn2019b] J. B. Vennekötter, T. Scheuermann, R. Sengpiel, and M. Wessling. “The electrolyte matters: Stable systems for high rate electrochemical CO2 reduction”. *Journal of CO2 Utilization* 32.February (2019). (Cit. on p. 38).

[Vere2013] Verein deutscher Ingenieure. *VDI-Wärmeatlas*. Ed. by VDI e.V. 11th ed. VDI-Buch. Berlin Heidelberg: Springer, 2013 (cit. on pp. 73, 85, 96).

[Vinc2017] I. Vincent, A. Kruger, and D. Bessarabov. “Development of efficient membrane electrode assembly for low cost hydrogen production by anion exchange membrane electrolysis”. *International Journal of Hydrogen Energy* 42.16 (2017). (Cit. on pp. 17, 62).

[Vinc2018] I. Vincent and D. Bessarabov. “Low cost hydrogen production by anion exchange membrane electrolysis: A review”. *Renewable and Sustainable Energy Reviews* 81.May (2018). (Cit. on p. 17).

[Wagn2004] N. Wagner, M. Schulze, and E. Gülzow. “Long term investigations of silver cathodes for alkaline fuel cells”. *Journal of Power Sources* 127.1 (2004). (Cit. on pp. 56, 62).

[Wang2014] X. Wang, C. Tong, A. Palazoglu, and N. H. El-Farra. “Energy management for the chlor-alkali process with hybrid renewable energy generation using receding horizon optimization”. *Proceedings of the IEEE Conference on Decision and Control* 2015-Febru.February (2014). (Cit. on p. 14).

[Wang2020] Y. Wang, Y. Du, M. Ni, R. Zhan, Q. Du, and K. Jiao. “Three-dimensional modeling of flow field optimization for co-electrolysis solid oxide electrolysis cell”. *Applied Thermal Engineering* 172 (2020). (Cit. on p. 34).

[Weig2021] J. Weigert, C. Hoffmann, E. Esche, P. Fischer, and J. U. Repke. “Towards demand-side management of the chlor-alkali electrolysis: Dynamic modeling and model validation”. *Computers and Chemical Engineering* 149 (2021). (Cit. on p. 14).

[Wies2018] M. Wiese, S. Benders, B. Blümich, and M. Wessling. “3D MRI velocimetry of non-transparent 3D-printed staggered herringbone mixers”. *Chemical Engineering Journal* 343 (2018). (Cit. on p. 144).

[Wrig2006] J. L. Wright, H. Jin, K. G. Hollands, and D. Naylor. “Flow visualization of natural convection in a tall, air-filled vertical cavity”. *International Journal of Heat and Mass Transfer* 49.5-6 (2006). (Cit. on p. 33).

[Xi2004] H. D. Xi, S. Lam, and K. Q. Xia. “From laminar plumes to organized flows: The onset of large-scale circulation in turbulent thermal convection”. *Journal of Fluid Mechanics* 503 (2004). (Cit. on p. 34).

[Zhao2019] X. Zhao, H. Ren, and L. Luo. “Gas Bubbles in Electrochemical Gas Evolution Reactions”. *Langmuir* 35.16 (2019). (Cit. on p. 20).

[Zien2000] O. C. Zienkiewicz and R. L. Taylor. *The finite element method - Volume 3: Fluid dynamics*. Butterworth Heinemann, 2000 (cit. on p. 28).

[Zoul2004] E. Zoulias, E. Varkaraki, N. Lymberopoulos, C. N. Christodoulou, and G. N. Karagiorgis. “A review on alkaline water electrolysis”. *Tcjst* 4.2 (2004). (Cit. on p. 26).

DOI: 10.18154/RWTH-2024-09734

Aachener
Verfahrenstechnik

RWTH AACHEN
UNIVERSITY